Tristan da Cunha hotspot
-
Mantle plume or shallow plate tectonics?

Dissertation

zur Erlangung des Grades Dr. rer. nat.
vorgelegt dem Fachbereich Geowissenschaften der
Universität Bremen

Antje Schlömer

20.09.2016

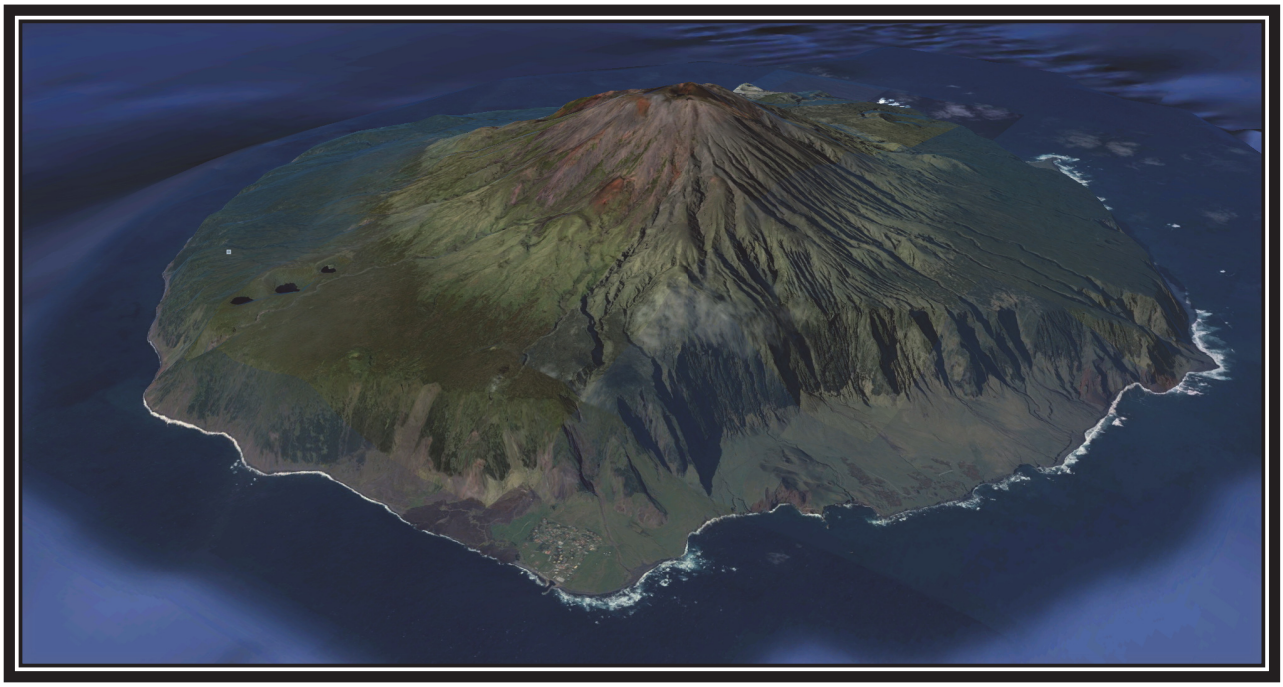

Erklärung

Antje Schlömer

Batteriestraße 59
27568 Bremerhaven

20. Sep. 2016

Hiermit versichere ich, dass ich

- die vorliegende Arbeit ohne unerlaubte fremde Hilfe angefertigt habe,
- keine anderen als die von mir angegebenen Quellen und Hilfsmittel verwendet habe,
- die den benutzten Werken wörtlich oder inhaltlich entnommen Stellen als solche kenntlich gemacht habe.

Antje Schlömer

Die vorliegende Dissertation wurde am 05.12.2016 an der Universität Bremen verteidigt. Der Prüfungsausschuss bestand aus Prof. Dr. Wilfried Jokat (erster Gutachter), Prof. Dr. Wolfgang Bach (zweiter Gutachter), Prof. Dr. Marta Pérez-Gussinyé, Prof. Dr. Tilo von Dobeneck, Dr. Norbert Kaul und Viola Bihler.

Zusammenfassung

Tristan da Cunha ist eine kleine Insel im Südatlantik, nahe des Mittelatlantischen Rückens. Sie befindet sich in einem Gebiet, was durch weit verstreute Seamounts und kleine Inseln charakterisiert ist. Die Insel liegt am westlichsten Ende der Walfischrücken - Tristan/Gough Hotspot-Spur. Sie ist das Endglied einer klassischen Hotspot-Spur, die über einem Mantelplume liegt. Die aktive Vulkaninsel Tristan da Cunha am jüngsten Ende der Hotspot-Spur ist mit der Etendeka-Flutbasaltprovinz aus der Kreide am ältesten Ende der Spur verbunden.
Die Entstehung der Insel ist bisher jedoch ein Rätsel. Es wird diskutiert, ob die Insel direkt über einem Mantleplume liegt oder ob sie auf plattentektonischen Prozessen beruht.
Um den Tristan da Cunha Hotspot zu verstehen, wurde eine multidisziplinäre Studie angelegt. Elektromagnetische und seismologische Daten wurden mit dem deutschen Forschungsschiff Maria S. Merian in den Jahren 2012 und 2013 erhoben. Ziel ist es den oberen Mantel der Erde anhand von Dichte- und Geschwindigkeitsunterschieden aufzulösen.
Ich beschränke mich in dieser Arbeit auf den seismologischen Datensatz: Zunächst habe ich eine P-Wellen Tomographie mit kreuzkorrelierten Laufzeitresiduen von teleseismischen Erdbeben gerechnet. Damit konnte ich Geschwindigkeitsunterschiede im oberen Erdmantel unterhalb der Insel auflösen und klären ob ein Mantelplume existiert. Ausserdem habe ich die lokale Seismizität in der Region um Tristan herum untersucht um tektonisch-magmatische Prozesse am Mittelatlantischen Rücken sowie an den nah gelegenen Inseln und Seamounts identifizieren zu können. Des Weiteren habe ich die elektromagnetischen Daten mit den seismologischen Daten kombiniert um Schmelzzonen zu identifizieren und um Prozesse, die mit dem Mantelplume zusammenhängen, zu verstehen.

Die tomographischen Ergebnisse liefern den Nachweis für die Existenz eines Tristan Plumes. Er ist zylindrisch und hat einen Radius von ∼100 km bis zu einer Tiefe von 250 km. Unterhalb dieser Tiefe verzweigt er sich in kleine Adern. Eine Verbindung vom Plume zu einer Seamount Kette zeigt, dass Schmelze zu Inseln und Seamounts kanalisiert wird.

In einem ozeanischen Plattensegment nördlich der Insel habe ich eine hohe Seismizität beobachtet. Diese kann auf innere Spannungen des Segmentes zurüeckgeführt werden, die aufgrund unterschiedlich angreifender Kräfte an der nördlichen Grenze dieser Platte auftreten.
Ein Gebiet, ohne Erdbeben, deckt sich räumlich mit der Lage des Tristan Plumes. Dies deutet auf eine duktile Lithosphäre oberhalb des Plumes hin.
Des Weiteren wurden Anhaltspunkte für einen Sprung des Rückens zum Plume hin gefunden. Ebenso wurden viele Erdbeben nahe des Tristan da Cunha Archipels beobachtet. Diese können mit jungen oberflächlichen Eruptionen in Verbindung gebracht werden, wie z.B. kleinen vulkanischen Kegeln oder Seamounts.

Summary

Tristan da Cunha is a small volcanic island in the South Atlantic Ocean close to the Mid-Atlantic Ridge. It is part of an area, which is characterized by widely scattered seamounts and small islands at the western end of the Walvis Ridge - Tristan/Gough hotspot track. Tristan da Cunha represents the end member of a classical hotspot track with an underlying plume: The active volcanic island Tristan da Cunha at the youngest end of the track is linked to the Cretaceous Etendeka flood basalt province in northwestern Namibia at its oldest end.
But the genesis of the island itself has so far been puzzling. It is hotly debated if the island sits actually above a deep-seated mantle plume or if it is caused by shallow plate tectonics.

To understand the Tristan da Cunha hotspot, a multi-disciplinary geophysical study has been conducted in 2012 and 2013 on board the German research vessel Maria S. Merian to acquire marine magnetotelluric and seismological data. The aim was to reveal the upper mantle structure with electrical density and velocity perturbations. Within this study I focused on the seismological dataset.
At first, I performed a P-wave finite-frequency tomography with cross-correlated travel time residuals of teleseismic earthquakes. This allows to resolve the upper mantle structure beneath the island in terms of velocity perturbations and clarifies the existence of a mantle plume. I also investigated the local seismicity in the Tristan region to identify tectono-magmatic processes at the Mid-Atlantic Ridge and close to the islands and seamounts. Moreover, I compared and combined my tomographic results with electromagnetic results to identify zones of partial melt and to understand plume processes in the upper mantle beneath the Tristan da Cunha hotspot.

The tomographic results provide evidence for the existence of the Tristan conduit southwest of the archipelago. Its shape is cylindrical with a radius $\sim$100 km down to a depth of 250 km. The structure ramifies in narrow veins below that depth. A recent link from the conduit to a seamount chain shows, that melt is channelled towards seamounts and islands in the study area.

High seismicity within an oceanic plate segment north of Tristan da Cunha can be related to the internal stresses of the fragment. Differently directed forces act at the northern boundary of this plate.
An earthquake free zone coincides spatially with the location of the Tristan mantle plume. This indicates a ductile regime in the lithosphere above the plume.
Furthermore, hints for an incipient ridge jump towards a parallel line to the actual location of the Tristan plume were found
Several earthquakes were localised close to the archipelago of Tristan da Cunha. The locations of these earthquakes are related to young surface eruptions like small volcanic cones or seamounts.

Contents

List of Tables

List of Figures

Abbreviation list

BGR	Bundesanstalt für Geowissenschaften und Rohstoffe
$BRTT$	Boulder Real Time Technologies
CMT	Centroid Moment Tensor
$CTBTO$	Comprehensive Nuclear-Test-Ban Treaty
DFG	Deutsche Forschungsgemeinschaft
FZ	Fracture Zone
GPS	Global Positioning System
IMS	International Monitoring System
$IRIS$	Incorporated Research Institutions for Seismology
$LLSVP$	Large-Low-Shear Velocity Provinces
MAR	Mid-Atlantic Ridge
ML	Local/Richter Magnitude
MTS	Magnetotelluric stations
$NEIC$	National Earthquake Information Centre
NFZ	Northern Fracture Zone
$NHNM$	New High Noise Model
$NLNM$	New Low Noise Model
NTS	Northern Tristan Segment
OBS	Ocean-bottom seismometers
PSD	Power spectral density
$SAMPLE$	South Atlantic Margin Processes and Links with onshore Evolution
SFZ	Southern Fracture Zone
SNR	Signal-to-noise ratio
STA/LTA	short time average/long time average
STS	Southern Tristan Segment
TdC	Tristan da Cunha
$TdCFZ$	Tristan da Cunha Fracture Zone
TS	Tristan Segment
$WAVfilter$	Wood-Anderson Velocity filter

1 Introduction and Motivation

1.1 Hotspot volcanism and mantle plumes

We know very little about the Earth's deep interior. One good example is the mantle plume debate. More than 50 years after mantle plumes were first proposed scientist are debating whether they actually exist.
Hot, low-density material rising up due to its buoyancy is called plume. Hotspots are believed to be surface expression of underlying mantle plumes and are unevenly distributed around the world (Fig. 1). They can be observed at mid-ocean ridges like the Iceland hotspot, within oceanic plates like Hawaii or as intra-continental volcanism such as, for example the Yellowstone or Eifel hotspot.

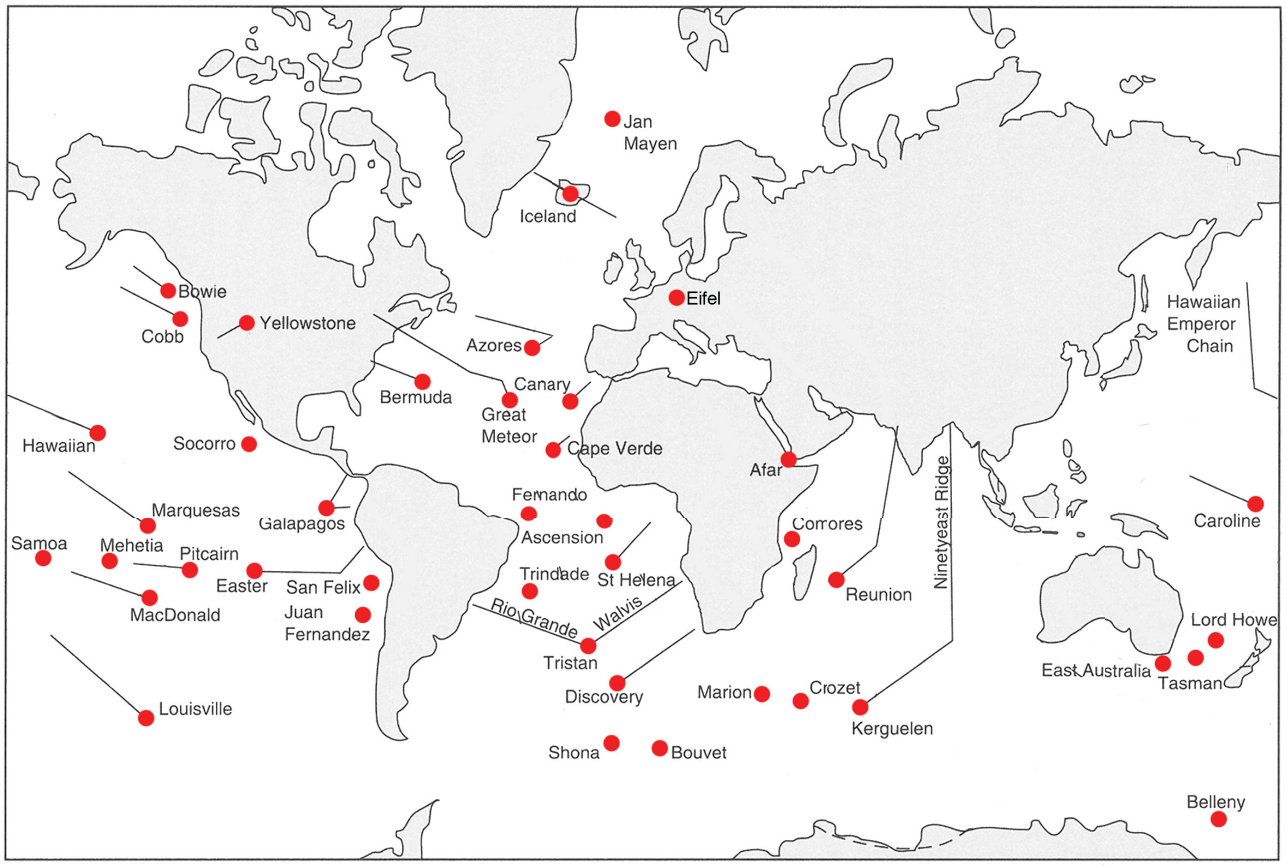

Figure 1: Global distribution of hotspots (solid red dots) and hotspot tracks (lines) (modified after Condie (2001)).

Wilson (1963) was the first who proposed mantle plume existence beneath Hawaii. Several authors (e.g., Morgan, 1971; Duncan and Richards, 1991; Courtillot et al., 2003) championed his idea and provided additional evidences. Richards et al. (1989) differentiated between a plume head, whose melt forms flood basalt provinces at the surfaces and plume tails, whose partial melting forms the hotspot tracks. A hotspot track is formed, when an oceanic plate moves across a fixed mantle plume. The Hawaiian-Emperor chain in the Pacific is one of the

most prominent hotspot tracks and is accepted to be a classical example. Condie (2001) characterized a classical hotspot track by the following facts: (1) The hotspots are overlain by topographic swells (relief: 500-1000 m; widths: 1000-2000 km). (2) Active or recently active volcanoes cover the hotspot. (3) Intermediate-wavelength gravity highs reflecting a topographic rise centred on the hotspot. (4) Volcano ridges lead away from hotspots on a age-progressive line: Older ages can be found with increasing distances from a hotspot. (5) Hotspots have a high heat flow, reflecting the mantle plume source. (6) Correlations between hotspots and a positive departure from the average geoid can be observed.
While the Earth's surface can be directly investigated, studying the Earth's interior is challenging. Seismic tomography is a suitable technique to image the Earth's interior with seismic waves produced by earthquakes. The tomographic models have been sufficiently improved and several plumes have been imaged (Montelli et al., 2004).
Despite of the plume imaging a few authors still doubt the plume theory (e.g., Anderson, 2005; Foulger and Natland, 2003). They prefer that hotspots can be explained by plate tectonic processes in a more effectively way. The Iceland hotspot serves as an example: Although, the Iceland plume was imaged by body wave tomography (Wolfe et al., 1997), Foulger and Natland (2003) tried to explained the observed features by plate tectonic processes.
Another subject of vigorous debate are the deep origins of plumes. Thermal boundary layers like the mantle transition zone (410-660 km depth), Large-Low-Shear Velocity Provinces (LLSVP) or the core mantle boundaries are likely to be generation zones for mantle plumes. French and Romanowicz (2015) used a whole-mantle imaging technique that combined wavefield computations with information of the whole seismic waveform to give first evidences of the origin of plumes at the core-mantle boundary.

A study of the intra-plate Tristan da Cunha hotspot would be an important contribution to the global mantle plume debate. The next chapter provides an introduction to the island of Tristan da Cunha and its surroundings. An additional chapter lists the research questions of this study.

1.2 Tristan da Cunha

Tristan da Cunha (TdC) is a shield volcano in the South Atlantic (37°6'S, 12°17'W). The island is located at the southwestern and youngest end of the Walvis Ridge - Tristan/Gough hotspot track, 450 km east of the present day spreading axis of the Mid-Atlantic Ridge (MAR) (Fig. 2). Besides the inhabited main island TdC, the eponymous archipelago comprises the uninhabited Nightingale group (including Stoltenhoff Island, Middle Island and Nightingale Island), the wildlife reserve Inaccessible Island and Gough Island (400 km southeast of TdC). TdC has a size of 98 km^2. The summit of the volcano Queen Mary's Peak is the highest point (2.062 km) of the island. Since the distance to the next continent is 2400 km, TdC is the most remote inhabited island in the world. Today only 265 British people live on the island.
A Portuguese sailor, Tristão da Cunha discovered the island and named it after himself in 1506. The United Kingdom formally annexed the island to prevent the French from using it as a base to liberate Napoleon Bonaparte from his prison on the nearby island Saint Helena.
The first eruption on TdC felt by the inhabitants was in October 1961, preceded by several earthquake swarms. Rocks fall from the cliffs and a dome-shaped mass of lava (tholoid) was erupted from a flank of the volcano (Baker et al., 1962). A huge tholoid had breached on the

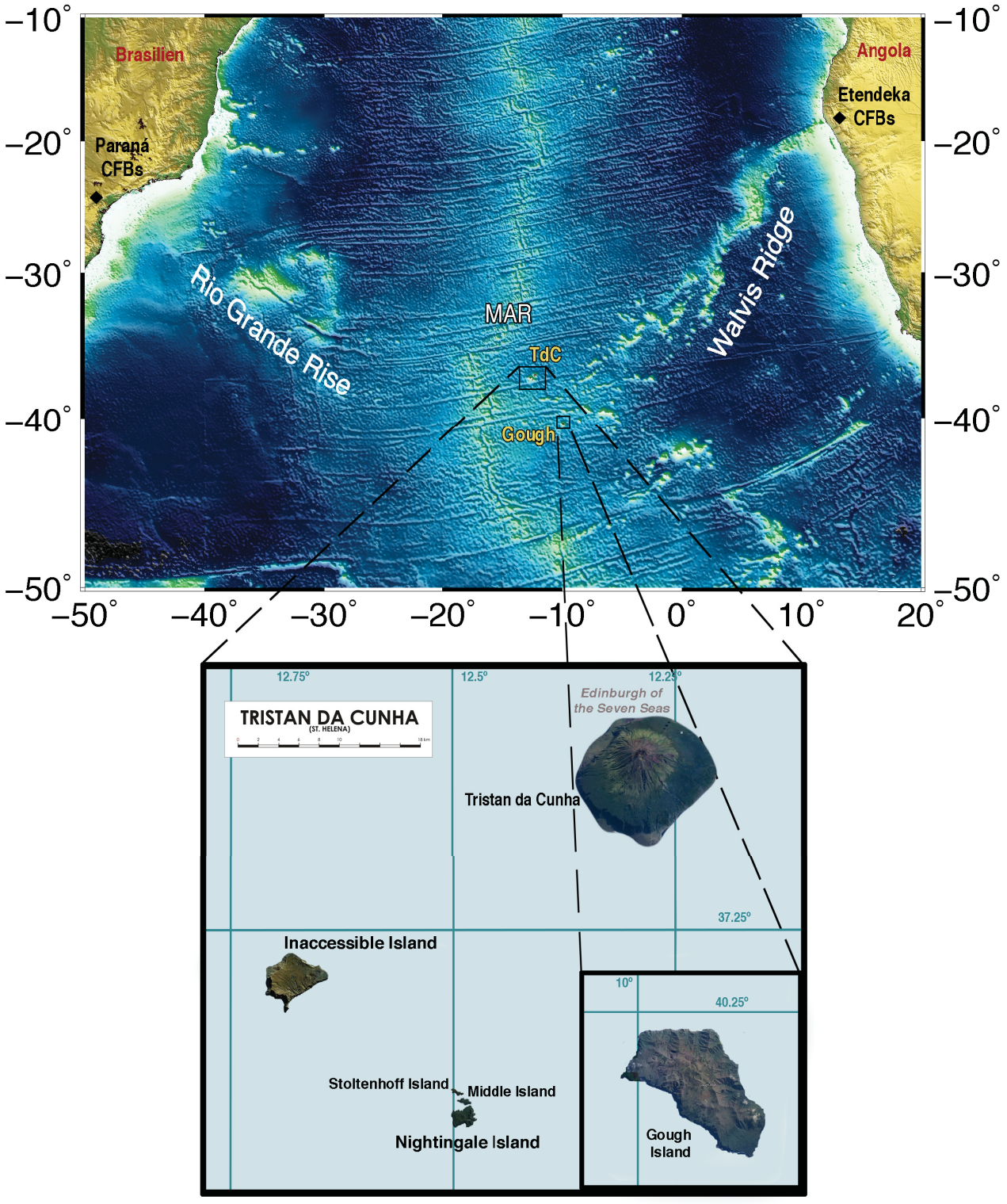

Figure 2: South Atlantic Ocean and the archipelago of Tristan da Cunha

seawards side and the lava extended into the ocean. A photo (Fig. 3) published by Baker et al. (1962) illustrates this eruption. It shows the tholoid (black areas) surrounding the east side of the settlement *Edinburgh of the Seven Seas*. A substantially growth of the dome had been

observed during one week after the eruption. Subsequently, the inhabitants were evacuated to the United Kingdom for one year.
Another intense earthquake swarm occurred on 29-30 July 2004. The strongest earthquake reached a magnitude of 4.8. The Tristanians were evacuated, but could return after one day. With only two seismometers present on TdC, the location of these events was estimated to be close to Nightingale Island. Floating pumice was found on the sea-surface and on the beaches close to TdC. Hards (2004) associated it to a submarine vent on the flanks of the Tristan volcano. They suggested an injection of new magma from great depth or faults, which intersects a magma chamber to explain the event.

Figure 3: The 1962 Eruption: Tholoid east of the settlement (Baker et al., 1962).

1.3 Walvis Ridge - Tristan/Gough hotspot track

TdC located at the youngest end the Walvis Ridge - Tristan/Gough hotspot track is widely accepted to be the youngest surface expression of the deep-seated Tristan mantle plume (Morgan, 1972; White and McKenzie, 1989; Courtillot et al., 2003). In this context, it is controversially discussed, if and in which way the plume contributed to the breakup of the South Atlantic. (e.g., Fromm et al., 2015; Jokat et al., 2003; Heit et al., 2015).
Many events in the past are also associated with the Tristan plume: ∼132 Ma ago, the arrival of the plume head at the base of the lithosphere is thought to be responsible for the emplacement

of the Paraná (South America, Brazil) and Etendeka flood basalts (Africa, Namibia) (White and McKenzie, 1989; Renne et al., 1996; Gibson et al., 2005). While the South Atlantic opened, the ridge-centered plume tail and its related volcanism formed the hotspot track, starting with the Walvis Ridge on the African Plate and the Rio Grande Rise on the South American Plate (Morgan, 1971; O'Connor and Duncan, 1990; O'Connor and le Roex, 1992; Wilson and Guiraud, 1992). Since $\sim$ 70 Ma, the mid ocean ridge drifted westwards away from the plume. Intra-plate volcanism occurred on the African Plate and formed a province consisting of widely distributed small islands and seamounts.
Because of the close proximity to the ridge it is likely that plume material flows along the base of the lithosphere towards the nearby ridge or rather thinner lithosphere (Sleep, 2002).
Another issue that is discussed concerns the deep origin of the Tristan plume. The reconstructed location where the Paraná and Etendeka flood basalts initially erupted and the location of the assumed plume (here TdC), overly the margin of the LLSVP. Therefore, the LLSVP in the deep mantle is proposed to be a likely zone to generate the Tristan plume (Torsvik et al., 2006; Burke et al., 2008).

Several characteristics of the Walvis Ridge - Tristan/Gough hotspot track meet the criteria for a classical hotspot track listed by Condie (2001) (See 1.1): An active volcanic island (TdC) is situated at the youngest end of the hotspot track, while a continental flood basalt province can be found at its older end (Richards et al., 1989). The volcanism along the hotspot track is age-progressive due to older ages with increasing distances from TdC (O'Connor and Duncan, 1990; O'Connor and le Roex, 1992). Furthermore, a topographic swell can be observed (Sleep, 1990).
Courtillot et al. (2003) collated five criteria to characterize plumes (age-progressive track, high buoyancy flux, high $^{3}He/^{4}He$ ratio, seismic anomaly beneath the hotspot and associated flood-basalts) and classified Tristan to be one of the "primary" mantle plumes.
However, peculiarities compared to a classical hotspot are present: The youngest end of the hotspot track is characterized by widely scattered seamounts and small islands and a diminishing volcanism can be observed in the region. These facts, however, tend to contradict a plume tail with a diameter of 100-200 km.
Contrary to the plume theory, some authors proposed that the active volcanism in the region can be better explained by shallow plate tectonic origin (e.g., Anderson and Schramm, 2005). Fairhead and Wilson (2005) proposed that faulting and fracturing of the oceanic lithosphere can lead to subsequent melt transport towards sites of volcanism.

In contrast to a lack of geophysical observations in the investigated area, several petrological studies have been carried out in the past: Hanan et al. (1986) explained variations of Pb isotopes of mid-ocean ridge basalt (MORB) in the Tristan region by distinct channel connections between the off-ridge plume and the ridge. Rohde et al. (2013a) and Hoernle et al. (2015) showed different isotopic compositions for Tristan and Gough based on Sr–Nd–Hf–Pb isotope data from the respectively islands (Fig. 4 b and c). Therefore the authors suggest a bifurcation of the hotspot track after $<$70 Ma into a northern subtrack directed towards TdC and a southern subtrack directed towards Gough (Fig. 4a). They explain these differences by a geochemically zonation of the plume. While the enriched Gough source reflects the African superplume composition, the more depleted Tristan source represents a mixture of the superplume with the

surrounding depleted mantle (Fig. 4d).

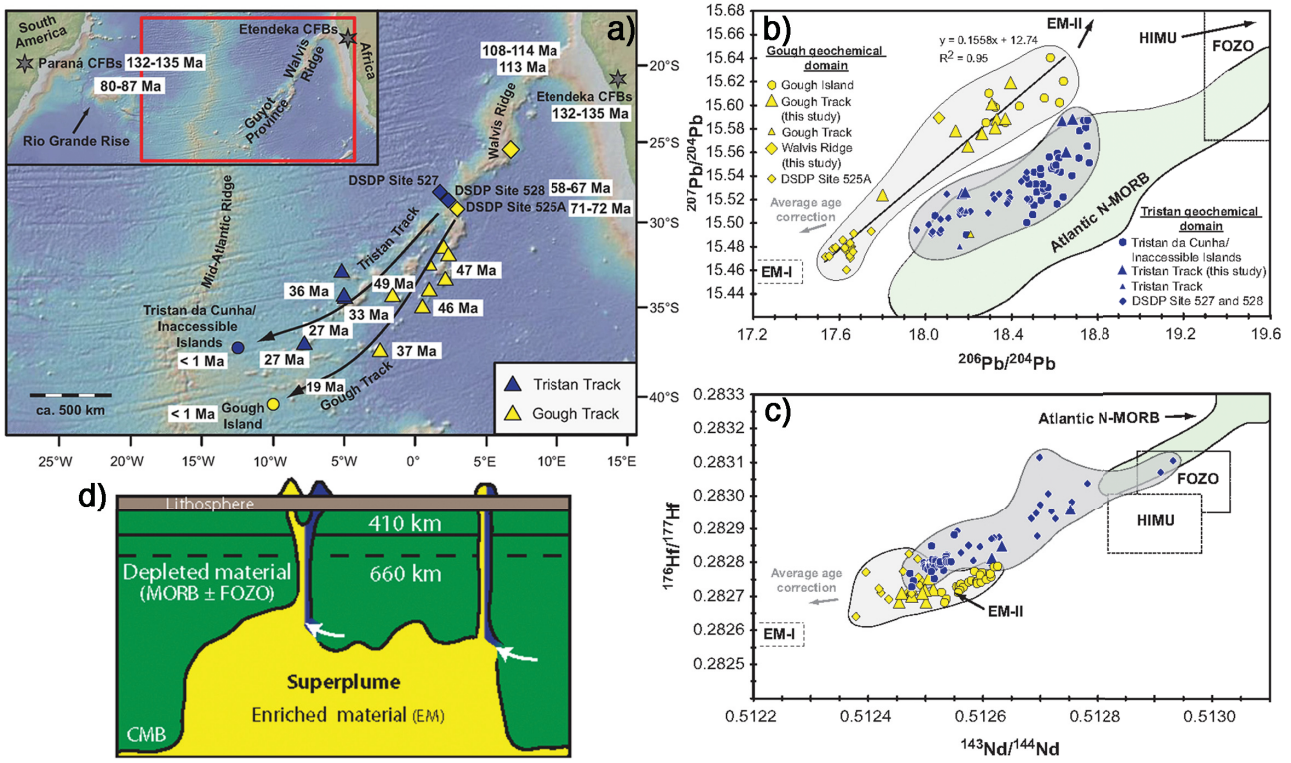

Figure 4: Results of Rohde et al. (2013a): a) Overview map of the hotspot track with Tristan and Gough subtracks with sample ages. b) and c): Pb, Nd and Hf isotope variation diagrams, showing distinct geochemically domains for Tristan and Gough samples. c) Nd versus Hf isotope variations. c) Schematic model showing the origin of geochemically zoned plumes from superplume boundaries.

Other authors have proposed a heterogeneous source at depth, from which melt has been discretely siphoned off to undergo rapid fractionation in conduits, chambers and dikes closer to the surface (Le Roex et al., 1990; Reagan et al., 2008), a branching plume stem, or a plume stem transporting discrete blobs (Rohde et al., 2013b; Hicks et al., 2012).

The Tristan plume has not been successfully resolved by global tomography. The models (e.g., Ritsema et al., 1999; Ritsema and Allen, 2003; French and Romanowicz, 2015) resolve large-features in the Earth's mantle easily and reliable. Whereas the resolution of small-scale heterogeneities in some regions of the world is poor due to a low station density in this area. Figure 5a-c shows global shear-wave velocity heterogeneities in different depth slices. Large anomalies and low shear velocity along the MAR down to 200 km can be observed, but no heterogeneities smaller than 200 km. Figure 5d shows a cross section of the whole mantle, unfortunately a little bit south of TdC.

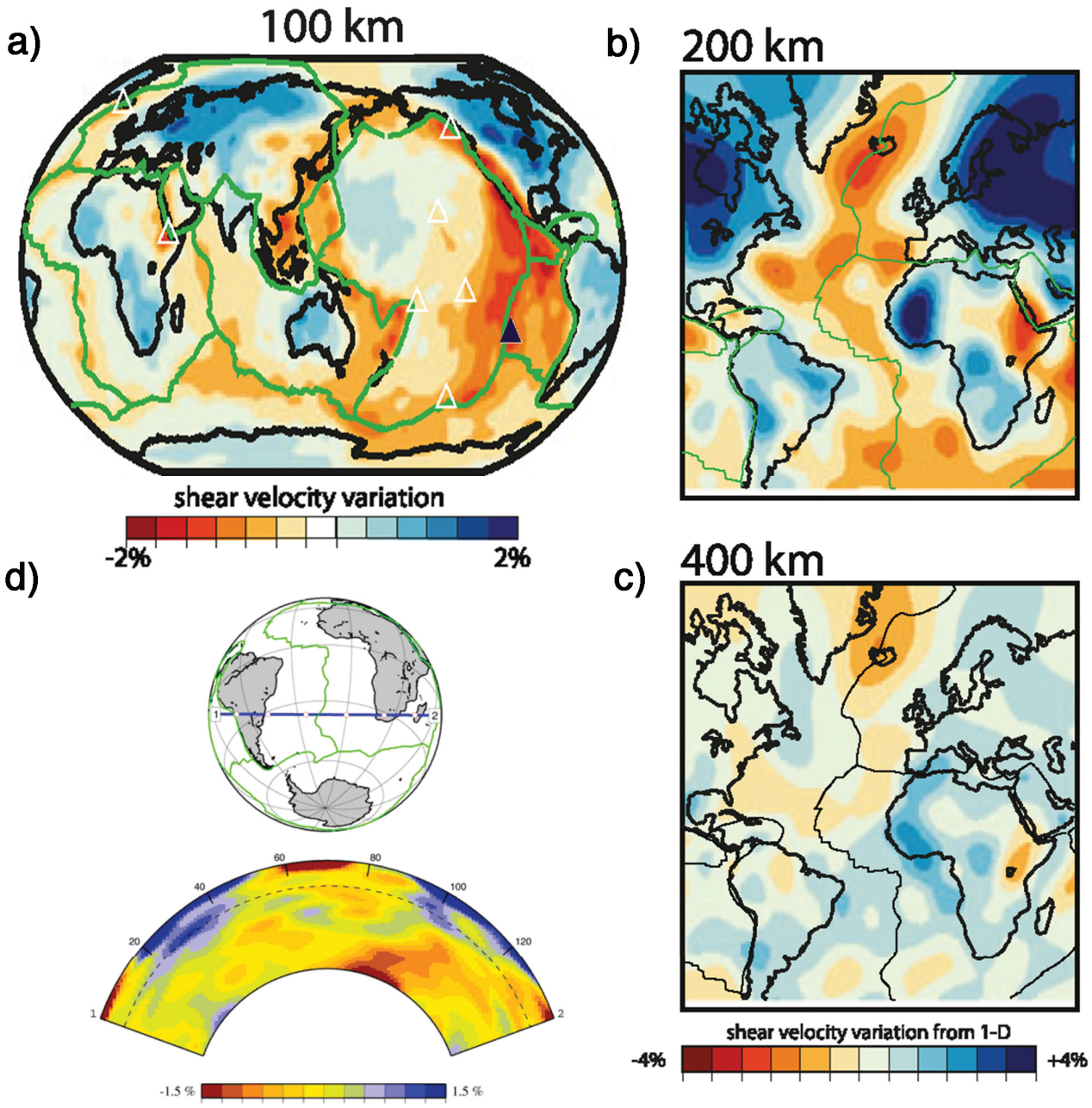

Figure 5: a-c) Shear-velocity heterogeneities in different depth slices showing lower velocities at plate boundaries and rigdes down to 200 km and higher velocities below the continents. Tristan is marked with a blue triangle (Ritsema et al., 2011). d) Cross section of the whole mantle showing the ridge-melt beneath the MAR (Ritsema et al., 1999).

1.4 Research questions

The previous chapters have shown that various different approaches exist to explain the origin of the Tristan da Cunha hotspot. But none of these assumptions has been proven by direct regional geophysical data. This thesis aims at closing these knowledge gaps. A multidisciplinary geophysical study of the Tristan region was conducted to resolve the upper mantle with electrical resistivity and seismic velocity variations. Two cruises were carried out to collect magnetotelluric as well as seismological data. In this study, I analysed the Earth's upper mantle in terms of velocity perturbations. Another topic is to study the local seismicity in the TdC region. In the following sections, I will summarize the central questions of the thesis.

1.4.1 Upper mantle

Can the genesis of Tristan da Cunha be attributed to a deep-seated mantle plume or explained by shallow plate tectonics?

If a plume exists:

- **Where is the plume located?**
- **How does the plume look like?**
- **Does the plume interact with the Mid-Atlantic ridge?**

If no plume exists:

- **Which processes formed Tristan da Cunha?**
- **In which way can plate tectonics explain the hotspot track?**
- **What are the contributions of the Mid-Atlantic Ridge?**

1.4.2 Local seismicity

How are earthquakes distributed in the Tristan da Cunha region?

- **Which processes can be identified at faults and fracture zones?**
- **What kind of seismicity is present at the Mid-Atlantic Ridge and close to known volcanic edifices like islands and seamounts?**
- **If a plume is present how does it influence the seismicity?**

2 Dataset

This work was part of a multi-disciplinary geophysical study of the TdC region. On the Maria S. Merian cruise MSM20/2 in January 2012 a network consisting of 24 broadband ocean-bottom seismometers (OBS), 26 magnetotelluric stations (MTS) and two seismological land stations were deployed around the archipelago of TdC and on Nightingale Island. After one year of acquiring passive marine magnetotelluric and seismological data, the instruments were recovered on the Merian cruise MSM24 in January 2013. The project was part of the DFG (**D**eutsche **F**orschungs**g**emeinschaft) Priority Program 1375 SAMPLE (**S**outh **A**tlantic **M**argin **P**rocesses and **L**inks with onshore **E**volution). The aim was to resolve the upper mantle beneath TdC with electrical resistivity and velocity perturbations. As a first geophysical study of this kind in the TDC region, the dataset is unique.

2.1 Stations

While one part of the study deals with resolving the upper mantle in terms of velocity perturbations, another part concerns the local seismicity in the TdC region. Therefore, the following chapters only focus on the evaluation of the seismological dataset and its acquisition by the OBS network.

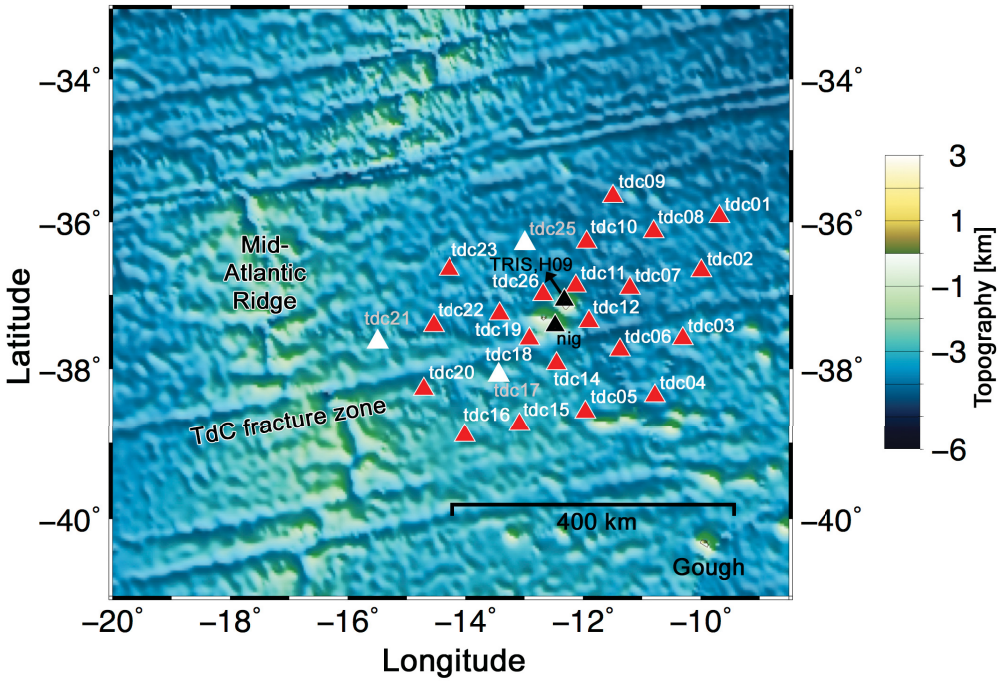

Figure 6: Station distribution of OBS locations (red triangles), land stations on Nightingale Island and the permanent station TRIS as well as the Hydrophone stations H09, both located on the main island Tristan da Cunha (black triangles). White triangles mark the OBS stations, whose data acquisition failed.

2.1.1 OBS and land stations

The OBS station network covered an area of 400 km x 500 km around the archipelago with an average station spacing of approximately 85 km (Fig. 6 and tab. S1). The western boundary of the array was located 120 km away from the MAR. The OBS stations were equipped with Güralp CMG-40T broadband seismometers with four channels (Hydrophone, vertical and two horizontal components). Most of the data were sampled with 50 Hz. Two OBS (tdc11 and tdc04) sampled with 100 Hz. Both land stations nig01 and nig02 were equipped with Güralp-3ESP Compact 60 s seismometers and were installed on Nightingale Island. These instruments sampled the data with 100 Hz.

2.1.2 Permanent station TRIS

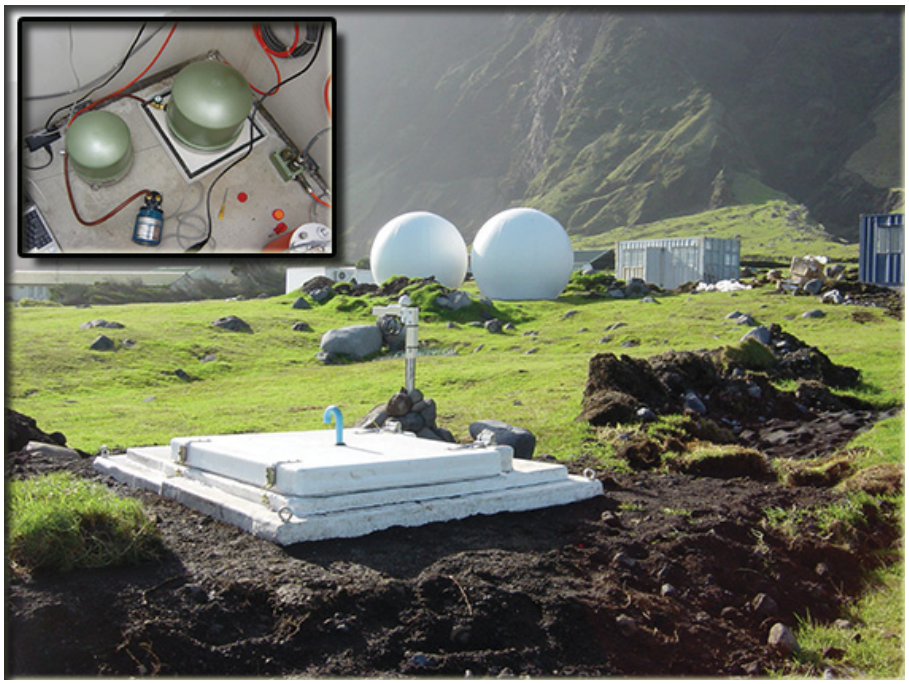

Figure 7: Permanent station TRIS located on TdC and equipped with an STS-2 (inset).

All available data of the permanent station TRIS, installed on TdC and operated by IRIS (**I**ncorporated **R**esearch **I**nstitutions for **S**eismology), were used. TRIS is equipped with an STS-2 seismometer (Fig. 7) and sample data with a sampling frequency of 100 Hz. Unfortunately, the station was flooded within 2012 implying that only a sparse amount of data were recorded at the beginning of the experiment.

2.1.3 Hydroacoustic stations H09

The BGR (**B**undesanstalt für **G**eowissenschaften und **R**ohstoffe) offers data access to two hydroacoustic stations, located on TdC. These stations belongs to the IMS's 11 (**I**nternational **M**onitoring **S**ystem) hydroacoustic stations operated by the CTBTO (**C**omprehensive Nuclear-**T**est-**B**an **T**reaty) to detect natural and man-made phenomena like nuclear detonations in the oceans. These stations detect acoustic waves that are converted to seismic waves when they hit

land. The hydroacoustic stations HA09 consist of two three-component seismometers. One of the seismometers (HA09N1) is located near the main city *Edinburgh of the Seven Seas*, 500 m away from the coast and in immediate vicinity to the seismological station TRIS. The second station (H09W1) is located in the western part of TdC one kilometre away from the sea.

2.2 Data Quality

The use of ocean-bottom seismometers is complex and labour-intensive compared to land stations: Accessing the instruments after deployment to correct failures is not possible. Therefore, the OBS has to be carefully prepared before the deployment in the ocean. These preparations include equipping with batteries, programming of the recording and release system, synchronization of the internal clock, testing the operation modus of hydrophones and seismometers and finally starting the radio beacon and flash light systems. After the deployment, the instruments sink on the ocean bottom and are at the mercy of pressure, temperature differences, surrounding water and its currents. These are the reasons, why the data quality of an OBS cannot be compared to quality reached by land stations.
Figure 8 gives an overview of the availability and quality of the dataset during 2012. OBS tdc17 and tdc25 could not be recovered and tdc21 did not record any data. The second land station nig02 recorded a sparse amount of data as well as TRIS (see 2.1.2). At several stations the hydrophone component did not work reliable, which means that spikes and artefacts disturbed the seismograms. This phenomenon can also be observed at a few horizontal components.

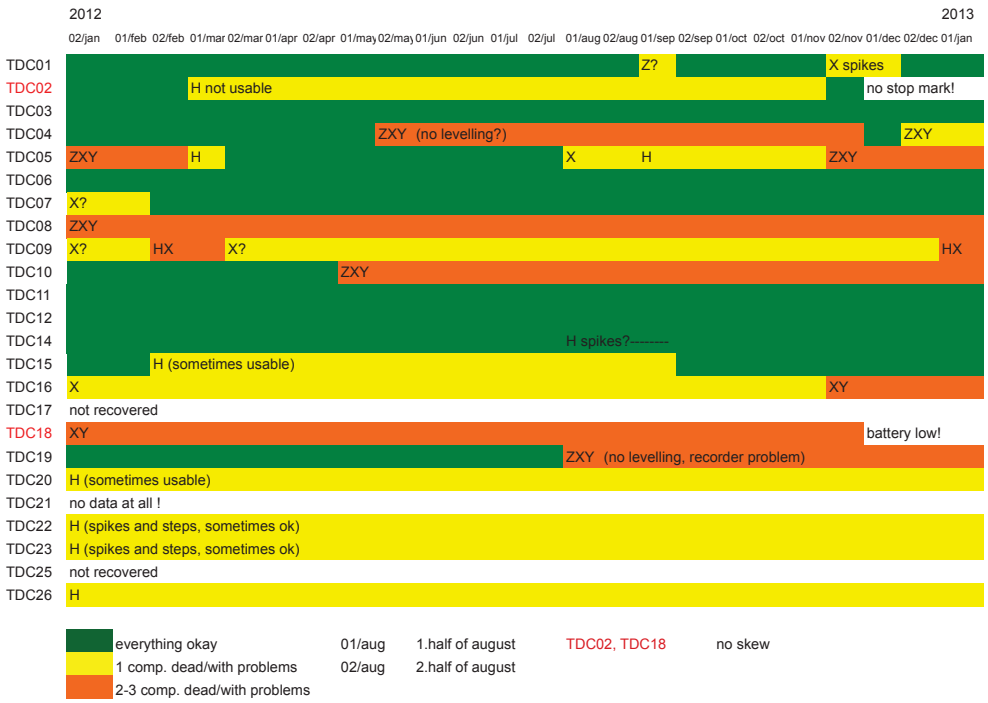

Figure 8: Quality of the seismological dataset (from cruise report of MSM24 (Geissler, 2013)).

2.2.1 Ambient seismic noise

It is a challenge, while working with OBS data to deal with the high noise level in the oceans caused by storms, tides and flows. Therefore, this chapter deals with the prevailing background noise in OBS and land station seismograms. In a first step I demonstrate the relationship between noise in OBS seismograms and wind speed at the surface. In a second step I compared the noise of land stations and OBS.

Figure 9 shows the wind speed recorded on the island TdC during the whole year 2012 provided by the MeteoGroup. The wind speed ranges mostly between $20\frac{km}{h}$ and $40\frac{km}{h}$.

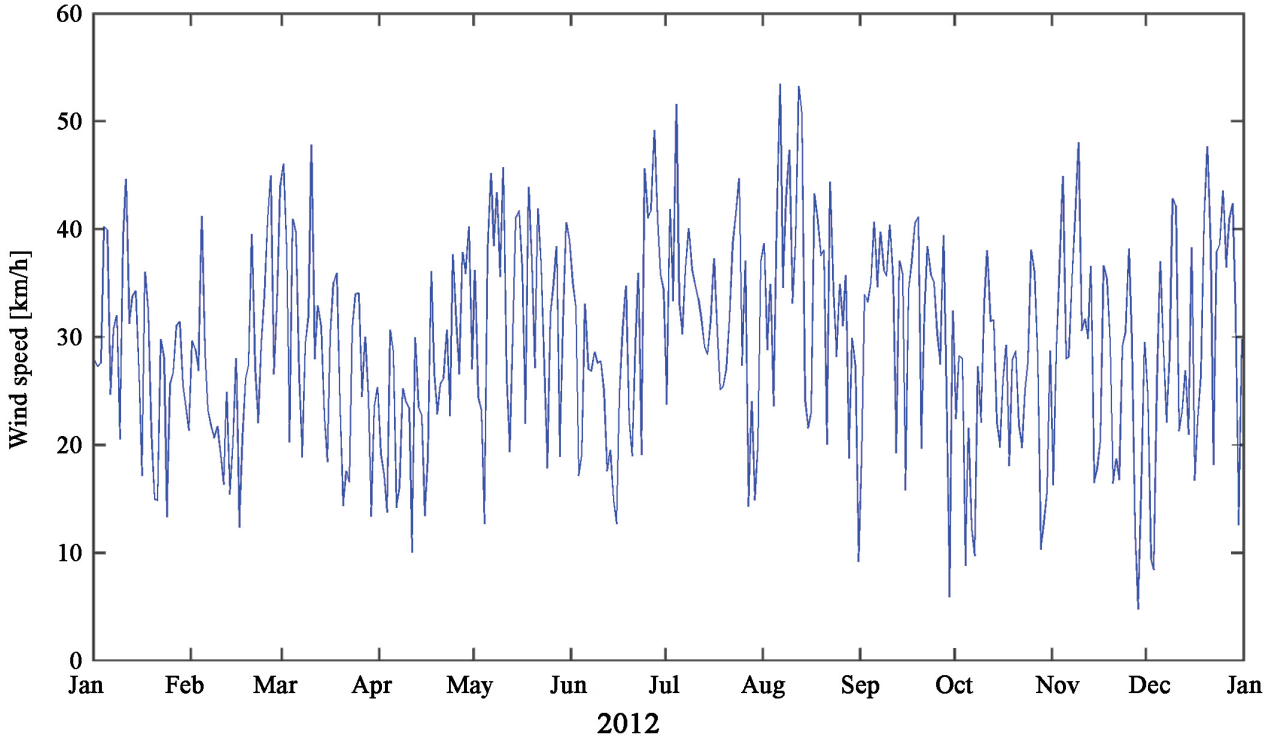

Figure 9: Wind speed during the year 2012 (source: MeteoGroup based on ERA-Interim analyse models).

For measuring the background noise, I calculated the power spectral density (PSD) of the noise of the OBS tdc03 for the whole year, took an average value for every day and compared these values with the wind speed (Fig. 10).
The PSD or noise power can be expressed in units of decibel dB, which can be related to $(\frac{m}{s})^2/Hz$ as a function of the frequency. Figure 10 shows the normalized curves for the wind speed and for the power spectral density of noise. Several peak amplitudes show a perfectly time fit or the noise power peaks are a little bit postponed to a later stage. I also plotted a polynomial fit of 10th degree to both curves. These fitting curves (Fig. 10) show a very good correlation, which indicates a strong relation between the wind speed at the surface and the noise at the ocean bottom. The observed delays could indicate, how the wind power is coupled into the oceans.
To classify the signal-to-noise ratio (SNR), I plotted the velocity PSD of the land station nig01 and the OBS tdc03 within the boundaries of the Peterson (1993) **N**ew **L**ow **N**oise **M**odel (NLNM) and the **N**ew **H**igh **N**oise **M**odel (NHNM) (Fig. 11). The Peterson models represent the PSD determined by 75 worldwide stations for noisy (NHNM) and quiet (NLNM) periods and therefore present accepted limits of seismic noise. Figure 10 shows the PSD on a quiet (a) and on a windy (b) day for both stations. The PSD of the land station on a quiet day lies in the upper third of the Peterson model boundaries, while the PSD of the OBS station lies slightly above the NHNM in a frequency range of 0.03 Hz to 1 Hz. On a windy day, the PSD

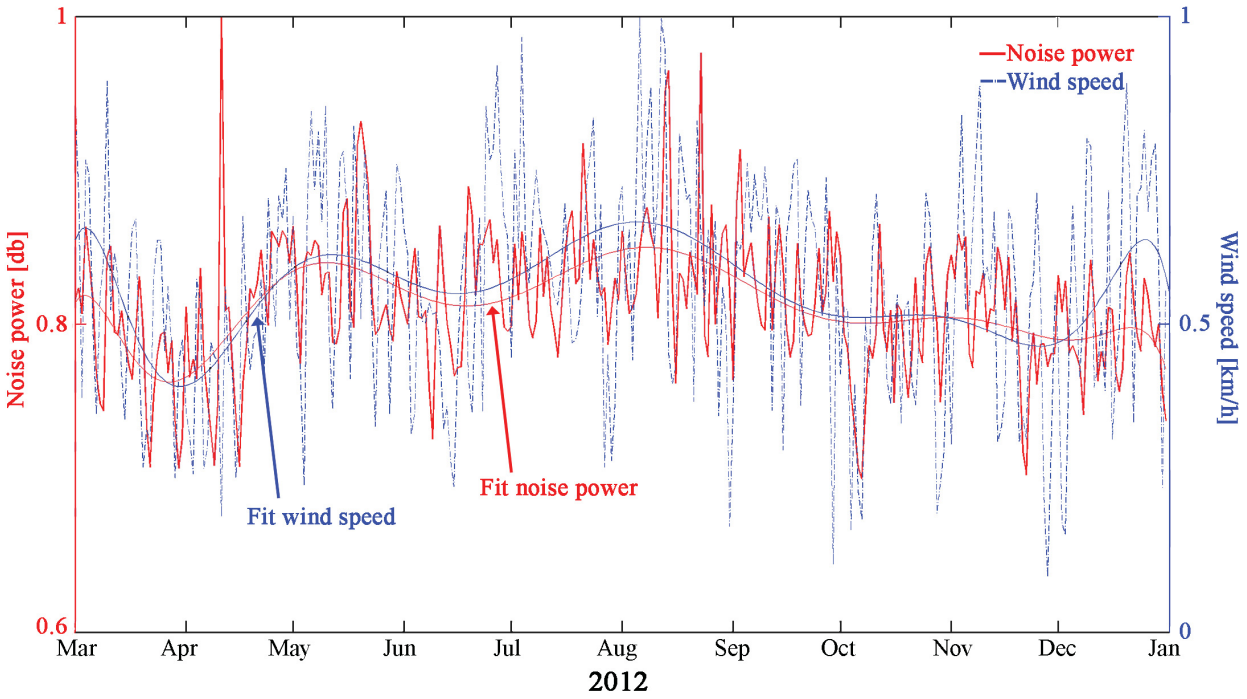

Figure 10: Wind speed and noise power of the OBS tdc03 and their corresponding polynomial fittings (10th degree) during the year 2012.

of the land station exceeds the NHNM boundary in a frequency range of 0.03 Hz to 1.1 Hz. In that range, the PSD of the OBS station is 5 dB higher than the NHNM. Thus, even if the wind speed is low at the surface, the noise at the ocean bottom is very high in a frequency range lower than 1.3 Hz. It is also apparent, that the PSD of the land station is high compared to the OBS station at frequencies larger than 1 Hz.
In summary, the noise registered with the network either on land or at the ocean bottom is very high even on calm days. While the land stations have an even higher noise level at high frequencies (> 3 Hz), the OBS have a high noise level at low frequencies (< 1 Hz).
TdC is located close to the "Roaring Forties", a region of strong westerly winds throughout the year. The noise level at high frequencies is caused by the arrival of surf and waves on the coast of TdC at windy days. Arriving waves at beaches and coastal regions as well as smashing surf in shallow water generate pressure variations, which are converted into seismic energy (Bormann and Wielandt, 2002). Also, the high wind speed on TdC causes wind friction on the surface or wind vibrations, which are detected at the land stations. The amplitude of this specific noise decays exponentially with depth. This is the reason that this high frequency noise is not detected by the OBS.
High noise at low frequencies, which is observed at OBS, is generated by superposition of ocean waves with similar frequencies travelling in opposite directions (Bormann and Wielandt, 2002). Waves, generated at the front side of a low-pressure zone can interfere with waves from the backside of this zone. The superposition of these waves generated standing waves, which cause non-linear pressure perturbations propagate to the bottom of the ocean without any attenuation (Bormann and Wielandt, 2002). Low-pressure zones from Antarctica perpetually afflict the Tristan region. This could be the reason for this high noise level.

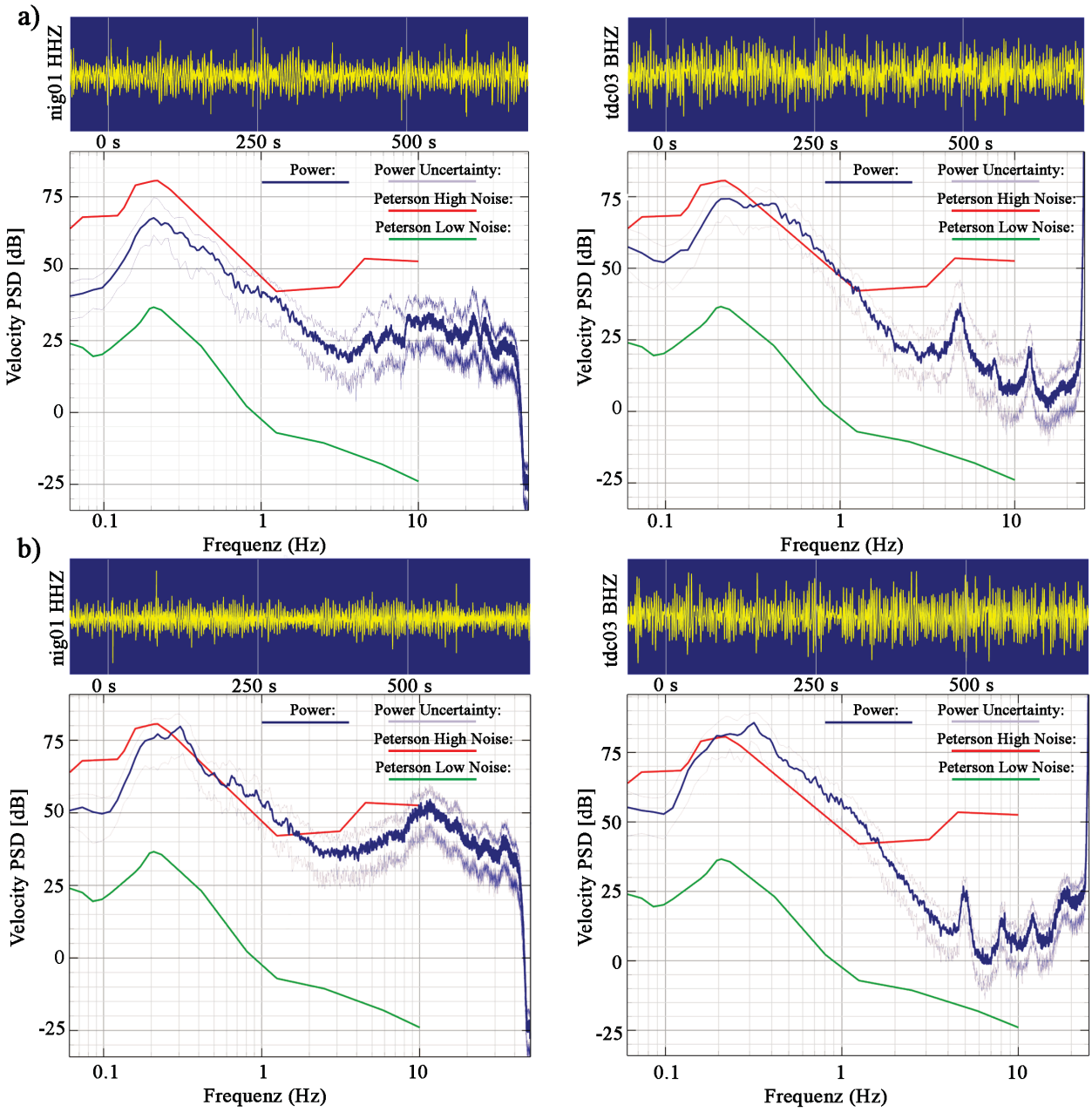

Figure 11: Velocity power spectral density (PSD) within a time window of 640 s for the land station nig01 and the OBS tdc03 is shown. a) PSD measured on a quiet day ($v_{wind} < 10\frac{km}{h}$) (29.03.2012 05:09:20). b) PSD measured on a windy day ($v_{wind} > 40\frac{km}{h}$) (11.07.2016 03:09:20).

2.3 Observed signals

Records of continuous broadband data were acquired, which were limited by the properties of the used instruments. One part of this study includes a tomography of the upper mantle beneath the island, calculated with travel time arrivals of teleseismic events. Another part deals with the detection of local earthquakes in the study region. Since teleseismic earthquakes are observed in a low (<2 Hz) frequency range, local earthquakes can be observed in a high frequency range (>5 Hz). The following subsections show examples of various signals registered in different frequency ranges with the network.

2.3.1 Teleseismic earthquakes

To calculate a tomography of the earth's upper mantle, body-wave arrivals of teleseismic earthquakes with distances more than 30° are needed. The year 2012 was a very weak earthquake year concerning regions of known high seismicity like e.g. the South Sandwich Trench. Figure 12 shows the earthquake occurrence in 2012 with magnitude (mb) larger than 5 and a distance larger than 30°. (The earthquakes are provided by the **N**ational **E**arthquake **I**nformation **C**enter (NEIC), which is part of the Department of the Interior, U.S. Geological Survey.) But unfortunately only a small portion of these earthquakes could be observed in the recorded data or were suitable fore use in the tomography. In the following I therefore present examples of suitable earthquakes and examples of earthquakes, which were not inappropriate for this study.

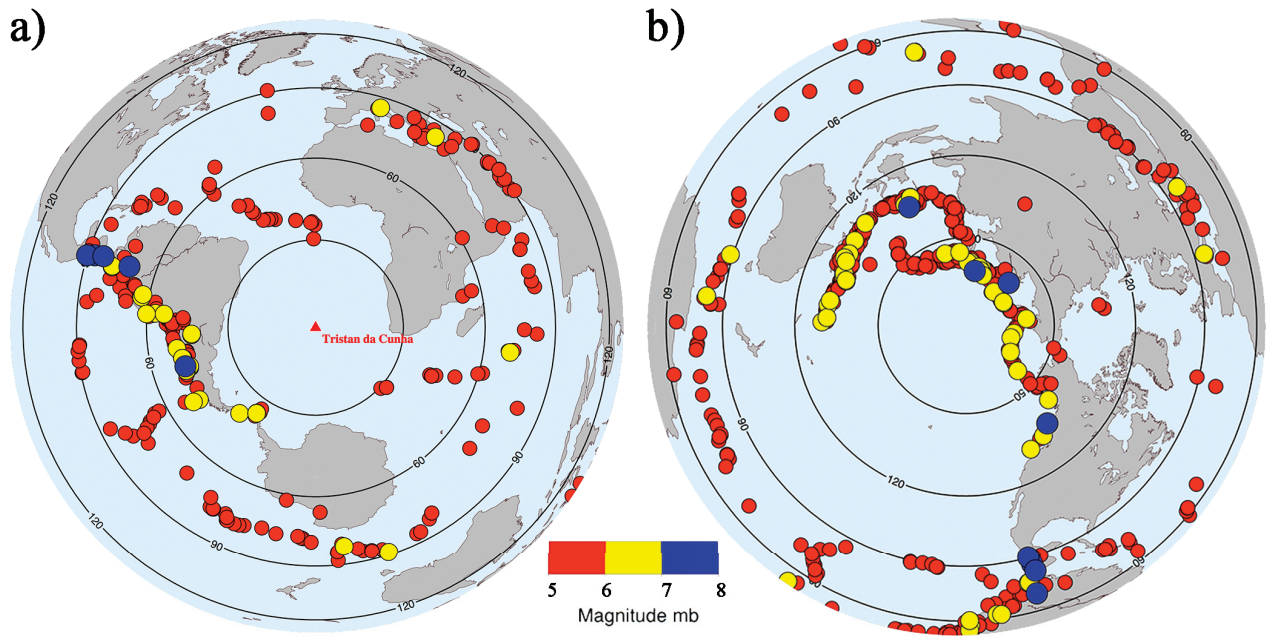

Figure 12: Azimuthal distribution of NEIC catalogue earthquakes occurred 2012 with TdC in its centre (a) and with the antipode of TdC in its centre (b).

Figure 13 shows raw seismograms of a Chile earthquake (25.03.2012) with magnitude (mb) 7.1. This is a suitable earthquake due to clear observable P-arrivals at all stations at around 22:46 UTC. The surface waves can also been viewed at around 23:00 UTC. The corresponding

spectrogram of OBS tdc04 (Fig. 14) shows higher velocity amplitudes at the P-arrival time at frequencies lower than 1 Hz compared to time prior of 22:46 UTC. The branch of the surface wave amplitudes starting at 23:00 UTC is visible below 0.08 Hz. The bottom of the picture shows the velocity amplitudes at a time prior to the P-arrival (background noise) and after the arrival (signal). The amplitudes of the signal are larger up to a frequency of 3 Hz in comparison to the background noise.

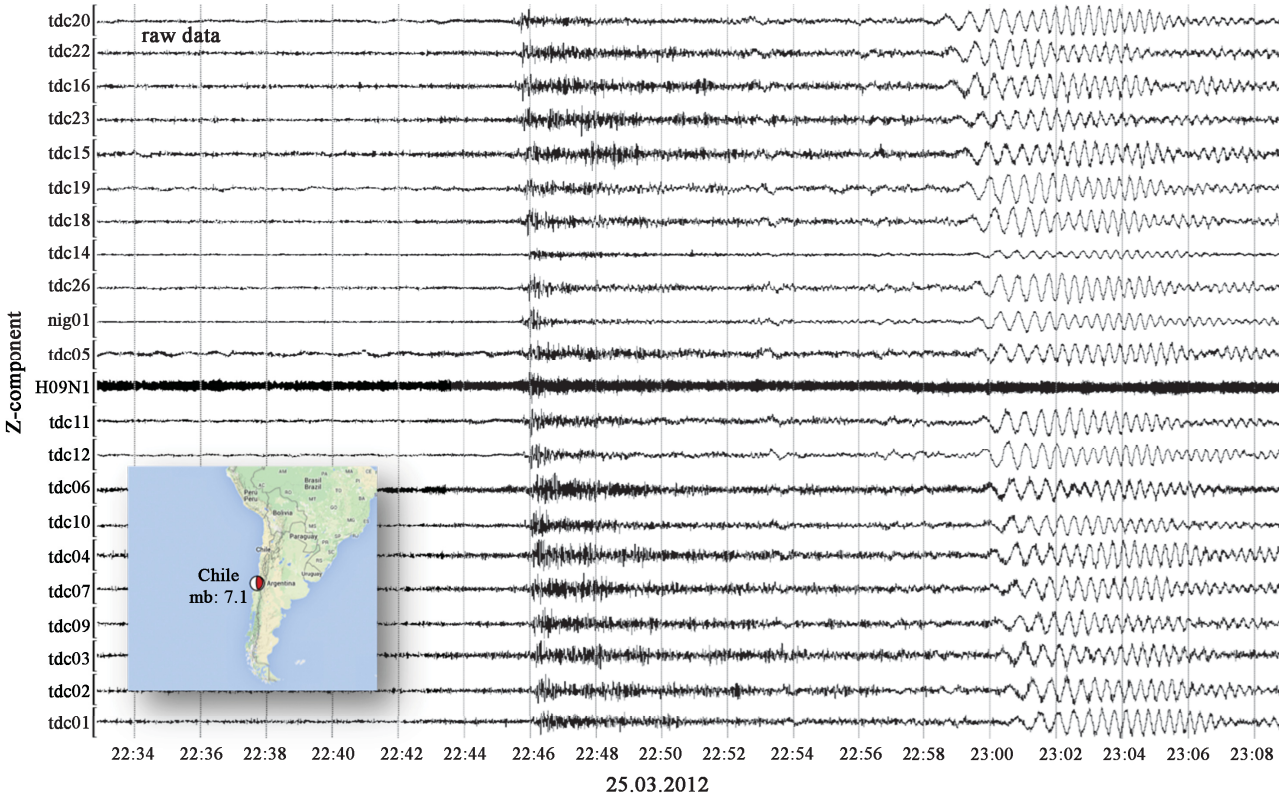

Figure 13: Chile earthquake (25.03.2012 22:37:06, mb: 7.1) registered on the vertical components.

In contrast to this earthquake showing a high SNR even in raw seismograms, figure 15 shows bandpass filtered (0.05 Hz to 0.07 Hz) seismograms of a Panama earthquake (04.06.2012) with magnitude (mb) 6.3. The seismograms are aligned to the theoretical P-arrival at 00:45:15 UTC, but only the surface waves at ∼01:15 UTC are visible. (The seismogram of the land station nig01 shows a distinct waveform at around 00:47 UTC: This is a filter artefact due to a gap in the raw seismograms.) Figure 16 shows the corresponding spectrograms for the land station nig01 (a) and the OBS tdc06 (b) and the velocity amplitudes for time prior to the theoretical P arrival and after the arrival. It is shown in the spectrograms that the frequency range between 0.1 Hz to 0.04 Hz for the land station (a) has large amplitudes and no high amplitudes mark the P arrival. Signals arriving after 01:07 UTC are observable with a frequency lower than 0.1 Hz. The branch of the surface waves can be observed after 01:20 UTC in a frequency range below 0.08 Hz. The velocity amplitudes at times before and after the theoretical P-arrival show slightly larger amplitude compared to the background noise at frequencies below 0.1 Hz. At higher frequencies the amplitudes are in the same range. The spectrogram for the OBS station (b) has large amplitudes at 0.1 Hz to 1 Hz. This is a broader range compared to the land

station. Unfortunately, this is the frequency range, where body waves from teleseismic earthquakes normally occurs (See spectrogram of the Chile earthquake (Fig. 14)). Below 0.03 Hz the background noise has also large amplitudes. Even the branch of the surface waves (starting at 01:25 UTC) is difficult to recognize. The velocity amplitudes at two times before and after the theoretical P-arrival almost coincides, which means that no special frequency stand out and the SNR is low. By comparison both spectrograms at frequencies higher than 3 Hz, the noise amplitude is larger for the land station compared to the OBS. The reasons for that are discussed in chapter 2.2.1.
For further demonstrations I added a Greece earthquake with magnitude 6 (Fig. S3), an Ascension Island (Fig. S5) earthquake and a South Sandwich earthquake (Fig. S4 with magnitudes 5.0 and 5.3, respectively to the supplementary material. All examples have in common, that no P-arrivals are observable. Therefore, it is difficult to determine a threshold for magnitude and distance at which P-arrivals are observable. A reliable magnitude of completeness seems to be in the order of 6.5.
Trying to find a pattern for the detection of earthquakes with no P-arrival, I investigated the corresponding weather conditions (high wind speed) and the node plane of the fault mechanism of these events (Fig. S2). I could not recognize any systematic pattern, whereas I only considered the wind speed on TdC and not the prevailing weather conditions in the whole area.
It seems that the detection of earthquakes with this network have to be assigned to the fortunate coincidence of local weather conditions, the arrival of low-pressure zones, the magnitude and distance of the events and their fault mechanisms.

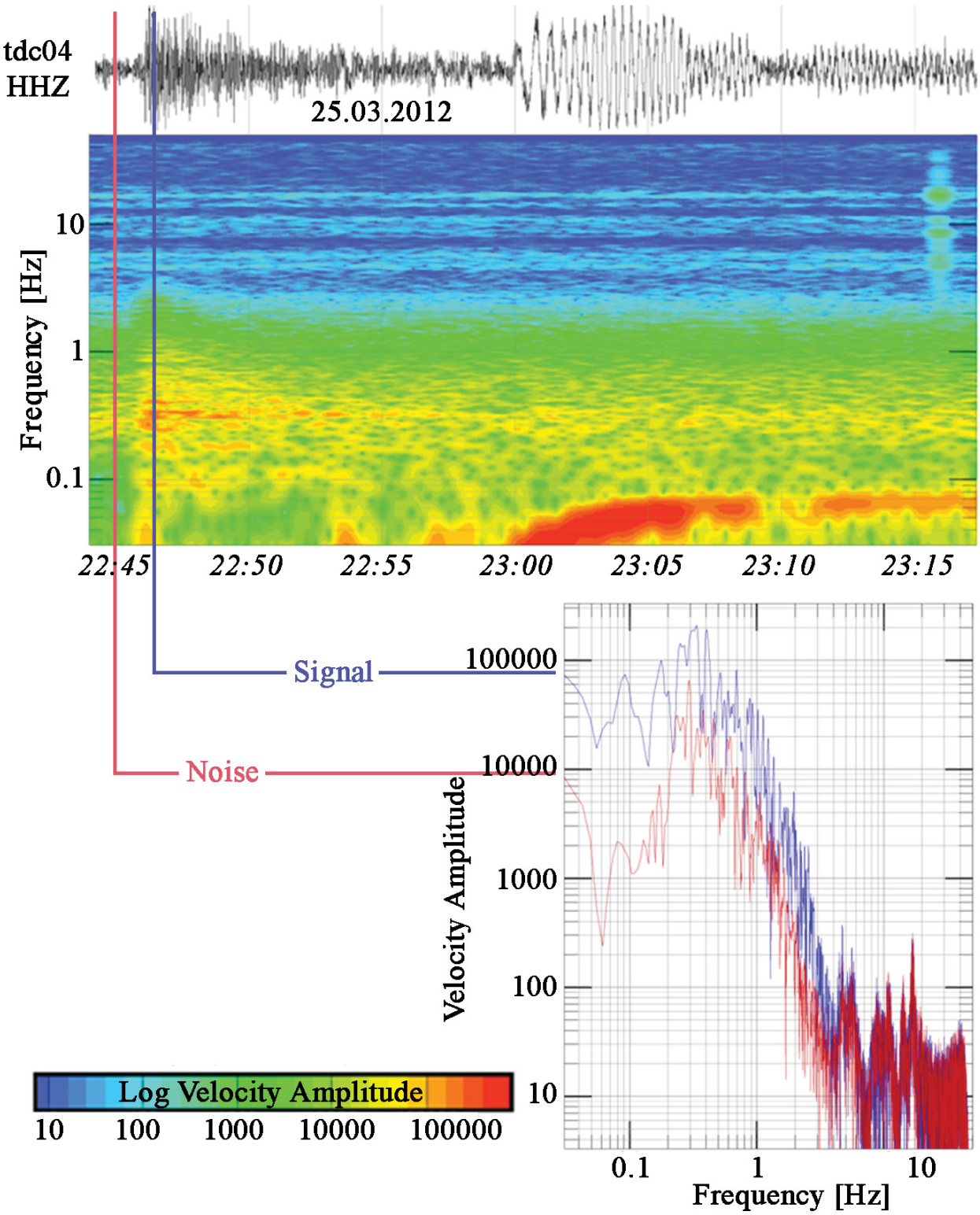

Figure 14: Spectrogram and spectral plot of the Chile earthquake (25.03.2012 22:37:06, mb: 7.1) registered with OBS tdc04 on the vertical component.

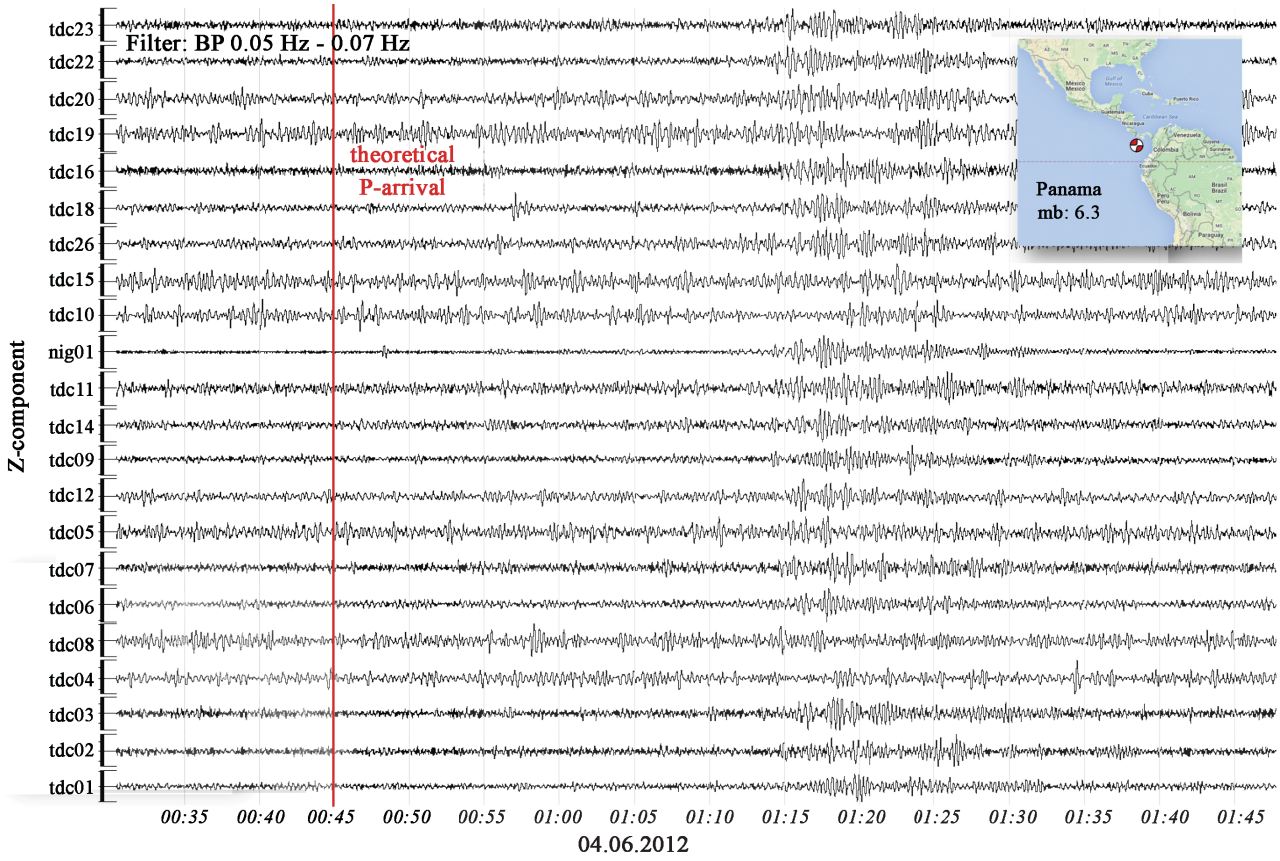

Figure 15: Panama earthquake (04.06.2012 00:45:15, mb: 6.3) registered on the vertical components. No clear P-arrival can be observed.

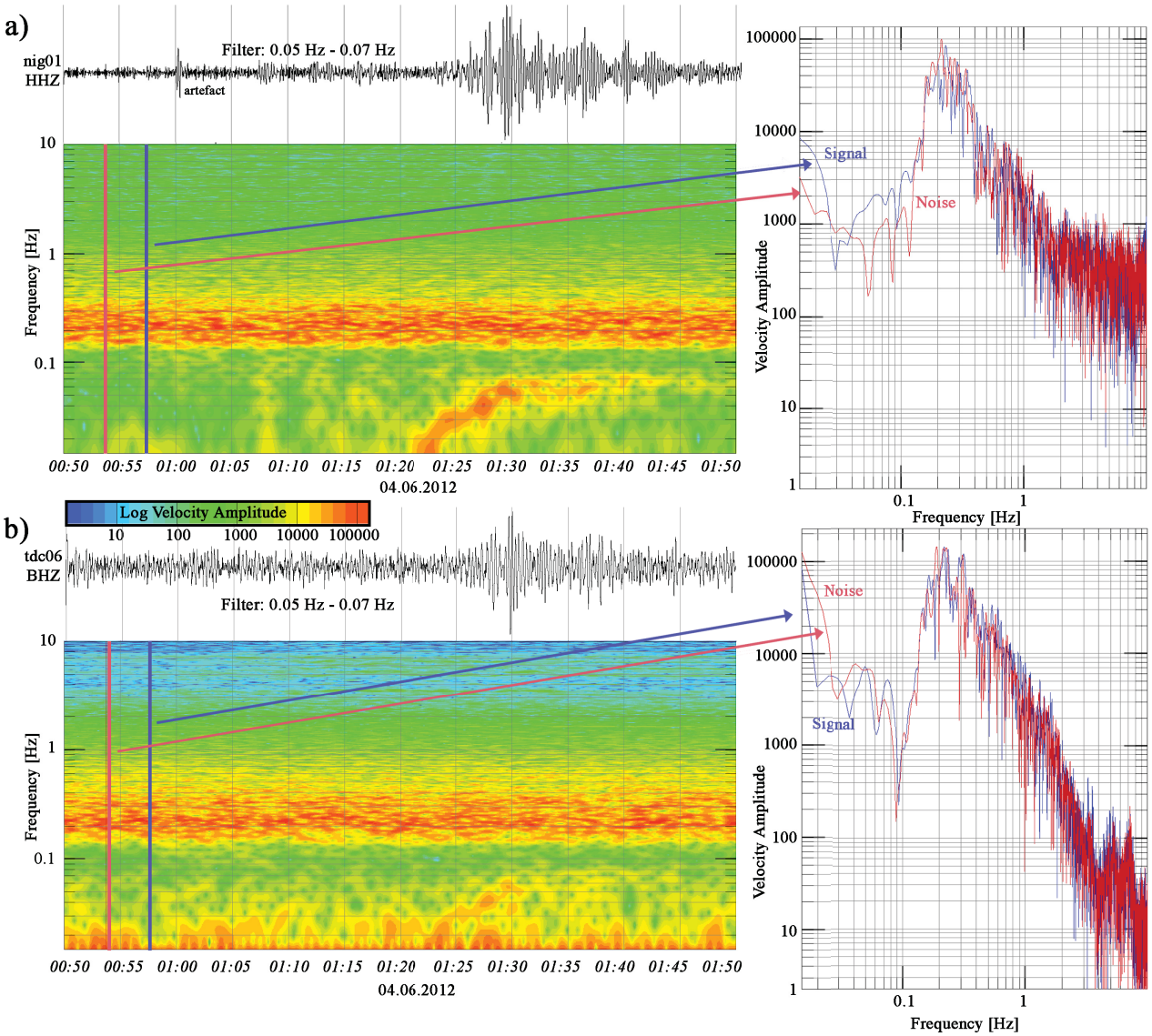

Figure 16: a) Spectrogram and spectral plot of the Panama earthquake (04.06.2012 00:45:15, mb: 6.3) registered with the land station nig01 (vertical component: HHZ). The theoretical P-arrival, calculated for nig01 is at 00:57:13 UTC. b) Spectrogram of OBS tdc06 (vertical component: BHZ). The theoretical P-arrival is calculated to be at 00:57:18 UTC.

2.3.2 Local earthquakes

While teleseismic earthquakes were observed in a low frequency range (0.04-1 Hz), the network registered more than 500 local earthquakes within a high frequency range (5-18 Hz). Figure 17 shows an example of an earthquake, which is located within the network (13.28°W, 32.19°S). In most of the OBS seismograms, the P-arrivals and S-arrivals ($\sim$ 60 s later) are clearly identified. The body wave arrivals are not in seismograms of the land stations (H09N1, H09W1, nig01) due to the high noise level at frequencies above 3 Hz measured at land stations, discussed in chapter 2.2.1. Figure 18 shows a spectrogram of OBS tdc19, calculated for the shown local event. The amplitudes of the signal are higher than the background noise and the P-arrival is significant in a frequency range from 3 Hz to 15 Hz. The S-arrival of the earthquake is also visible at 15:22:25 UTC.

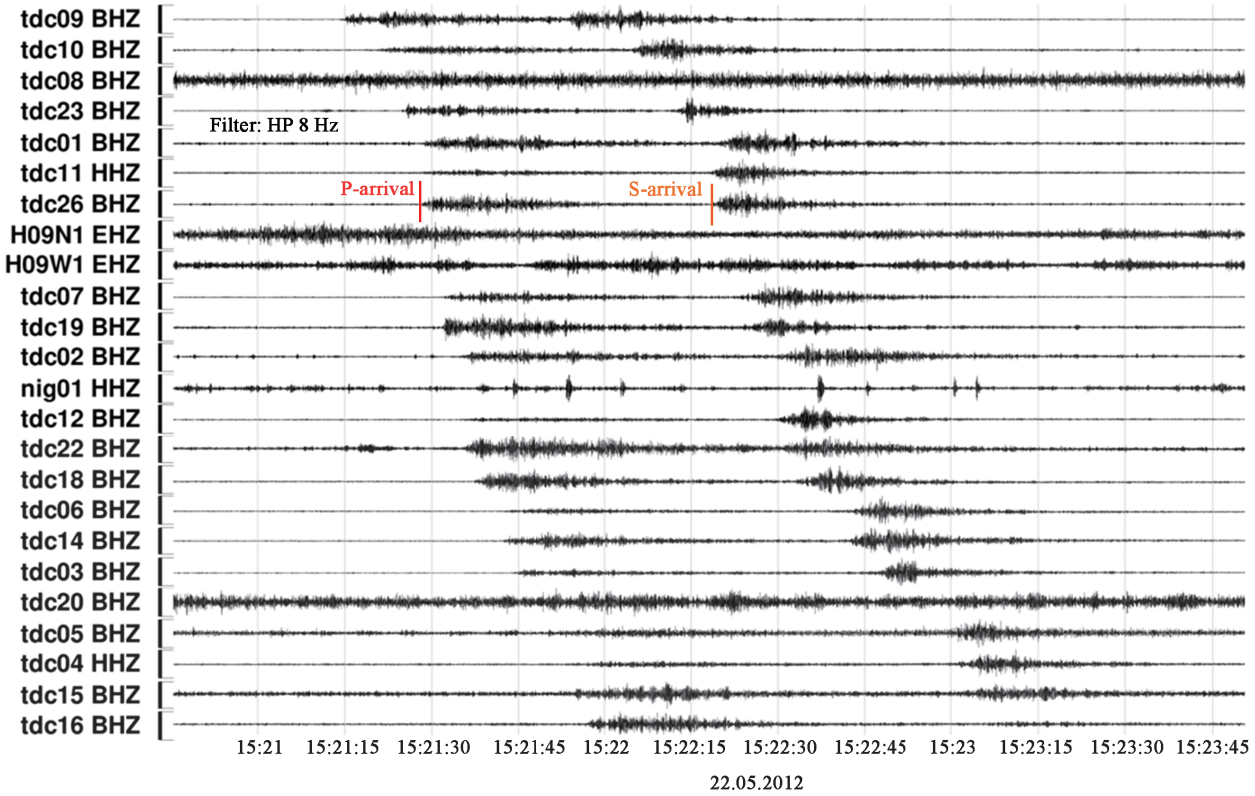

Figure 17: Seismograms of a local earthquake (25.03.2012 15:20:19), location: 13.28°W, 32.19°S.

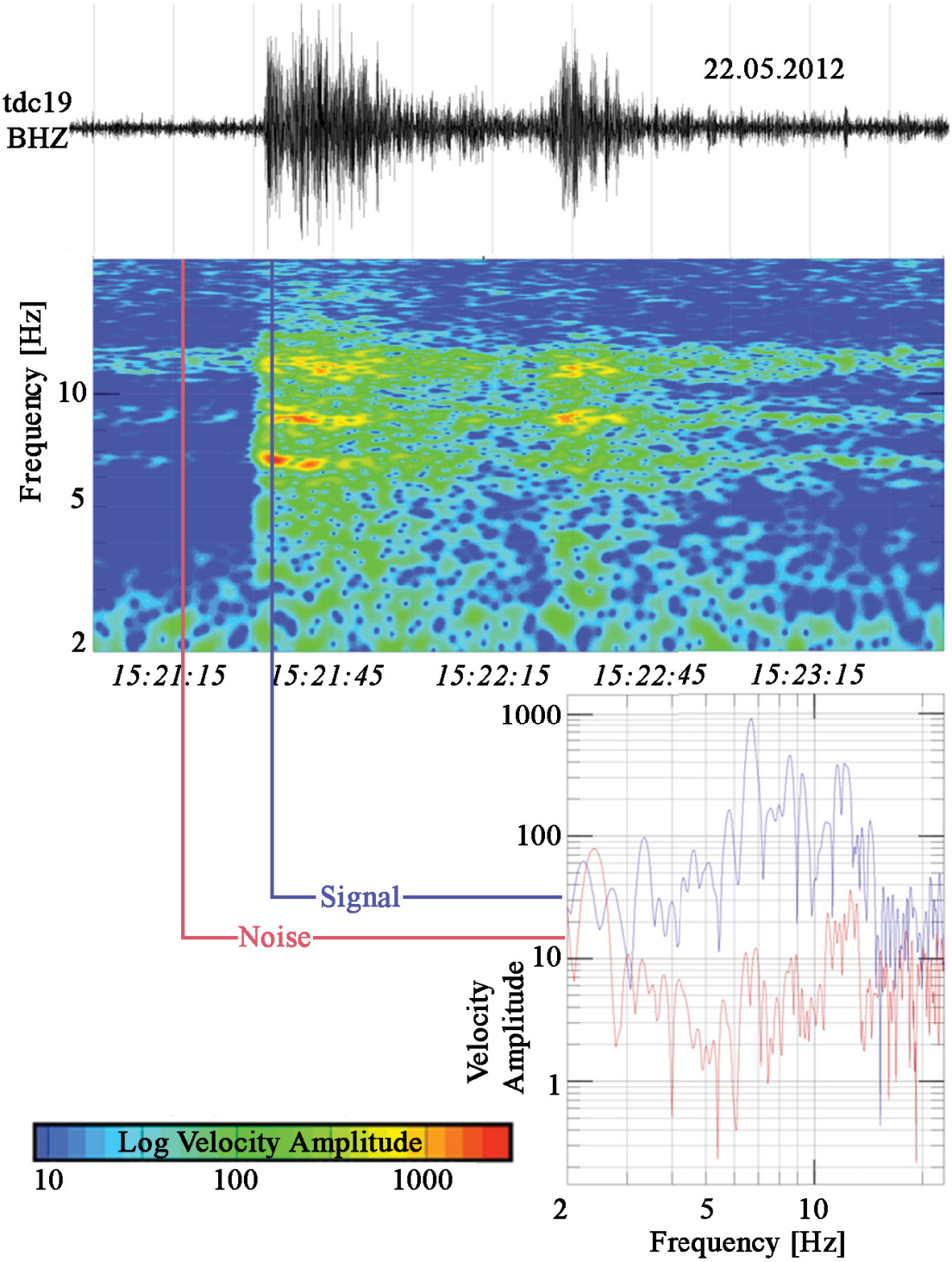

Figure 18: Spectrogram and spectral plot in a frequency range from 2 Hz to 25 Hz of a local earthquake (22.05.2012 15:20:19) registered with the OBS tdc19 on the vertical component.

2.3.3 Whale signals

Apart from seismic signals the OBS registered acoustic signals emitted by marine mammals. These signals travel through the water column with a velocity of 1.5 $\frac{km}{s}$ as a direct wave or as waves reflected at the ocean bottom (multiple). They occur in the same frequency range (>10 Hz) as local earthquakes. Therefore, the automatic detection filter (STA/LTA-filter) for detecting local earthquakes detect also whale signals. These detections had to be removed by hand. Figure 19 shows a seismogram and its corresponding spectrogram of a signal emitted by a whale. The signals occur short and frequently every now and then. I assigned the signals in a frequency range from 13 Hz to 22 Hz to fin whales and the signals from 15 Hz to 17 Hz to blue whales. A small local earthquake occurred at 09:25 UTC. This is a good example how seismic detections are disturbed by whale vocalizations.

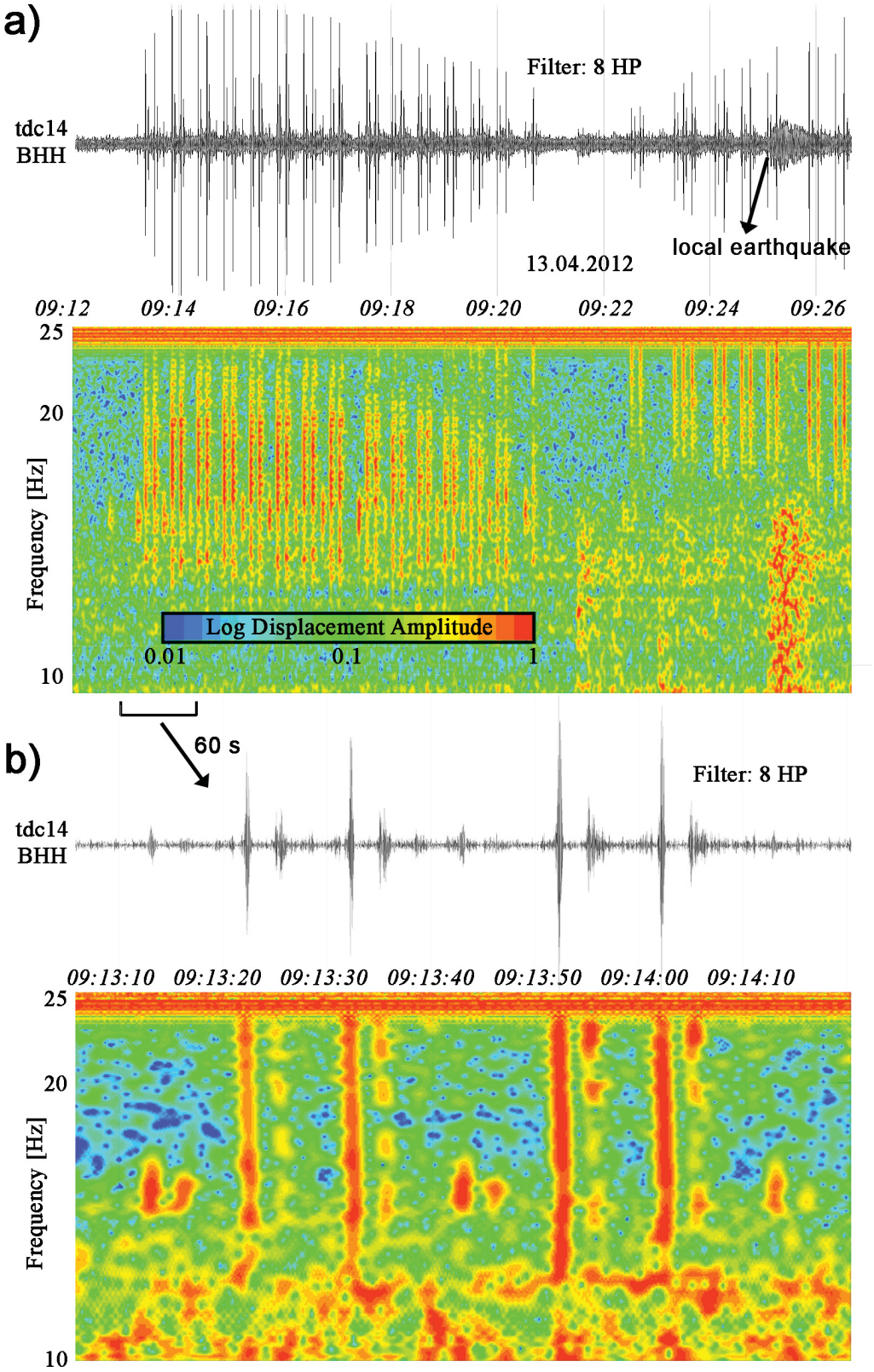

Figure 19: Whale vocalisation registered with OBS tdc14 on the hydrophone component. The seismograms are filtered with a high-pass filter (HP 8 Hz). The corresponding spectrograms are normalized to the frequency. a) 15 minutes time window. b) Enlarged time window of 60 seconds.

3 Preprocessing

Before picking arrivals of teleseismic or local earthquakes for further processing, the seismograms need to be preprocessed. Firstly, the data has to be time corrected in order to consider clock drifts of the recording system. Secondly, a restitution has to be applied to make signals registered with different types of seismometers comparable. In a third step I programmed a polarisation filter to enhance the SNR and to make it possible to differentiate between background noise and the P-arrival of unsuitable earthquakes (see 2.3.1). Although the SNR was enhanced at noisy seismograms, the P-arrivals were nevertheless not visible after applying the polarisation filter.
The following chapters describe the methods and the application of these preprocessing steps in detail.

3.1 Time corrections

The recording system of an OBS is equipped with an internal clock. This clock has to be synchronized with a GPS (**G**lobal **P**ositioning **S**ystem) signal before the deployment of the seismometer. On the ocean-bottom the GPS signal is lost and the clock drifts. After recovering the instruments, the internal clock is synchronised again and the time shift (skew) between the GPS time and the time of the internal clock can be calculated (Suppl. S1). If the internal clock ran faster than the GPS-time, the skew value is positive. In this case the time stamps of the seismograms has to be corrected by a subtraction. If a positive skew is measured, the clock ran faster and time intervals have to be added. Skew values for the OBS tdc02 and tdc18 could not be obtained. Therefore, these values were calculated afterwards with a cross-correlation technique of ambient noise (Geissler pers. comm.). Figure 20 shows the skew values for all used OBS related to one year. The values range between -1 s and +1 s. Most of the OBS have a positive skew, which means that the internal clock runs slower than GPS time.
In the year 2012 a leap second was applied to UTC (**C**oordinated **U**niversal **T**ime) due to

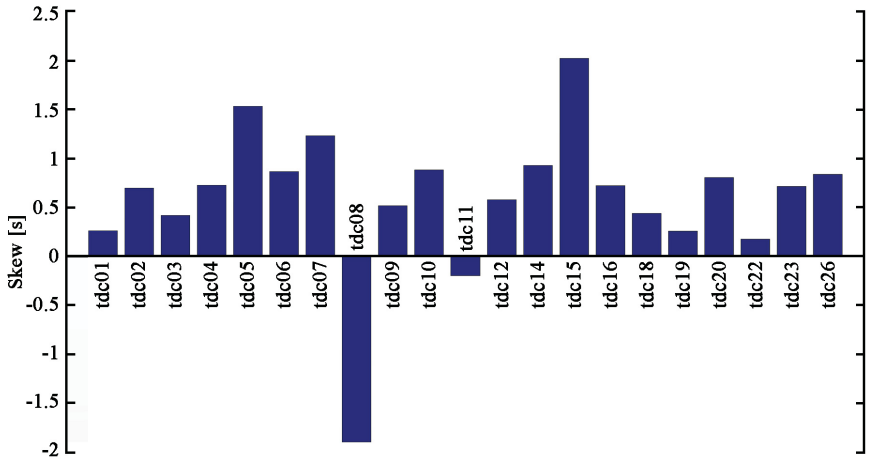

Figure 20: Skews of OBS.

irregular changes in Earth's rotation. Recorders on the ocean bottom were not connected to a GPS signal at that day (30.06.2012) and therefore miss this information. I calculated time shifts for each day, assuming a linear clock drift during the whole year and considering the leap second. Thereafter, I corrected the time stamps for the whole dataset for each day. All corrections were made with an Antelope software program *alter_timestamps*, which changed the time-shift information in the header of the mseed-files. The required parameter file is stored on the enclosed storage system. This file contains old and new calculated time stamps for all mseed-files. The software implemented the time shifts by changing the sample rates of the seismograms (e.g. 50 Hz to 50.0002 Hz or to 49,9998 Hz). This can cause problems in further processing steps or by using different software.

3.2 Restitution

Seismometers register ground motions and convert it into an electrical signal. The recording system of a seismometer consists of several sequences. The seismometer and its included amplifiers influence the incoming signal like a high-pass filter for the ground displacement. Frequencies above the eigenfrequency of the seismometer are registered proportional to the amplitude of the incoming signal. Amplitudes of frequencies below this eigenfrequency are damped (Fig. 22). The damping coefficients are described by the transfer function of a seismometer. Every seismometer has its own transfer function described by poles and zeros. The real ground motion has to be reconstructed from the recorded signal by the transfer function. This is called restitution.
Signals at very low frequencies (<0.1 Hz) serves as input for the tomography. Therefore, the signals are influenced by the transfer function of the recording seismometers (Fig. 22). Before I cross-correlate travel time residuals of earthquakes, I had to restitute the signals according to their corresponding transfer function to ensure that time shifts caused by using different types of instruments are eliminated.

3.2.1 Transfer function

The value of the transfer function $H(i\omega)$ for a mechanical seismometer is obtained by dividing the amplitude of the output signal A_0 by the amplitude of the input signal A_i (derivation described in Scherbaum (2013)).

$$|H(i\omega)| = \frac{A_0}{A_i} = \frac{\omega^2}{\omega_0^2 - \omega^2 + 2i\omega\epsilon} = \frac{\omega^2}{\sqrt{(\omega_0^2 - \omega^2)^2 + 4\epsilon^2\omega^2}}. \tag{1}$$

The transfer function $H(i\omega)$ in dependency of $s = i\omega$ is obtained by a Laplace-Transformation of the equation:

$$s^2 X_r(s) + 2\epsilon s X_r(s) + \omega_0^2 X_r(s) = -s^2 U_g(s) \tag{2}$$

$$\Leftrightarrow H(s) = \frac{X_r(s)}{U_g(s)} = \frac{-s^2}{s^2 + \omega_0^2 + 2s\epsilon}. \tag{3}$$

The order of equation 3 shows that the transfer function of the mechanical seismometer consists of two poles and two zeros. The zeros are at zero and the poles s_{P_1} and s_{P_2} can be calculated by the zeros of the denominator.

$$H(s) = \frac{-s^2}{(s - s_{P_1})(s - s_{P_2})}, \tag{4}$$

$$\begin{aligned} s_{P_{1,2}} &= -\epsilon\sqrt{\pm}\epsilon^2 - \omega_0^2 \\ &= -h\omega_0 \pm \omega_0\sqrt{h^2 - 1} = -(h \pm \sqrt{h^2 - 1})\omega_0. \end{aligned} \tag{5}$$

The difference between a mechanical and an electrodynamical seismometer is a factor ω, which is multiplied to the denominator in 3 due to the proportionality of the input signal to velocity. Hence, the transfer function for a electrodynamic seismometer can be written as

$$|H(i\omega)| = \frac{\omega^3}{\sqrt{(\omega_0^2 - \omega^2)^2 + 4\epsilon^2\omega^2}}. \tag{6}$$

At present time, Velocity-Broad-Band feedback seismometers are used, where the output signal is derived from the force, which is necessary to keep the flexible seismometer mass calm. The deviation of the mass relative to the frame is measured very sensitive and corresponding to that value a current is generated, which is fed into a coil. This coil forces the mass, so that the mass moves with the frame. This feedback system behaves like an electrodynamic seismometer. Therefore, the same transfer function can be used.

3.2.2 Restitution and simulation

As mentioned before, the input signal has to be reconstructed by the transfer function of the seismometer. The Laplace transform of the input signal $U_i(s)$ is yield by dividing the Laplace transform of the output signal $U_0(s)$ by the transfer function $H(s)$:

$$U_i(s) = \frac{U_0(s)}{H(s)}. \tag{7}$$

Figure 21a demonstrates that the input source spectrum, which arrives at the seismometer, is multiplied with the amplitude function of the recording system to obtain the recorded output spectrum. To reconstruct the input source spectrum, the recorded output spectrum has to be multiplied by the inverse transfer function (Fig. 21b).
While figures 21a and 21b describe ideal cases without any noise, real records are highly influenced by noise, caused by the seismometer itself, weather conditions etc. (see 2.2.1). This noise would be amplified when multiplied with the inverse transfer function as shown in Fig. 21c. The increased noise can be observed in a higher amplitude range than the main signal. To minimize this kind of noise, a high-pass filter is applied before the multiplication with the inverse transfer function. The combination of a restitution and a high-pass filter is called 'simulation' due the simulation of a seismometer with a higher eigenfrequency than the existing. The simulation increases the pass band of the seismometer and therefore frequencies below the eigenfrequency of the seismometer are observable.

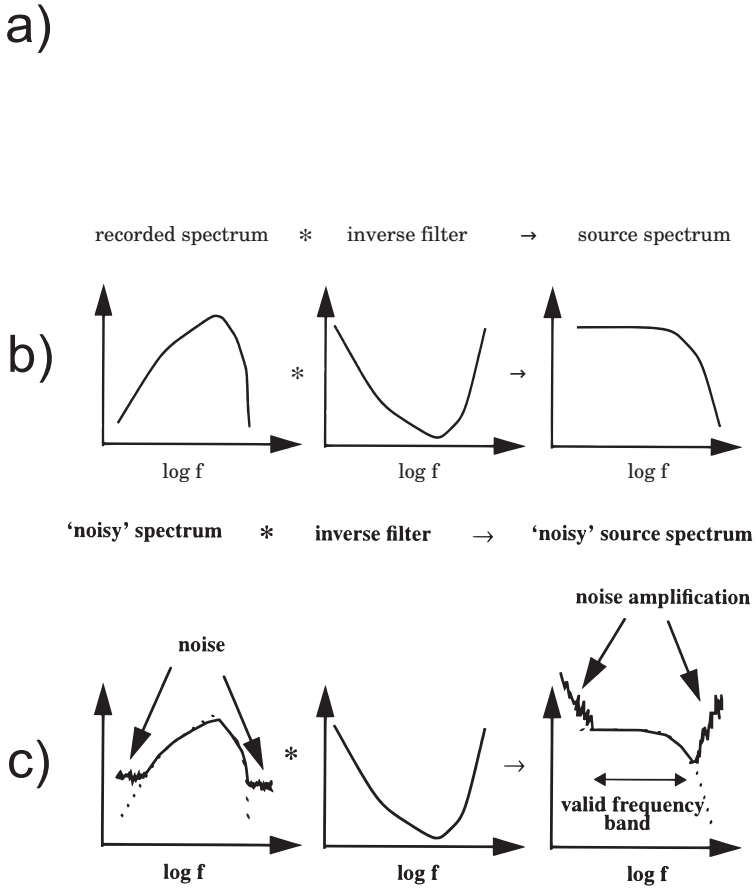

Figure 21: a) Recording of ground motion. b) Restitution of a ground motion for a noisfree case. c) Restitution of a noisy ground motion: the noise is amplified. Source: Scherbaum (2013).

3.2.3 Application of restitution

In this study many different types of seismometers and hydrophones are used (see 2.1). Figure 22 shows the velocity-amplitude and phase frequency response functions of different types of used instruments. The main frequency range used for the tomography is marked by black vertical lines. Different damping values as well as phase shifts are applied to the same incoming signals. Figure 23a shows the signals registered at the hydrophone and the vertical seismometer component of OBS tdc01. A remarkable time shift is observed between the two signals caused in the phase response of the respectively instruments. Before I used the signals for further processing, I applied a restitution. For this purpose, I construct an inverse filter by turning the nominator and denominator of the transfer-function, given by poles and zeros in transfer-function sheets corresponding to each seismometer. Thereafter, I applied this filter in addition to the above mentioned high-pass filter. This yielded the restituted signals. Figure 23b shows the coincidence between the restituted signals. The source code for the restitution program (restitution.mat) is stored on the enclosed storage system.

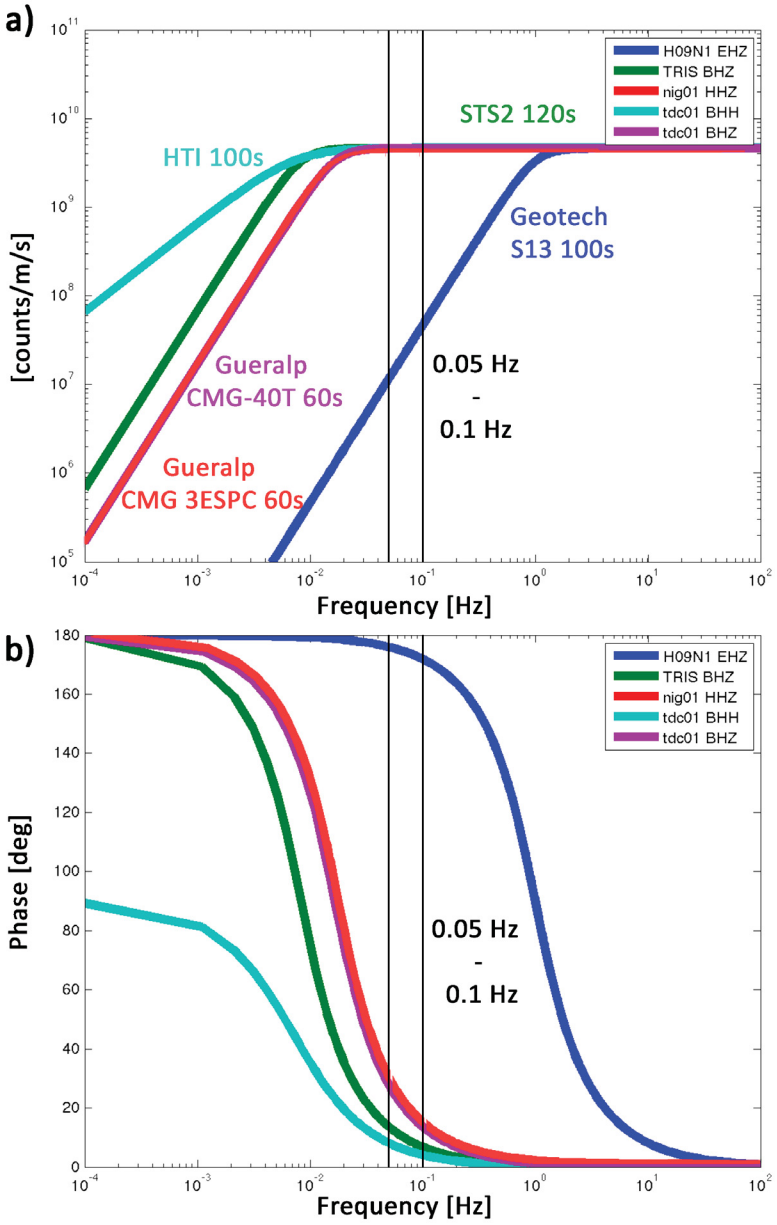

Figure 22: a) Velocity amplitude frequency response functions of different instruments. b) Velocity phase frequency response functions.

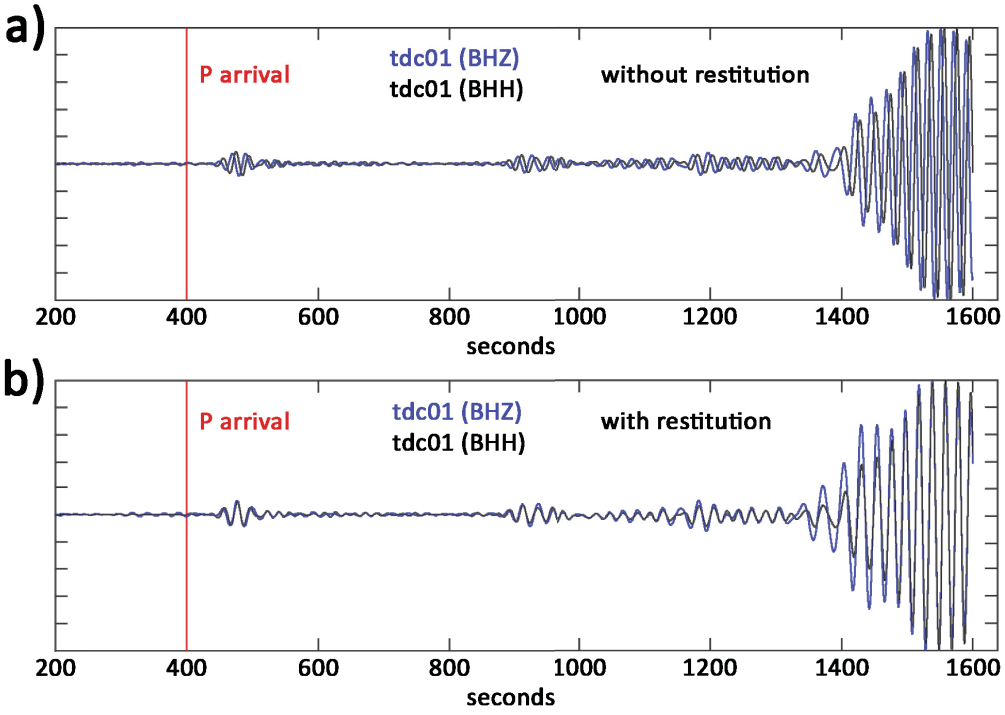

Figure 23: Hydrophone (black) and seismometer (blue) signal of an earthquake. a) The traces are trend and mean removed, bandpass filtered and normalized. b) These traces are processed like a) and additionally high-pass filtered (HP 1800s) and restituted.

3.3 Polarisation filtering

To investigate the Earth's upper mantle, arrival times of body waves are need. Unfortunately, the dataset contain many teleseismic earthquakes with only visible surface waves (see 2.3.1). In order to enhance the SNR of the seismograms and perhaps resulting clear P-arrival, I programmed and applied a polarisation filter. The following two chapters describe the theory (source: Maercklin (2002)) and the application of this filter with attached examples. The corresponding MATLAB source code (*Polarisation.m*) is stored on the enclosed storage system.

3.3.1 Theory

P- and S-waves show a high degree of linear polarisation. This means, that the particle motion of a P-wave is confined to a single plane, while e.g. particle motion of noise is not confined to a direction. The particle motion of a P-wave coincides with the propagation direction for that wave and is perpendicular to the azimuth of propagation for an S-wave. A hodograph (complex particle motion trajectory) can be fit to an ellipsoid in a least square sense by means of a covariance analysis. A three-component covariance matrix $\mathbf{M}$ for a time window of N samples centred around the signal can be written as

$$\mathbf{M} = \begin{pmatrix} Var(X) & Cov(X,Y) & Cov(X,Z) \\ Cov(Y,X) & Var(Y) & Cov(Y,Z) \\ Cov(Z,X) & Cov(Z,Y) & Var(Z) \end{pmatrix}. \tag{8}$$

$\mathbf{M}$ is symmetric, has real non-negative eigenvalues, and its eigenvectors present the principal axes of an ellipsoid that fits best to the date (least squares). The three eigenvectors $\vec{V_j}$ and their associated eigenvalues λ_j satisfy the equation

$$\mathbf{M}\vec{V_j} = \lambda_j \vec{V_j}. \tag{9}$$

The eigenvalues are orthonormal and have unit length, while the length of each axis of the polarisation ellipsoid is $\sqrt{\lambda_j}$. The eigenvalues are commonly sorted in decreasing order ($\lambda_1 \geq \lambda_2 \geq \lambda_3$). The eigenvector $\vec{V_1}$ is associated with the largest eigenvalue λ_1 and points into the main polarisation direction.
The direction of polarisation and the rectilinearity (RL) can be calculated from the components of the eigenvectors $\vec{V_1} = \begin{pmatrix} x_1 \\ y_1 \\ z_1 \end{pmatrix}$ corresponding to the largest eigenvalue λ_1. The polarisation direction can be described by a horizontal azimuth angle ϕ and by the deviation from the vertical direction or apparent incidence angle θ of the P-wave with

$$\theta = \arctan\left(\frac{\sqrt{x_1^2 + y_1^2}}{z_1}\right) = \arccos(|z_1|) \tag{10}$$

$$\textbf{and} \tag{11}$$

$$\phi = \arctan\left(\frac{y_1}{x_1}\right). \tag{12}$$

RL indicates the degree of linear polarisation of an event:

$$RL = 1 - \left(\frac{\lambda_2}{\lambda_1}\right), \tag{13}$$

with the two largest eigenvalues $\lambda_1 \geq \lambda_2$. Values of this definition range between $RL = 0$ for elliptical or undetermined polarisation, and $RL = 1$ for exactly linear polarisation.

3.3.2 Filter application

The RL in addition with the orientation of the polarisation ellipsoid ($\vec{V_1}$) can be used to construct a polarisation filter within a moving time window. A multiplication of RL, eigenvectors and filtered data yields the polarisation filtered results.

$$Xpol(t) = Xfil(t) * RL(t) * x_1(t) \tag{14}$$
$$Ypol(t) = Yfil(t) * RL(t) * y_1(t) \tag{15}$$
$$Zpol(t) = Zfil(t) * RL(t) * z_1(t). \tag{16}$$

Before applying polarization filtering the data are typically filtered with a (zero-phase) bandpass.
To demonstrate the method, figure 24a shows a filter application of seismograms with clear P-arrivals and a known orientation of the horizontal components of the seismometer. Figure 24b shows an example, where the desired effect failed and no P-arrival is observable after filter application.
The P-arrival is already visible at ∼16:48 UTC and the S-arrival at ∼16:53 UTC in the raw vertical component (HHZ) of the nig01 seismograms (24a). By applying a bandpass filter (0.05-0.07 Hz), a clear P-arrival is observable at all components. The RL reach a value close to one at the occurrence of the P- and S-wave. During this stable rectilinearity, the corresponding azimuth is measured to be -60°, which coincides with the backazimuth of -310 measured from the station to the event. The dip angle is measured to be $\sim 60°$, which correlates to an calculated dip angle of 30° ($90° - 30° = 60°$). The resulting polarisation filtered seismograms show a distinct P-arrival at all components. The noise, visible at the horizontal components is completely suppressed in the polarisation filtered seismograms within a small time span before the P-arrival. Signals in the time span between the P- and S-arrivals are minimized at all components. This example demonstrates that the polarisation filter is able to suppress non-linear noise and therefore enhance the SNR.
Figure 24b shows the application of the polarisation filter applied to OBS tdc06 seismograms. The Panama earthquake (Fig. 15) serves as an example with no visible P-arrivals. The theoretical arrival times were calculated to arrive at 00:57:18 UTC and the surface waves at $\sim$ 01:15 UTC (both marked in the bandpass filtered seismograms (Fig. 24b). The arrivals of the surface waves are not even recognizable in this enlarged window. Although, the eigenvalues show some small time spans of high rectilinearity, the polarisation filtered seismograms do not show any distinct arrivals, which were suitable for cross-correlation techniques. In summary, therefore, it can be said that the SNR can be enhanced, if signals are observable in bandpass filtered seismograms. If not, this method does not help making arrivals visible. The polarisation filtering could not increase our amount of suitable earthquakes for the tomography.

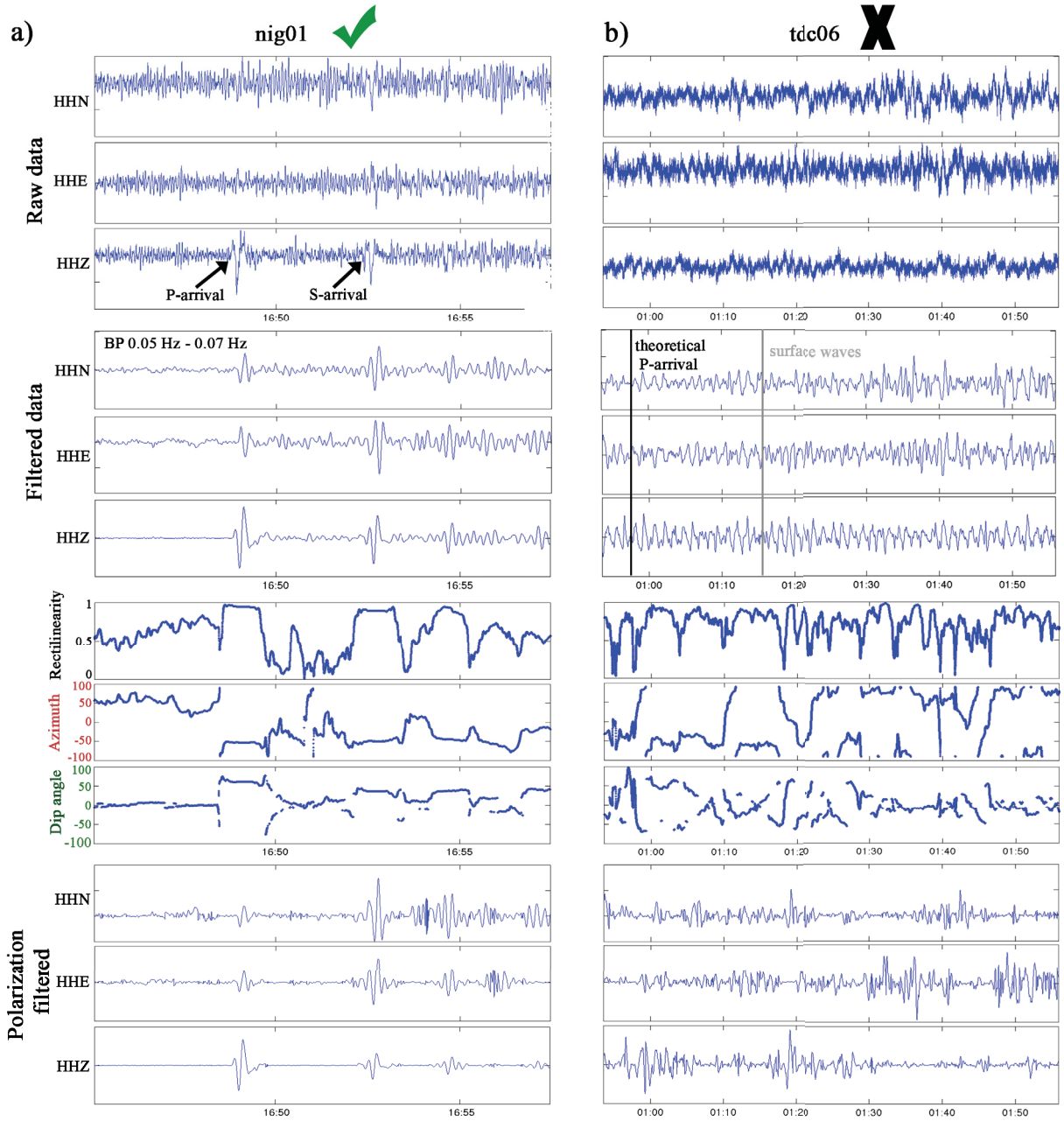

Figure 24: Polarisation filtering. a) nig01 seismograms of an earthquake with visible P-arrivals. b) OBS seismograms with no visible P-arrivals. See text for further explanations.

4 Method: Tomography

Seismic tomography is a method to image the Earth's deep interior using data provided by seismic waves. These waves are generated by earthquakes. The wave velocity is controlled by physical properties like elastic, anelastic and anisotropic parameters as well as the density and the temperature of the passed material. The travel time of a wave through the Earth gives an average of the wave velocity along the ray path. If rays pass all parts of a region in many different directions, it is possible to unscramble the times and to determine the velocity variations of each small part in the region. Figure 25 shows ray paths of two different earthquakes arriving at a network consisting of seismological stations. Waves, which pass an anomaly, arrive later at receiver stations in comparison to waves which do not pass this anomaly.
Plumes or hotspots are characterized by hot temperatures and melt, which implies lower velocities compared to the ambient mantel material. Such anomalies in the Earth interior can therefore be identified by using the tomography techniques.

In this study I performed a finite-frequency tomography with relative travel time residuals obtained from teleseismic earthquakes. The method I used is deployed by Schmandt and Humphreys (2010). In the following sections I will give a short overview of the theory and describe how I obtained the travel times residuals.

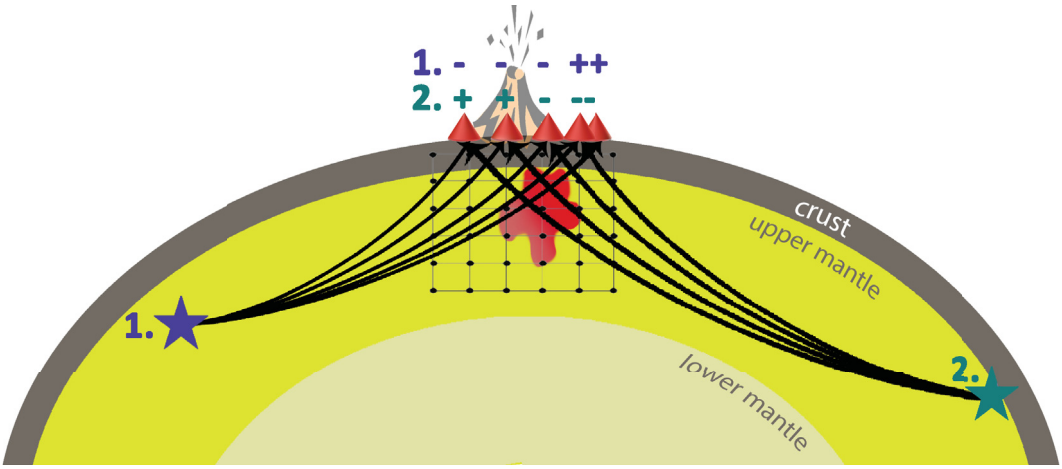

Figure 25: Principle of detecting an anomaly with a tomography.

4.1 Finite-frequency tomography

For many years, seismic body waves (P and S) were treated and calculated like optical rays (ray theory). This is a good approximation but limited: Objects, which are smaller than the Fresnel zone cannot be identified. The recently developed finite-frequency tomography uses sensitivity kernels of different frequency bands and therefore allows to resolve small-scale heterogeneities. High frequency measurements are rather influenced by small-scale heterogeneities than low frequency measurements. In ray theory the infinitesimally narrow ray path calculated by Snell's law is the only region where the travel time is sensitive to the Earth's structure. In kernel theory, this region is not sensitive, but the area which surrounds this ray paths. This is the striking

differences between ray theory and kernel theory.
Schmandt and Humphreys (2010) tomography method is based on an approximation of the Frechet-kernel theory (Dahlen et al., 2000; Hung et al., 2000). It suggests that the ray velocity is influenced by the material surrounding the geometrical ray in a specific area. The volume which describes this area of sensitivity is a hollow banana-shaped region or kernel. The kernels have also become known as banana-doughnut kernels due to their shape (Marquering et al., 1999) or are named 'Fréchet kernels' after the French mathematician Maurice Fréchet.

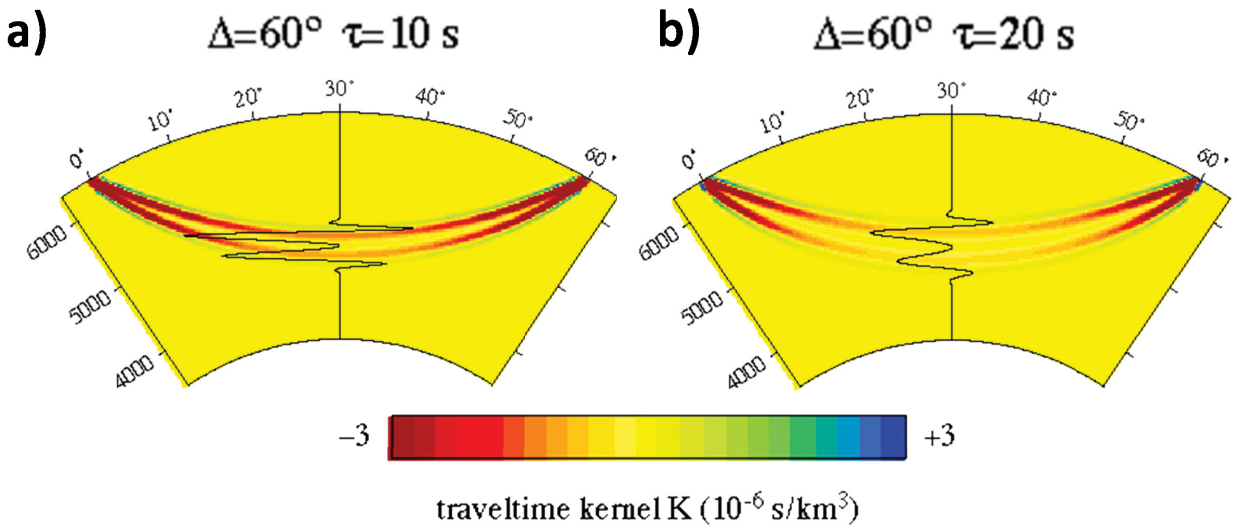

Figure 26: Ray-plane cross-section through Fréchet kernel from Hung et al. (2000). a) Sensitivity K for a P-wave in an epicentral distance of 60° for a period of 10s. b) Sensitivity (P-wave) for a period of 20 s.

Figure 26 shows the sensitivity of Fréchet kernels for a P wave of 60° epicentral distances for a period of 1 s and 20 s. The width of the kernel increases with the period of the corresponding body waveform: The larger the period, the larger the ray-normal distance of the kernel.
Figure 27 shows the Fréchet kernels calculated by Dahlen et al. (2000) and the approximate kernels calculated by Schmandt and Humphreys (2010) and used in this study.

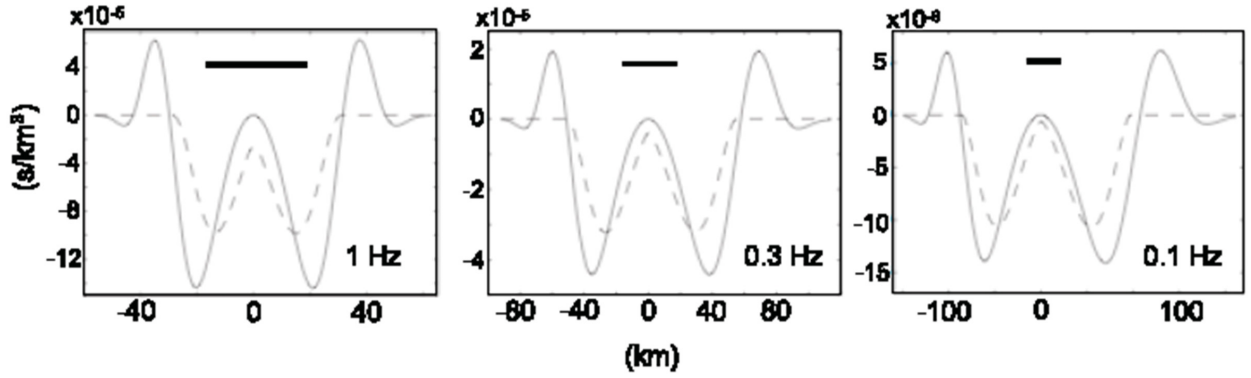

Figure 27: Comparison of the approximated first Fresnel zone sensitivity kernel (dashed line) calculated by Schmandt and Humphreys (2010) and used in this study and the Fréchet kernel calculated by Hung et al. (2000) at a distance of 250 km away from the receiver along the ray path for different frequencies (1Hz, 0.3 Hz and 0.1 Hz). The solid black line defined a 35 km length scale, which is typically used for node spacing. From Schmandt and Humphreys (2010).

(Schmandt and Humphreys, 2010) calculated the sensitivity of the kernels in an approximated first Fresnel zone, which radius R_{F1} can be described by

$$R_{F1} = \frac{\sqrt{\lambda D_R}}{2}, \tag{17}$$

in relation to the distance D_R along the ray path and the wavelength λ of the transmitted signal. λ can be replaced by $\lambda = \frac{c}{f}$ with the frequency f and the velocity of the medium c. The approximated Fresnel zone is an interpolation between radii, calculated for rays at 5°increments of epicentral distances Δ_{i5}. The authors calculated the relative amplitude of sensitivities K as a function of the ray-normal distance R_n by

$$K(R_n) \approx A \sin(\pi(\frac{R_n}{R_{F1}(D_R, \omega, \Delta)})^2). \tag{18}$$

A is a constant and R_{F1} is the radius of above-mentioned approximated first Fresnel zone as function of the distance along the ray path D_R, the frequency band ω (f in equation 17) and the epicentral distance Δ).
The integrated value in the volume of the kernel along the ray is equal to the ray theoretical sensitivity along the ray length L:

$$\int_V K(x)dV = \int_L \frac{1}{v(D_R)}dL. \tag{19}$$

In this equation is $K(x)$ the 3D kernel and $v(D_r)$ is the reference velocity as a function of the position along the ray. The 1D ak135 velocity model (Kennett et al., 1995) is used for calculating $v(D_R)$. By implementing equation 19 in equation 18, the approximation of the sensitivity (K_{F1}) in the first Fresnel zone can be written as

$$K_{F1}(R_N, D_R, \omega, \Delta) \approx [\frac{\int_L \frac{1}{v(D_R)}dL}{\int_{V_{F1}} \sin(\pi(\frac{R_N}{R_{F1}(D_R,\omega,\Delta)})^2)dV_{F1}}] * \sin(\pi(\frac{R_N}{F1_r(D_R, \omega, \Delta)})^2). \tag{20}$$

V_{F1} is the volume of the approximated first Fresnel zone about the ray length L.

To consider the uncertainties of the geometrical ray locations, the sensitivities are smoothed into ray-normal direction. This smoothing widths increase with distance from the receiver along the ray paths and starts with 2 km at the crust-mantle boundary to 15 km at the bottom of the model (Schmandt and Humphreys, 2010).

The tomography is an inverse problem, which has to be solved. In a first step a three-dimensional model space has to be configured, which contains voxels of specific sizes (Fig. 25). A sensitivity kernel for every single ray, which arrives at a network is calculated. Afterwards, the sensitivity for each voxel, which is covered by the kernel is stored in a matrix **G**. At the end the matrix consists of sensitivities for each voxels (rows) for every ray (column). The sensitivities for the voxels along the raypath multiplied with the velocity perturbations for these voxels $\vec{m}$ summed up yields the travel time residual $\vec{d}$ ($|G\vec{m} = \vec{d}|$). The velocity perturbations $\vec{m}$ are unknown, therefore this equation has to be solved by an inversion.
It is necessary to regularize the model. While a good fit to the delays yields in an model with high roughness, a smoothed solution implies large errors in the delay times. Therefore Schmandt and Humphreys (2010) minimize the equation

$$c = ||\mathbf{Gm} - \mathbf{d}||^2 + k_1||\mathbf{Lm}||^2 + k_2||\mathbf{m}||^2 \tag{21}$$

with an iterative method for linear least-squares problems (Paige and Saunders, 1982). **G** is the above-mentioned matrix that relates the model parameter **m** (vel. perturbations) to the observed delay times **d**.

The matrix **L** defines a depth dependent smoothing operators, while k_1 defines the relative weight of the smoothness and k_2 the norm damping constraint. These values are selected by an L-curve, which shows the norm of the regularized solutions and variance reduction with varying damping coefficients (k_2). Eberhart-Phillips (1986) suggests that a good compromise between model normalization and variance reduction can be found at the turning point of the L-curve. The L-curve for the Tristan dataset is shown in figure 36. I chose a smoothing factor of 3 and a damping factor of 6 to regularize the inversion. Figure 28 shows a cross section of the tomographic results for different smoothness and damping values. While small damping and smoothing values 28a result in a model with high roughness and sharp spatial changes in the structure, high values result in a smooth solution. The cross correlation in between shows the tomographic results with the chosen values.

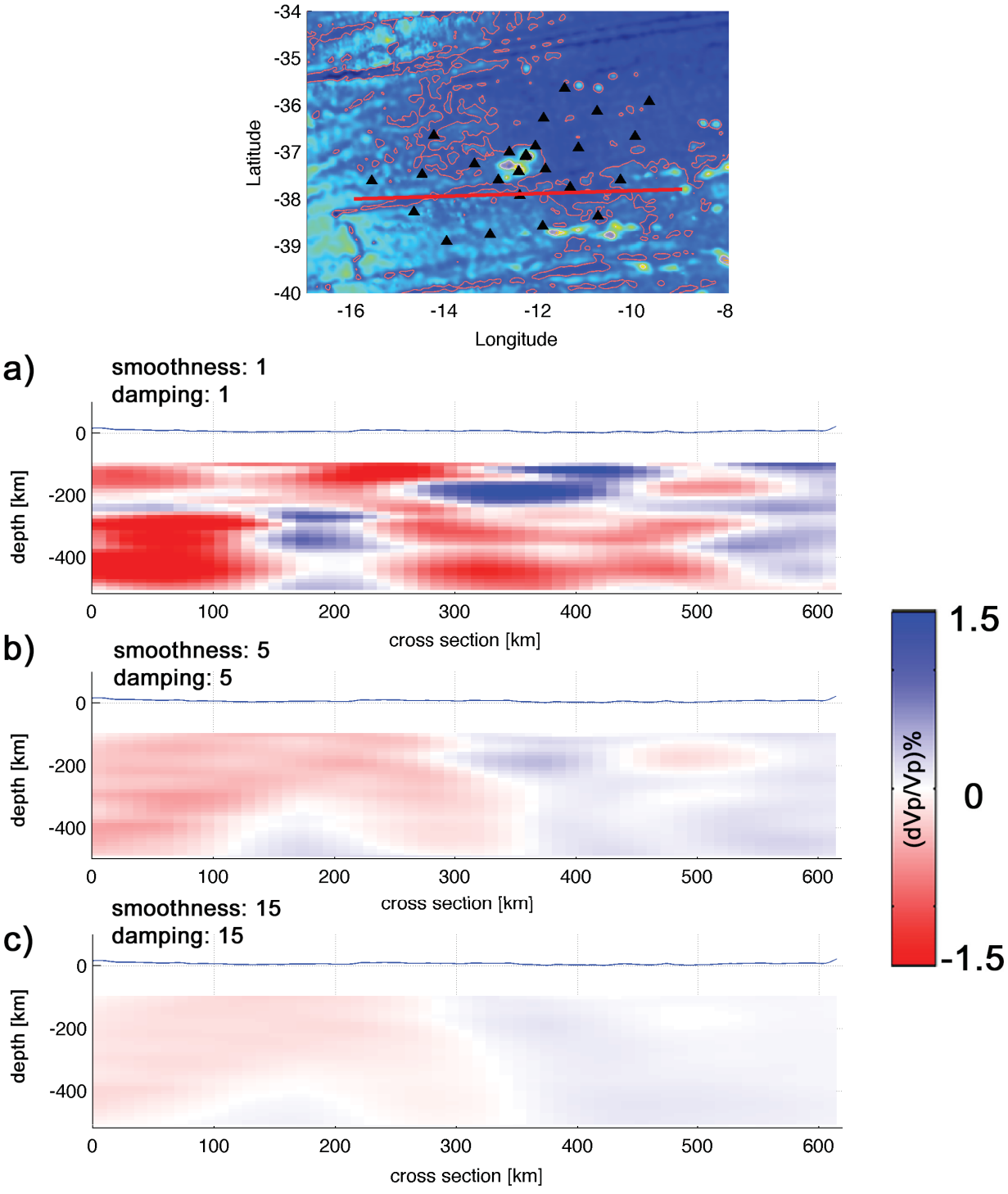

Figure 28: Cross sections of tomographic results along the red marked line in the map. a) Results with smoothness and damping equal to 1. b) Results with s=d=5. c) Results with s=d=15.

4.2 Relative travel time residuals

For the tomography I used relative travel time residuals of P- and PKP-arrivals obtained from teleseismic earthquakes. After the preprocessing steps (see section 3), I picked the arrival times and selected suitable earthquakes. These earthquakes are plotted in figure 34.

4.2.1 Cross correlation

To obtain the relative travel times, I correlated the arrivals of all network stations for each earthquake in different frequency bands. In a first step, the waveforms are aligned to a theoretical arrival time, calculated with the ak135 (Kennett et al., 1995). Afterwards, a small window containing the signal to cross-correlate is chose. Finally, the multi-channel cross-correlation procedure (VanDecar and Crosson, 1990) find the best fit of the waveforms. The corresponding shift, which is applied to each waveform is the travel time residual. This procedure is demonstrated in figure 29.
It is assumed that individual rays from an earthquake travel along the same raypath through the lower mantle and diverge beneath the seismic network within our model (Youssof et al., 2015). Therefore, the travel time residuals are only disturbed by anomalies within our model area. As a consequence, the mean values is removed and relative travel time residuals are obtained. Figure 30 shows the relative travel time residuals of the Chile earthquake for each

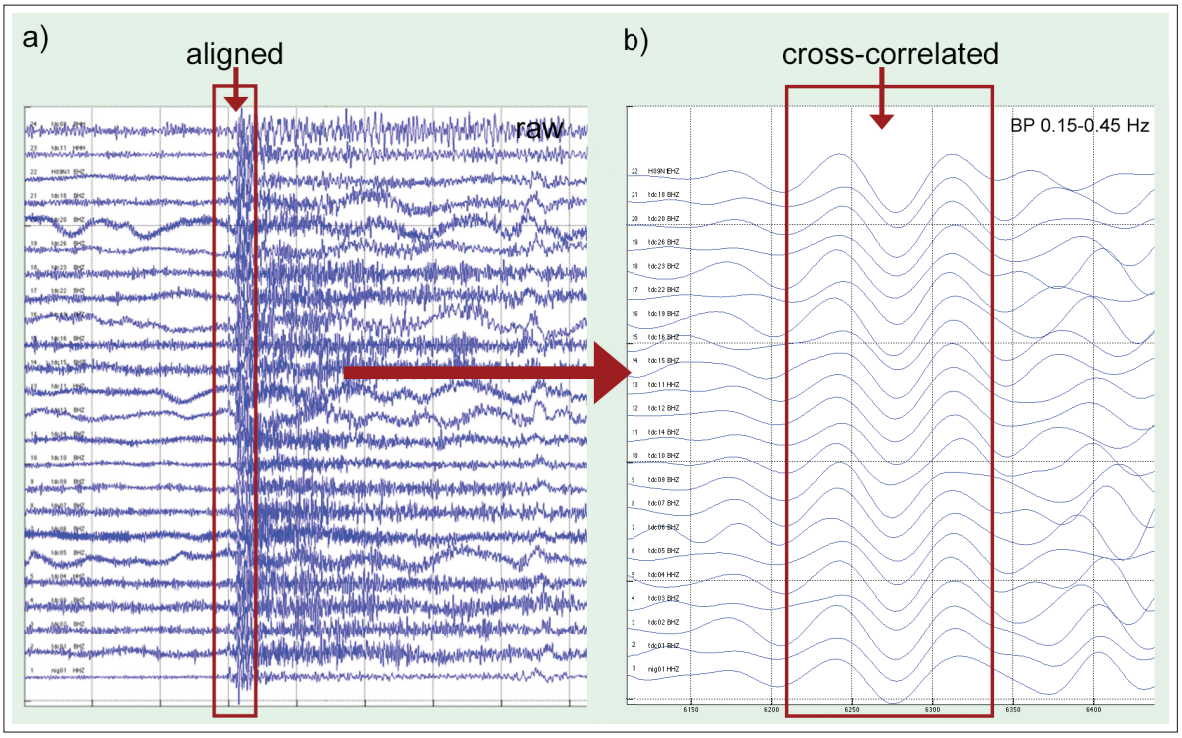

Figure 29: Cross-correlation of a Chile earthquake (35.03.2012). Filtered with a bandpass filter with centre frequency of 0.3 Hz and a half width of 0.15 Hz.

station. The colour indication changed from orange (later arrivals) in the southwest of the network to green (earlier arrivals) in the northeast. This indicates that rays arriving in the southwest of the network pass a lower velocity zone compared to the rays arriving at stations

in the northeast. Rays arrive late at both land stations (nig01 and TRIS). This is caused by the missing crustal and elevation correction (see 4.2.2).
I obtained 884 relative travel time residuals in 6 different frequency bands. The residuals are stored on the enclosed storage system (*residuals.dat*)

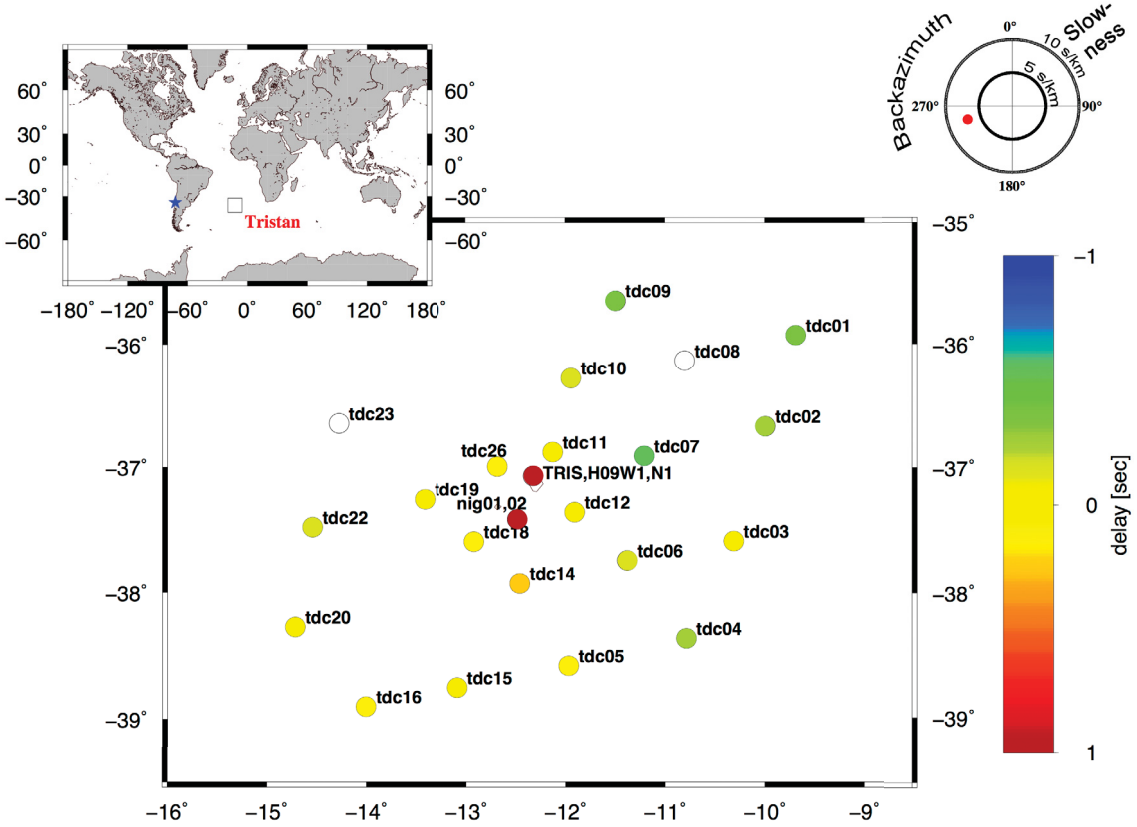

Figure 30: Relative arrival times at stations of the network. Locations of the earthquake is plotted top left. The averaged backazimuth and slowness values are plotted at top right.

4.2.2 Crust correction

A ray measured at a network station passes also the heterogeneous crust. To invert the data only for the upper mantle velocity perturbations, the crustal effects have to be removed. Here, I described the procedure.
The crustal travel times were calculated with the classical ray theory. Pierce points, where the arriving rays pierce the Moho are used to calculate the ray paths to the receivers and their corresponding travel times within the crust. The slowness of the ray p and the mean velocity v in the crust can be used to calculate the incident angle i of the arriving ray

$$p = \sin\frac{i}{v} \Rightarrow i = asin\frac{p}{v}. \tag{22}$$

I assumed a homogeneous crust to a depth of 10 km for the OBS stations ($Moho_{OBS}$) and calculated the distance from the pierce point to the receivers at the ocean-bottom by

$$s = \frac{Moho_{OBS} + elevation_{OBS}}{\cos(i)}, \tag{23}$$

where the elevations for the OBS are negative and therefore subtracted. The corresponding travel time correction is afterwards calculated with

$$t_{OBS} = \frac{s}{v}, \tag{24}$$

where v is a velocity in the crust and assumed to be 5.8 $\frac{km}{s}$. These and the following crustal P-wave velocities are derived from a seismic refraction P-wave model of the Discovery seamount (Keßling, 2008). Although the seamount is located 1500 km away from the archipelago, the Discovery form is comparable to Tristan and provides the only crustal P-wave velocities in this region.

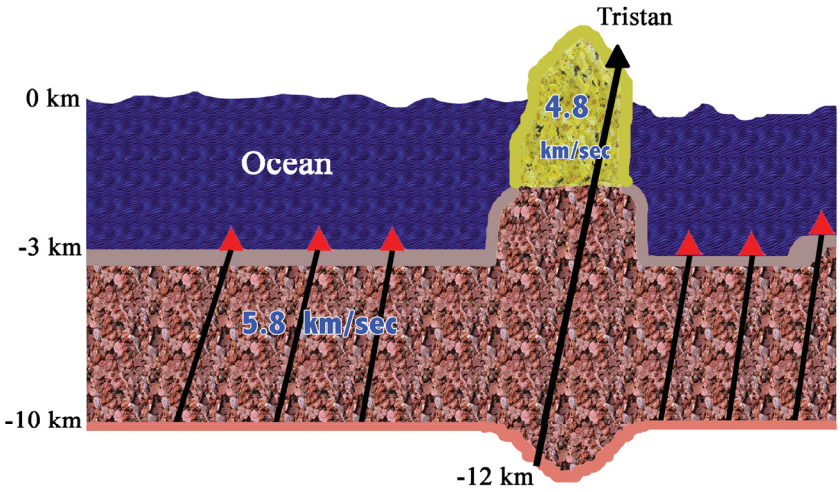

Figure 31: Schematic model of crust correction

To calculate the correction time for the land stations, I assumed a root directly beneath the island of 2 km thickness. Additionally, I assumed a two-layered crust beneath the archipelago. The top layer has a thickness of 4 km with a velocity of 4.8 $\frac{km}{s}$ and the second layer of 8 km thickness has a velocity of 5.8 $\frac{km}{s}$ The distances within the crust and its corresponding travel times are calculated by

$$s1 = \frac{4 + elevation}{\cos(i)} \quad \& \quad s2 = \frac{Moho_{land} + elevation}{\cos(i)} \tag{25}$$

$$\tag{26}$$

$$\Rightarrow t_{land} = \frac{s2 - s1}{5.8} + \frac{s1}{4.8}. \tag{27}$$

Figure 31 shows the assumed crustal model and figure 32 shows the calculated crustal correction values for the Chile earthquake. The correction times for all earthquakes and stations are stored on the enclosed storage system.

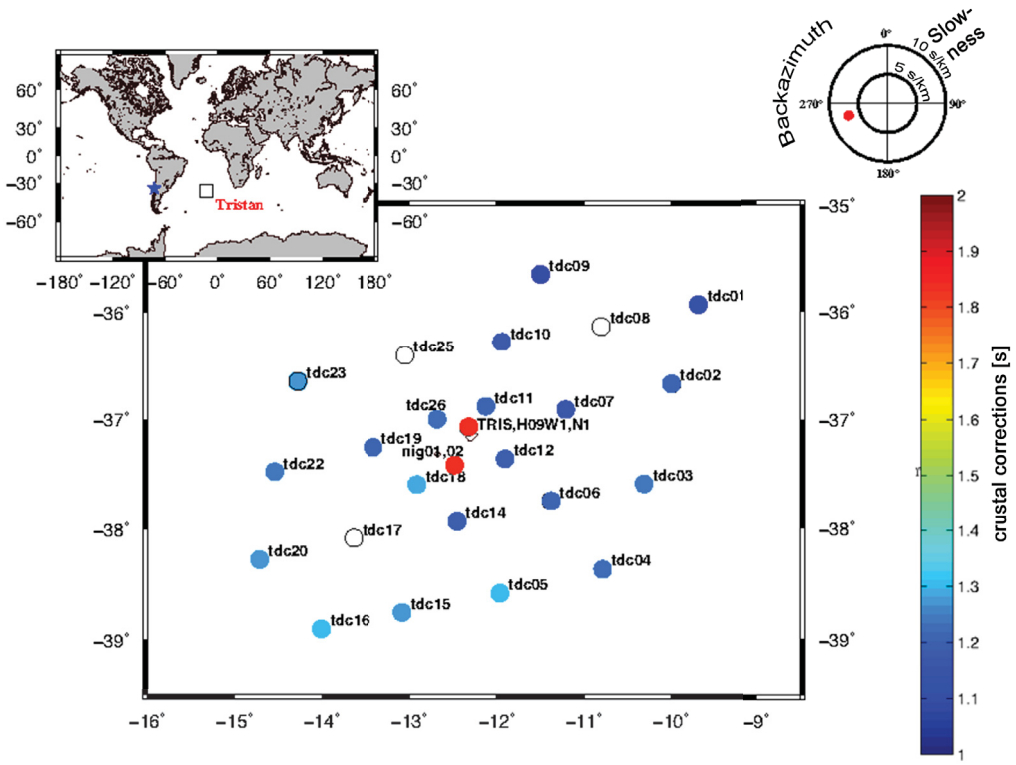

Figure 32: Crustal correction values for different stations calculated for rays arriving from the Chile earthquake. Location of earthquake in top, left edge. Averaged backazimuth and slowness values in the yop right edge.

4.3 Code

The tomographic codes used in this study are developed over many years: Schmandt and Humphreys (2010) started with coding and Bezada et al. (2010) and Youssof et al. (2015) contributed to the codes. Unfortunately, a description of the code has not been published. Therefore, it was a challenge for me to recognize code lines, which I had to change or fit to the Tristan dataset. I added the above-mentioned restitution and crustal corrections to the code. In order to test the resolution of the dataset, I deployed synthetic models with floating cubes or synthetic plumes. Figure 33 illustrates on the one hand the processing steps, which were necessary for the tomography and on the other hand my contributions to the code.

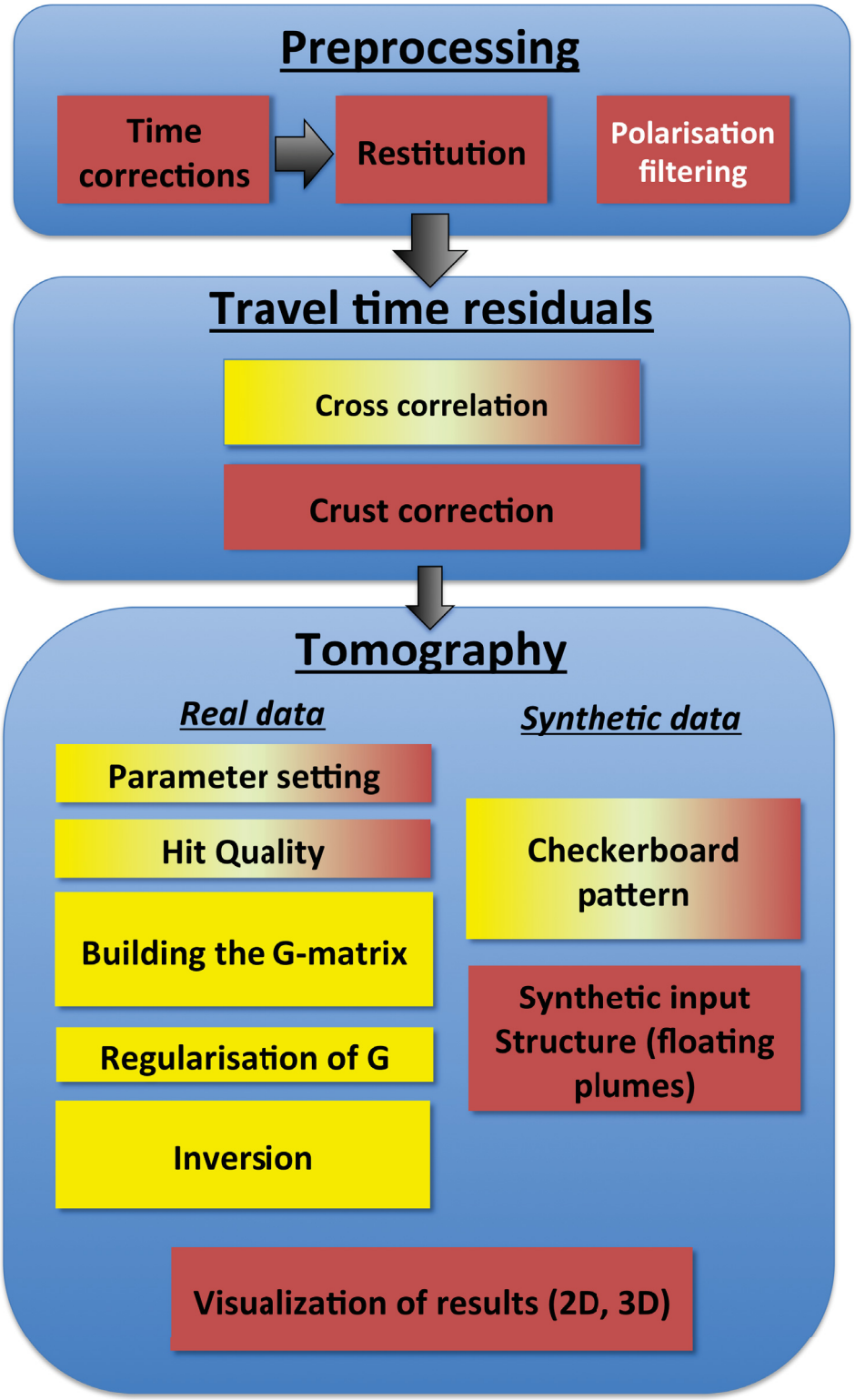

Figure 33: Processing steps of the tomography. Red: My contributions; yellow: untouched code; colour gradient: I fitted the code to the Tristan dataset but I left the remaining calculations untouched.

5 Contributions to scientific journals

In the following I present my first author contributions to scientific journals and manuscripts. I used a seismological dataset acquired with the Maria S. Merian cruises MSM20/2 and MSM 24. Marion Jegen, Wilfried Jokat and Wolfram Geissler wrote the proposal for the project.

5.1 Hunting for the Tristan Mantle Plume - An upper mantle tomography around the volcanic island of Tristan da Cunha

Antje Schlömer[1], Wolfram H. Geissler[1], Wilfried Jokat[1,2], Marion Jegen[3]

[1] *Alfred Wegener Institute, Helmholtz Centre for Polar and Marine Research, Am Alten Hafen 26, D-27568 Bremerhaven, Germany*
[2] *University of Bremen, Geoscience department, Bremen, Germany*
[3] *Geomar, Helmholtz Centre for Ocean Research Kiel, Wischhofstr. 1-3, 24148 Kiel, Germany*

In review at *Earth and Planetary Science Letters*.
Received: June 16th, 2016
Received in revised form: September 1th, 2016

In this paper, we investigated the upper mantle structure beneath the island of Tristan da Cunha by using the seismological dataset.
In a first step, I preprocessed the data, which included time corrections and the removal of the instrument response. After that, I picked all P- and PKP-arrivals of teleseimic earthquakes and performed a cross-correlation to obtain the relative travel time residuals. These residuals were used to calculate the finite-frequency tomography. The initial code is deployed by Schmandt and Humphreys (2010). But I modified it and implemented new calculations for the crust correction and synthetic resolution tests.
Moreover, I visualized the data and prepared all figures for this article. Finally, I interpreted the data and wrote the manuscript.
Wolfram Geissler supervised my scientific work at AWI. He and Wilfried Jokat revised the manuscript and contributed to the results in various discussions.

5.2 Seismicity in the vicinity of the Tristan da Cunha hotspot - Interaction of plate tectonics and mantle plume presence

Antje Schlömer[1], Wolfram H. Geissler[1], Wilfried Jokat[1,2], Marion Jegen[3]

[1] *Alfred Wegener Institute, Helmholtz Centre for Polar and Marine Research, Am Alten Hafen 26, D-27568 Bremerhaven, Germany*
[2] *University of Bremen, Geoscience department, Bremen, Germany*
[3] *Geomar, Helmholtz Centre for Ocean Research Kiel*

To be submitted to *Journal of Geophysical Research.*

In this paper, we investigated the local seismicity in the Tristan da Cunha region using the seismological preprocessed dataset.
I picked the P- and S-arrivals of the earthquakes. Subsequently, I localised the events and calculated their magnitudes. Finally, I interpreted the data and wrote the manuscript. Wolfram Geissler revised the manuscript.

5.3 Merging electromagnetic & seismological data to reveal the upper mantle beneath the Tristan da Cunha hotspot

Antje Schlömer[1], Kiyoshi Baba[2], Jin Chen[3], Wolfram H. Geissler[1], Wilfried Jokat[1,4], Marion Jegen[3]

[1] *Alfred Wegener Institute, Helmholtz Centre for Polar and Marine Research, Am Alten Hafen 26, D-27568 Bremerhaven, Germany*
[2] *Earthquake Research Institute, The University of Tokyo, 1-1-1 Yayoi, Bunkyo-ku, Tokyo 113-0032, Japan*
[3] *Geomar, Helmholtz Centre for Ocean Research Kiel, Wischhofstr. 1-3, 24148 Kiel, Germany*
[4] *University of Bremen, Geoscience department, Bremen, Germany*

Prepared for submission.

In this manuscript, we combined the recent results of marine magnetotelluric data with tomographic results of this study. The aim was to reveal the upper mantle beneath Tristan da Cunha in terms of electrical density and velocity perturbations.
The electromagnetic data were processed by Kiyoshi Baba and Jin Chen. Their manuscript is in revision at *Tectonophysics*. I got the processed data by Kiyoshi Baba and visualized them. Finally, I wrote the manuscript.

6 Hunting for the Tristan Mantle Plume - An upper mantle tomography around the island of Tristan da Cunha

6.1 Abstract

The active volcanic island Tristan da Cunha, located at the southwestern and youngest end of the Walvis Ridge - Tristan/Gough hotspot track, is believed to be the surface expression of a huge thermal mantle anomaly. While several criteria for the diagnosis of a classical hotspot track are met, the Tristan region also shows some peculiarities. Consequently it is vigorously debated if the active volcanism in this region is the expression of a deep mantle plume, or if it is caused by shallow plate tectonics and the interaction with the nearby Mid-Atlantic Ridge. Because of a lack of geophysical data in the study area, no model or assumption has been completely confirmed.
We present the first amphibian P-wave finite-frequency travel time tomography of the Tristan da Cunha region, based on cross-correlated travel time residuals of teleseismic earthquakes recorded by 24 ocean-bottom seismometers. The data can be used to image a low velocity structure southwest of the island. The feature is cylindrical with a radius of $\sim$ 100 km down to a depth of 250 km. We relate this structure to the origin of Tristan da Cunha and name it the Tristan conduit. Below 250 km the low velocity structure ramifies into narrow veins, each with a radius of $\sim$ 50 km. Furthermore, we imaged a linkage between young seamounts southeast of Tristan da Cunha and the Tristan conduit.

6.2 Introduction

Tristan da Cunha (TdC) is a small (98 km^2) volcanic island located at the southwestern and youngest end of the aseismic Walvis Ridge in the South Atlantic. The island is situated 450 km east of the Mid-Atlantic Ridge (MAR) (Fig. 34). The TdC archipelago comprises the main island TdC, the uninhabited island Nightingale, the wildlife reserve Inaccessible Island, and a number of smaller islands. The archipelago is part of a province characterized by widely scattered seamounts and small volcanic islands.
TdC has come to be widely accepted to be the youngest surface expression of a deep-seated mantle plume (Tristan plume) (Morgan, 1972; White and McKenzie, 1989; Courtillot et al., 2003). In this context, however, controversy centres on whether the plume played an active or passive role in the Mesozoic opening of the South Atlantic (e.g. Fromm et al., 2015; Jokat et al., 2003).
The known history of the assumed Tristan plume starts $\sim$ 132 Ma or slightly earlier with the emplacement of the Paraná (South America, Brazil) and Etendeka flood basalts (Africa, Namibia) (Fig. 34a) (White and McKenzie, 1989; Gibson et al., 2005). After seafloor spreading started, the ridge-centred plume tail and its associated volcanism formed the Walvis Ridge on the African Plate and the Rio Grande Rise on the South American Plate (O'Connor and Duncan, 1990; O'Connor and le Roex, 1992; Wilson and Guiraud, 1992). The mid-ocean ridge has migrated westwards away from the plume head since $\sim$ 70 Ma. During this latter period, intraplate volcanism occurred on the African Plate has formed a province of seamounts and small, scattered islands (Rohde et al., 2013b; O'Connor and Duncan, 1990).
TdC is assigned to the group of primary hotspots/mantle plumes (Courtillot et al., 2003),

because the Walvis Ridge - Tristan/Gough hotspot track fulfils all the criteria of a classical hotspot track: A continental flood basalt province in the northeast of the aseismic Walvis Ridge is linked to the active ocean island volcano TdC at its southwest end (Fig. 34) (Richards et al., 1989). The volcanic chain forms a clear age-progression parallel to the direction of plate motion over the mantle (O'Connor et al., 2012; O'Connor and Jokat, 2015; Rohde et al., 2013b).

However, inconsistencies compared to a classical hotpot track such as the Hawaiian hotspot track are present: While the northeast (east of $5°W$) end of the hotspot track consists of massive aseismic ridges, the southwest end is characterised by widely scattered seamounts and small islands, suggesting a decrease in vigour.
O'Connor et al. (2012) tried to explain the hotspot tracks in the South Atlantic by the motion of African Plate over multiple plumes rising from the stable edge of the African Large Low Shear Wave Velocity Province (LLSVP). Apart from the plume idea, it was suggested that the active volcanism in this region could be caused by plate tectonics (Anderson, 2005). Foulger and Natland (2003) and Fairhead and Wilson (2005) proposed that changes in relative plate motion led to faulting and fracturing of the oceanic lithosphere for subsequent melt transport towards sites of volcanism.
The basalt geochemistry of rock samples from the Tristan archipelago, the adjacent island Gough Island and nearby seamounts shows an ocean-island-basalt-type pattern, but there are striking differences in their isotopic compositions (Rohde et al., 2013b). Based on determinations of an enriched Gough component and a less-enriched Tristan component, the plume track seems to have bifurcated at $\sim$ 70 Ma into a northern subtrack directed towards TdC and a southern subtrack directed towards Gough (Rohde et al., 2013a,b; Hoernle et al., 2015). To explain these different isotopic compositions, Rohde et al. (2013a) proposed a geochemical zonation of the Tristan plume, which originates from the African superplume boundary.
Gibson et al. (2005) suggested that magmas from TdC, Inaccessible Island and Gough Island contain a deep mantle component originating from recycled metasomatised lithospheric mantle. Other authors have proposed a heterogeneous source at depth, from which melt has been discretely siphoned off to undergo rapid fractionation in conduits, chambers and dikes closer to the surface (Le Roex et al., 1990; Reagan et al., 2008), a branching plume stem, or a plume stem transporting discrete blobs (Rohde et al., 2013b; Hicks et al., 2012).
Another possibility is that plume material flows along the base of the lithosphere towards the nearby MAR (**?**). Petrological investigations of mid-ocean ridge basalts (MORB) from ridge-samples in the Tristan region show an isotopic anomaly, which can be explained by a Tristan mantle plume influence (Schilling et al., 1985; Hanan et al., 1986).
None of these numerous models and assumptions have been tested by direct geophysical observations around the island: Global tomography models (e.g. Ritsema and Allen, 2003) have a poor resolution in the upper mantle (<500 km) in the study area, because of the very low seismological station density in and around the South Atlantic. In order to close this knowledge gap, we acquired continuous seismological data for one year with an ocean-bottom seismometer (OBS) network around the island, which we used to investigate the upper mantle structure beneath TdC by a P-wave finite-frequency travel time tomography.

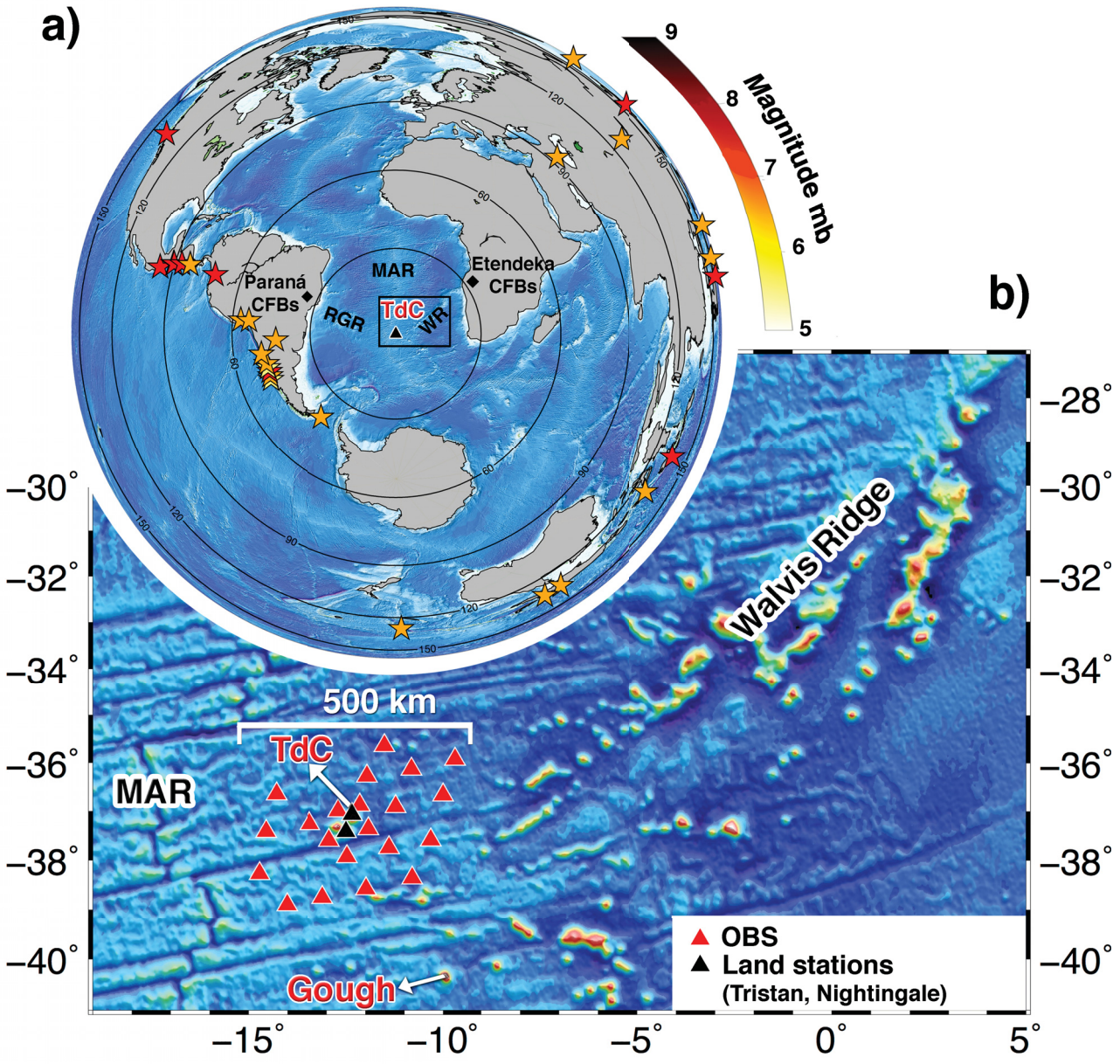

Figure 34: (a) Location map with Tristan da Cunha (TdC) located in its centre and showing the azimuthal distribution of earthquakes (stars) used in this study and their body wave magnitudes (mb) (colour indication with colour scale top right). The concentric circles mark the 30° increments. Black diamonds: Paraná and Etendeka flood basalts. (b) Bathymetric overview (ETOPO2) of the Walvis Ridge - Tristan/Gough hotspot track. Red triangles mark the locations of the OBS stations and the black triangles mark the land stations on the islands used in this study. Abbreviations: CFB - continental flood basalts; RGR - Rio Grande Rise; WR - Walvis Ridge; MAR - Mid-Atlantic Ridge.

6.3 Dataset

We deployed 24 broadband ocean-bottom seismometers (OBS) around the island of TdC and two seismological land stations on Nightingale Island during the R/V Maria S. Merian cruise MSM 20/2 in January 2012 (Fig. 34b). The station network covered an area of 400 km x 500 km around the Tristan archipelago with an average station spacing of approximately 85 km. The western boundary of the array was located 120 km away from the MAR. The instruments recorded seismological data continuously for one year and were recovered during the later cruise MSM 24. Our network consisted of varying types of instruments (Guralp CMG-40T (OBS), Guralp-3ESPC (Nightingale) and STS-2 (TdC)), which are quite different in their frequency responses, especially at lower frequencies. Consequently, to use all available data in this experiment, we corrected all our data for the instrument response. Additionally, we applied time corrections to the OBS data regarding linear clock drifts and a leap second, which occurred in 2012. Two OBS were lost and one OBS did not record any data. We also used all available data from the permanent station TRIS, located on TdC, for our analyses. Unfortunately, TRIS was flooded during that year, and only sparse data were recorded at the beginning of our experiment. To compensate for this, we used data from two hydroacoustic stations from the IMS's 11 (International Monitoring System) both located on the main island TdC and operated by the CTBTO (Comprehensive Nuclear-Test Ban Treaty).

TdC is located close to the "Roaring Forties", a region of strong year-round westerly winds that give raise to noise in the same frequency range (0.1-1 Hz) as numerous body wave arrivals around the microseism peak of ambient oceanic noise (**?**). Because of this, for many earthquakes, we could not identify the P arrival or find any suitable coherent signals at several earthquakes to apply cross-correlation techniques. Fig. 43 in the supplementary material shows an example of an Italian earthquake with magnitude (mb) 6.0, which proved unsuitable for this work because of this problem. Even short distance ($30° - 50°$) earthquakes with magnitude 5, arriving from Ascension Island or the South Sandwich region, could not be used, because only the surface waves were observable. Therefore, we could use a quite limited amount of differential travel time information. We obtained useful coherent teleseismic data at very low frequencies from earthquakes with magnitude larger than 6 within the 'noise notch' at 0.03-0.08 Hz (**?**).

We used the first body wave arrival P, from earthquakes with epicentral distances between 30° and 90°. Additionally, we used PKPdf arrivals from earthquakes with distances greater than 130°.

Fig. 34a shows the azimuthal distribution of earthquakes used in this study. TdC is unfavourable located with respect to plate boundaries, where earthquakes normally occur. Whilst numerous earthquakes arrived at the network from Central and South America, arrivals from the east of our network are rarer and more unevenly scattered. Unfortunately, virtually no suitable events were recorded from the north and south of the network (e.g. South Sandwich Trench) during its deployment.

In summary, after these limitations our study is based on travel time residuals obtained from 30 teleseismic earthquakes with magnitudes larger than 6 registered in 2012 on the vertical components.

6.4 Method

We performed a finite-frequency tomography (Schmandt and Humphreys, 2010; Bezada et al., 2010; Youssof et al., 2015) to resolve the upper mantle structure in terms of P-wave velocity perturbations within a model space beneath the island of TdC. We divided our model space into voxels by parametrizing a non-uniform grid whose cell size increases at the model edges and with depth. The horizontal node spacing starts at 40 km in the network centre and increases to 55 km at the edges of our model space. Cells above 300 km depth are 25 km thick and 50 km at greater depths. Overall our model consisted of 19 layers of 20 longitudinal by 18 latitudinal nodes, totalling 6840 nodes. We performed the tomography in the depth range of 25 to 500 km. These set-up values were selected after performing several synthetic tests and studying checkerboard patterns and images of hit qualities under different parametrization conditions (See 6.5).

The tomography is based on Born-Fréchet kernel theory (Hung et al., 2000; Dahlen et al., 2000) and assumes the ray velocity is only influenced by the area surrounding the direct geometrical ray path. The volume of this area is described by a sensitivity kernel, which determines how sensitive a wave at a specific frequency would be to a small anomaly. The tomography method used in this study is based on the statement that the Fréchet kernel for a differential travel time measurement between two adjacent stations is the difference of its respective kernels (Dahlen et al., 2000). The sensitivity along the classical ray path is zero (Dahlen et al., 2000). For every ray an associated sensitivity kernel in the first Fresnel zone for a specific frequency was calculated and stored in a matrix $\mathbf{G}$. The higher the frequency, the smaller the ray-normal distance of the kernel. $\mathbf{G}$ consists of sensitivities for every ray from a source to a single receiver (rows) for every voxel in our model space (columns). The sensitivity value indicates how strong the ray velocity is influenced by the material of this voxel. This weighting multiplied by the resulting velocity perturbations $\vec{m}$ for each voxel should yield the previous measured relative travel time residual $\vec{d}$: $|\mathbf{G}\vec{m} = \vec{d}|$.

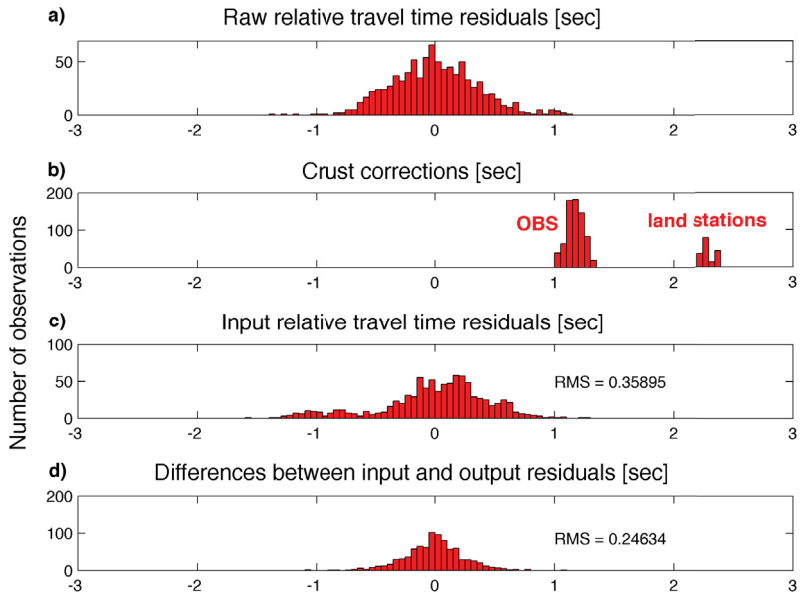

Figure 35: a) Distribution of raw relative travel time residuals. b) Crustal corrections for OBS and land stations. c) Relative travel time residuals with crust correction used in the inversion. d) Differences between input residuals and output residuals. The output residuals ($\vec{d_o}$) are obtained by multiplication of the sensitivities $\mathbf{G}$ and the resulting velocity perturbations $\vec{m}$ ($Diff = \vec{d_i} - \mathbf{G}\vec{m} = \vec{d_i} - \vec{d_o}$).

The relative travel time residuals were obtained from teleseismic earthquakes by a multi-channel cross-correlation (Bungum and Husebye, 1971; VanDecar and Crosson, 1990): In a first step, P and PKPdf arrivals were picked by hand. Unsuitable seismograms and outliers were removed. With the theoretical arrival times calculated with the ak135 1D velocity model (Kennett et al., 1995) and a corresponding mean pick time for all network stations for an event, the single station waveforms were preliminarily aligned within a small bandpass filtered time window. For each possible pair of traces the offset of the maximum of the cross-correlation function relative to an unknown mean time was calculated by least squares. This yielded the relative travel time delays after removal of the mean from the data. This data set consists of 884 relative travel time residuals from bandpass filtered data in six different frequency ranges (Gaussian-Frequency band with centre frequencies of 0.06, 0.08, 0.1, 0.3, 0.5 and 1 Hz) for the inversion. With higher centre frequencies of the applied filter, we received less numerous residuals (Tab. 1). The travel time residuals range from -1.4 to +1.1 s (Fig. 35a).

BP - centre frequency [Hz]	number of residuals
1	70
0.5	72
0.3	99
0.1	304
0.08	214
0.06	125

Table 1: Total amount of residuals in different frequency bands.

The effect of the crustal structure was removed by subtracting elevation-dependent crustal travel times (Fig. 35b) from the residuals. We assumed Moho depths of 10 km (below sea level) around TdC and a small root directly beneath the islands with a Moho depth of 12 km (Geissler pers. comm.). The points at which rays pierced the Moho were used to calculate ray paths within the crust and the corresponding static corrections. We assumed a homogeneous oceanic crust with a velocity of $5.8\frac{km}{s}$ below the OBS stations and a two-layered crust beneath the island stations with a 4 km thick layer of $4.8\frac{km}{s}$ overlying an 8 km thick layer of $5.8\frac{km}{s}$. These crustal P-wave velocities were derived from a seismic refraction P-wave velocity model of Discovery seamount ($42°S, 0°10.02'E$) (Keßling, 2008). Although the seamount is located 1500 km away from TdC, it provides the only direct information on crustal velocities in this region. Fig. 35c shows the relative travel time residuals used for the inversion with an applied crustal correction. The RMS value of these values is 0.36. After measuring relative travel time residuals, correcting for the crustal structure and calculating $\mathbf{G}$, we obtained the velocity perturbations in our model space by minimizing the main equation $|\mathbf{G}\vec{m} - \vec{d}|$ with the least squares method (Paige and Saunders, 1982).

In performing an inversion, it is necessary to apply a model regularization by choosing smoothness and damping values, because the best fit to the delays yields an undesirable model with high roughness. Smoothed solutions imply larger errors in the delay times. We determined a good compromise between model normalization and variance reduction using an L-curve (Fig. 36) and taking the value at the turning point of the curve (Eberhart-Phillips, 1986). We chose a smoothing value of 3 and a damping value of 6 which yielded a variance reduction of 72% after performing 68 iteration cycles. Other choices of these parameters did not significantly

change the size and location of the imaged anomalies in the model. A variance reduction of 72 % resulted in differences between the input residuals and the output residuals (Fig. 35d) with a RMS values of 0.25.

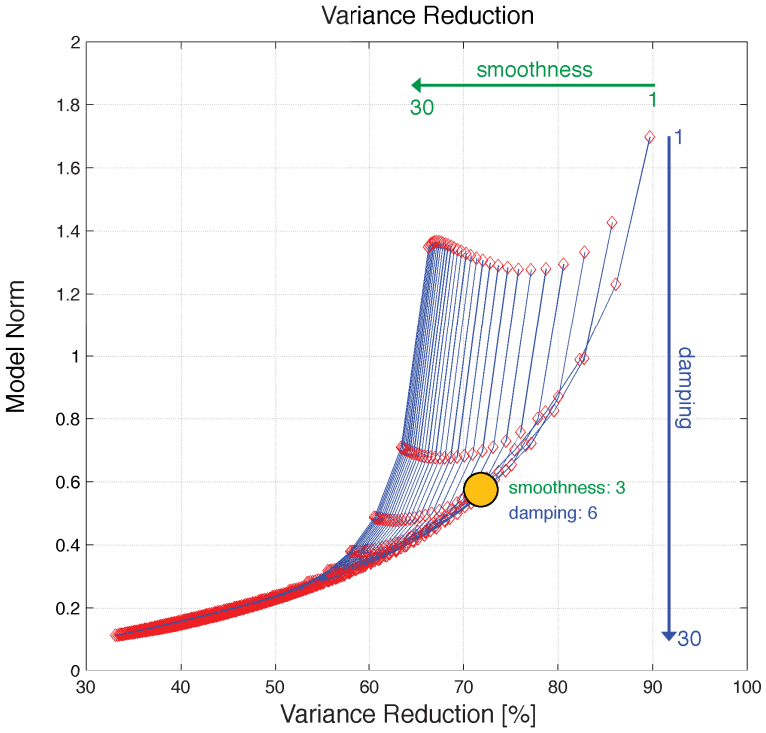

Figure 36: L-curve to find the best values for smoothness and damping. High variance reductions yields in a high model roughness, while a small variance reduction yields in a smooth model. We chose 3 for smoothness and 6 for damping.

6.5 Resolution tests

Because of the unequal azimuthal distribution of earthquakes and a limited number of input data, we performed several synthetic tests to identify, which parts of the tomography model are reasonably well resolved. These tests involved changing parameters including smoothness, damping, voxel sizes and inversion depths to test the robustness and stability of the geometry of our resulting anomalies.

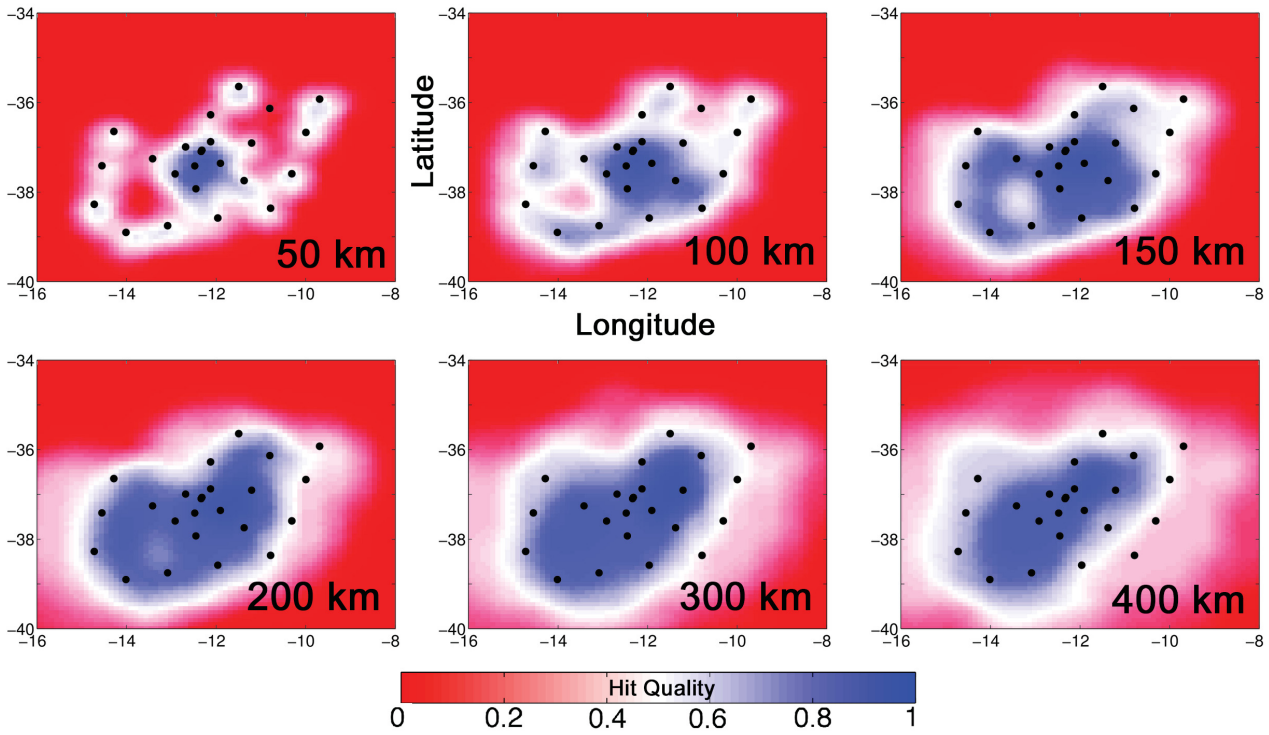

Figure 37: Hit quality in different depth slices. Hit quality ranges from red for unhit nodes to blue for very well hit nodes.

We calculated the ray hit quality of the model for different depth slices (Fig. 37) based on the ray density (Fig. S44). 100% ray density, corresponding to a value of 1, is achieved for a voxel in the model if it is hit by sensitivity kernels of at least 5 rays from each direction. The more hits in a voxel, the better the resolution. We achieved a good hit quality at shallower depths (50-100 km) directly beneath the island. The hit quality decreases with increasing depth (>200 km) east of our array. High hit quality follows the direction of high ray density, which is here mainly directed towards the Central and South American focal zones. Rays from earthquakes located to the east of our network arrived mostly from vertical angles due to large source-receiver distances. With increasing depth (>200 km) the areas of high hit quality become larger, because the radial diameters of sensitivity kernels increase and more cubes are hit by the ray sensitivity kernel.

Checkerboard patterns are a common method to prove the resolution ability of the dataset. We used the forward method $|\mathbf{G}\vec{m}_i = \vec{d}_i|$ to calculate travel time residuals ($\vec{d}_i$) of a known input

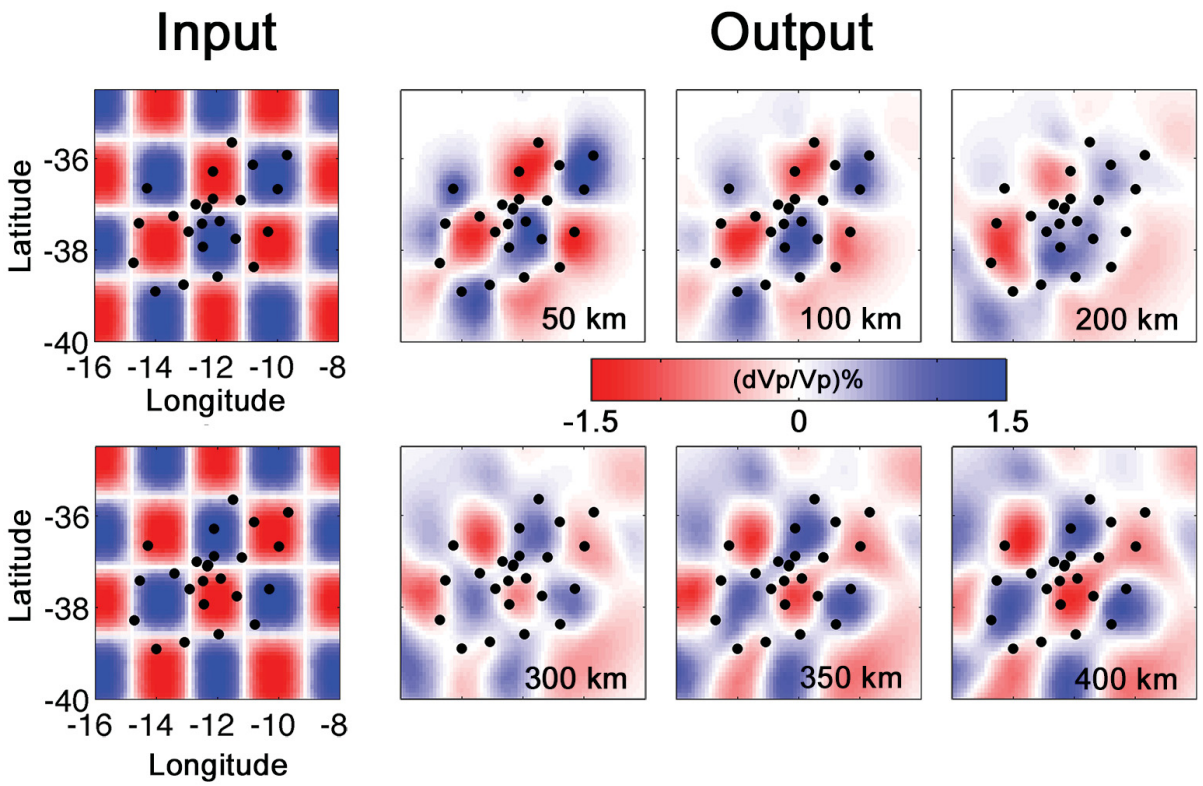

Figure 38: Checkerboard pattern for different depth slices. Amplitude of input pattern changes at a depth of 250 km. Left pictures: Input models. Right pictures: Recovered output models.

velocity model $\vec{m}_i$ with horizontally alternating amplitudes and a vertical change in anomaly polarity at 250 km depth. Thereafter we added a Gaussian-distributed random noise of 15% to the achieved synthetic residuals. With these residuals we minimized $|\mathbf{G}\vec{m}_o - \vec{d}_i|$ to get an output velocity model $\vec{m}_o$, which we compared to the input model $\vec{m}_i$. This gives us an idea which areas in our model are sensitive to a change in amplitude and showed us, which resolution can be achieved with the ray sensitivity coverage in $\mathbf{G}$. Fig. 38 shows the input models $\vec{m}_i$ and the achieved output models $\vec{m}_o$ for different depth slices (Fig. S46 shows the corresponding vertical cross sections): Good resolution is achieved in the central and western parts of the network. The depth slices at 200 and 300 km are resolved with weaker amplitudes than the others due to the change in anomaly polarity at 250 km. There are no rays in the north of the network above 200 km. However, at greater depths we can resolve the northeastern area. The eastern region is weakly resolved while the anomaly edges in the southeastern region, where the ray density is very low, are completely smoothed (Fig. 37 and Fig. 44). Within the network, the edges of the anomalies are clearly resolved, while they are smeared outside the network and especially in southeast-northwest direction. We have fewer rays arriving from the southeast to cross rays arriving from the southwest and so sharpen the alternating anomalies. The checkerboard patterns thus confirms the statements achieved from the hit quality and ray density pictures (Fig. 37 and Fig. 44).

In addition to the checkerboard tests (Fig. 46), we performed synthetic tests to investigate vertical resolution with our dataset. We created a model with 'floating', 'suspended' and 'rooted' anomalies to do this. Fig. 39 shows the results of these tests as vertical cross sections: Anomalies that are not connected to the bottom of the model are resolved as smaller than in the input models. Rooted anomalies appear with greater basal horizontal extents and are smeared into the main ray arrival direction. The horizontal edges of the anomalies can be resolved, even if the edges are somewhat shifted vertically (<50 km).
In one specific synthetic test, we checked whether a downwards-bifurcating input anomaly is resolvable. Fig. 40 shows one cross section of this test, which shows an anomaly that splits into branches separated by at least 100 km is probably resolvable in the southwest area of our model.
After performing synthetic tests, we tested the robustness and stability of our dataset: At first we omitted the crustal correction (Fig. S45). This correction influences the results to a depth of 100 km. At greater depths, the results are similar to those achieved with a crustal correction. The OBS stations vary by less than 1000 m in elevation. Therefore, while the crustal correction acts like an offset subtracted from the travel time residuals (Fig. 35b), this offset doesn't change the relative travel times. The island stations account for 19% of the data set and only the large elevation difference between them and the OBS stations has an influence on the residuals. These influences are remarkable only at shallower depths (<100 km) due to a lower ray density there. Deeper down (>100 km) more rays cross the voxels, therefore the results are based on more independent information received from travel times from different backazimuths. If we only apply an elevation dependent correction with a constant crust velocity of $5.8\frac{km}{s}$ and/or omit the 2 km thick crustal root, no changes are observed.
In a further test, we randomly select a half or a quarter of the travel time residual data set to show that the results are not dependent on a selection of events. In addition, we omitted some earthquakes, especially PKPdf arrivals from epicentral distances of $90° - 130°$ to assess the influence of these phases. We weighted down the residuals of South American earthquakes in order to balance the input data. Additionally, we changed the background velocity model. After performing several of these tests, we concluded, that the model's main features are consistent with the data and are mostly independent of the parametrisation.

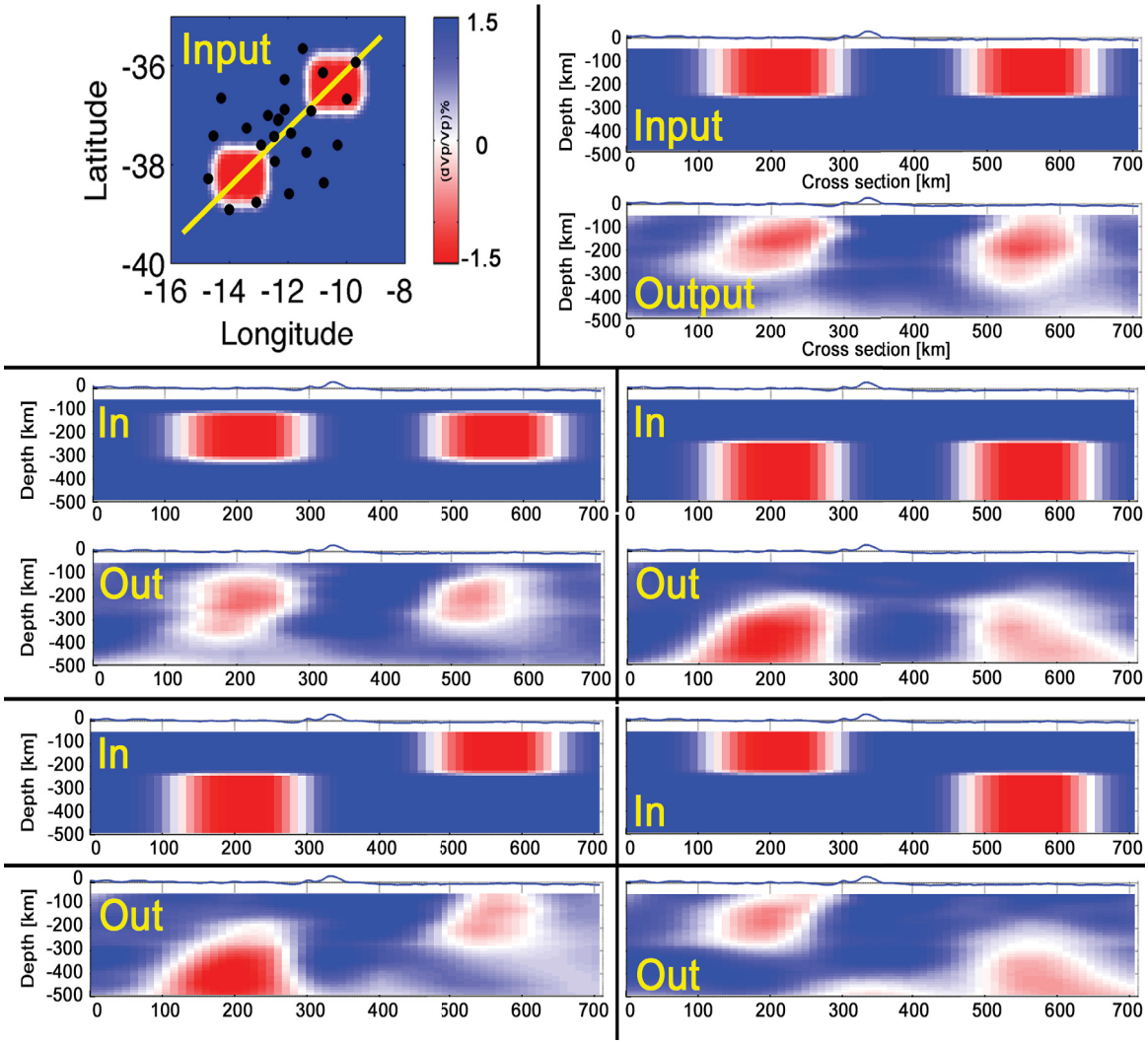

Figure 39: Synthetic tests with two anomalies distributed at various depth combinations in the model area. The cross sections running along the yellow line are shown for the input models and corresponding output models.

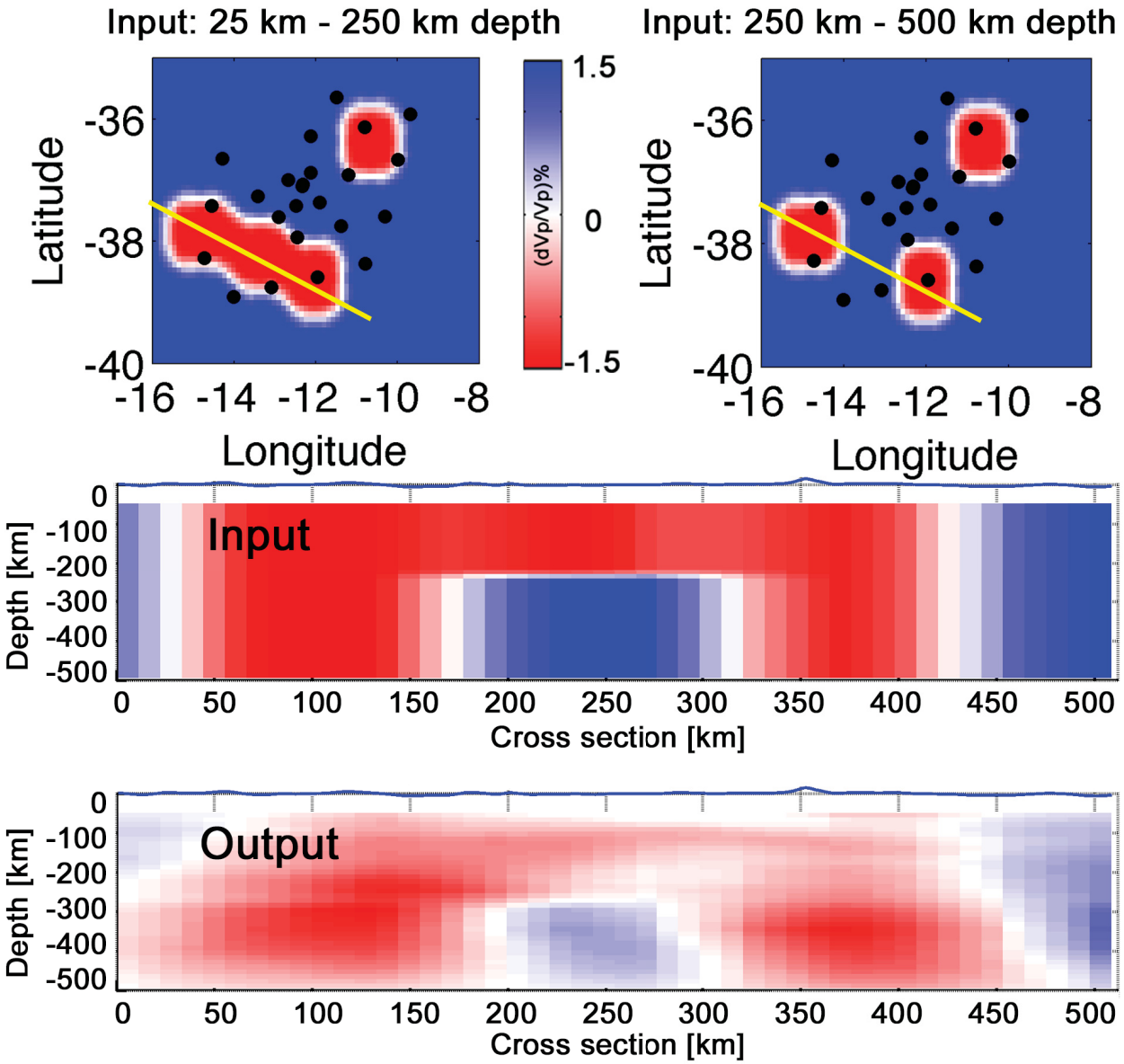

Figure 40: Synthetic test with an input anomaly that bifurcates downwards. The top figures show the input structure at 25-250 km (left) and below 250 km (right). The yellow line marks the location of the corresponding cross section, which is shown at the bottom of this picture. The upper cross section shows the input pattern, the lower section the output pattern.

6.6 Results

The results of the tomographic inversion show velocity perturbations in percent for different depths slices (Fig. 41). Starting at depths of 50 km near the base of the lithosphere, we observe

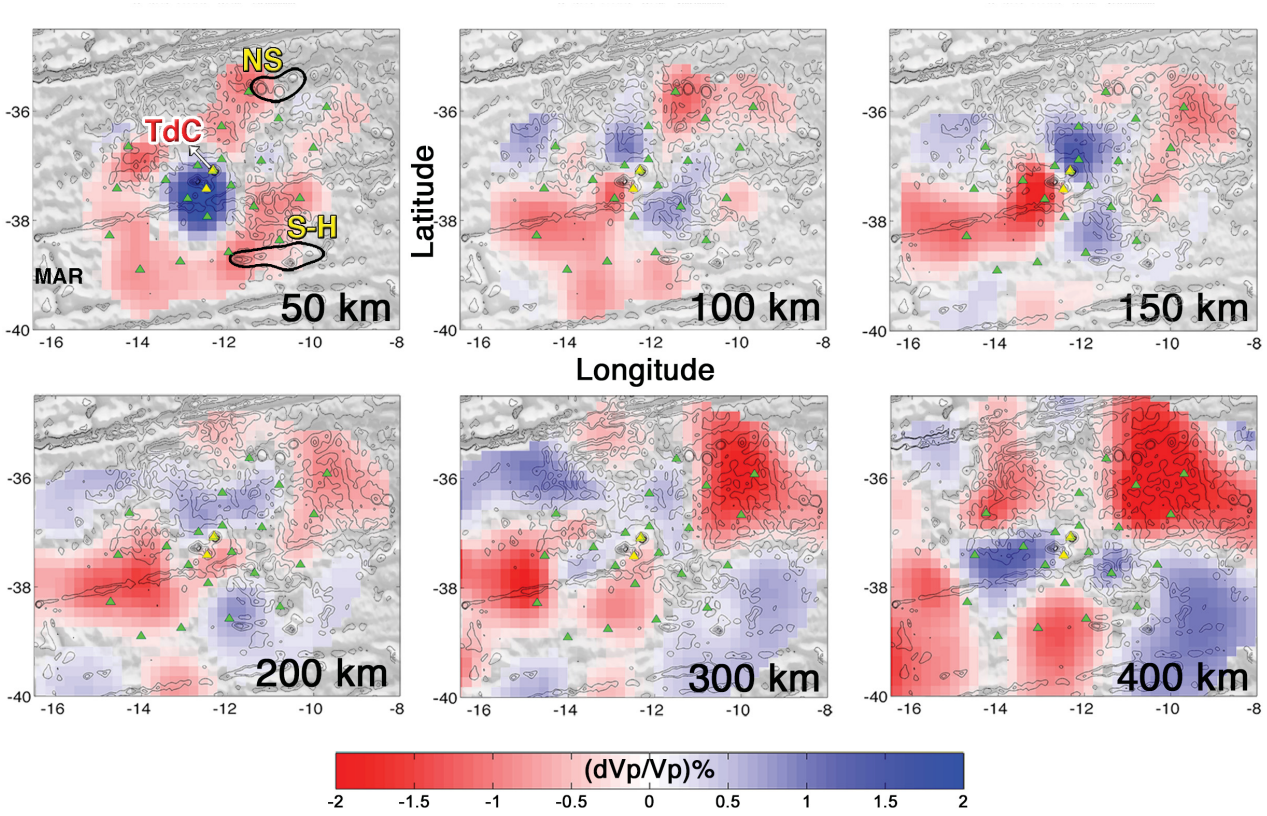

Figure 41: Horizontal P wave velocity perturbations in different depth slices. The colour scale saturates at -2% for low velocities (red) and +2% for high velocities (blue). Areas with no ray hits are masked (Fig. 37). The black lines are bathymetric contours. OBS stations are marked with green triangles and land stations (TdC and Nightingale) are marked with yellow triangles. The northern seamounts (NS) and the Speedwell-Hercules seamount chain (S-H) are marked in 50 km depth.

a striking circular higher velocity zone directly beneath the Tristan archipelago with a radius of $\sim$ 75 km, in which the magnitude of the V_p anomaly deviates from the surrounding by +1.5% to +2%. This anomaly spatially coincides with a bathymetric low, that surrounds the archipelago (Fig. 42a). The bathymetric low is disturbed by the Tristan da Cunha fracture zone, which cuts off the southern part of the structure. Further away from the island, this distinct high velocity anomaly is surrounded by lower relative velocities.
Another prominent feature is a lower velocity structure (-2% to -0.7%) southwest of TdC, which can be observed at depths greater than 100 km. This structure is spatially consistent throughout all following depth slices. Deeper in the mantle ($\sim$ 300 km) this volume of lower relative velocities spreads out to the south, where it extends to greater depths. This southwestern anomaly is located in a well-resolved part of the model space.
Another low velocity structure appears northeast of TdC at the edge of our network. Down to

a depth of 200 km, the amplitude of this low velocity zone is $\sim -0.7\%$ and, at greater depth, up to -2%. Only part of the low velocity zone is resolvable beneath the seismometer network, whilst those parts outside it suffer from poor resolution due to sparse ray path coverage (Fig. 37).
We observe a zone of higher velocities (+0.7% to +1.5%) at 150 km depth, which is located mainly east of TdC, but extends from north-northwest to southwest (Fig. 41). This structure coincides with a bathymetric low stretching from north of the Speedwell-Hercules seamount chain to the north of TdC.
Fig. 42b represents our results in 3D, by plotting the low velocity anomaly volumes within the -0.6 % perturbation surface. The southwestern low velocity structure connects the shallow upper mantle and the uppermost mantle transition zone in 500 km depth. It reaches its greatest horizontal extent (radius: $\sim$ 100 km) in a depth of 100 km to 200 km, and below 250 km it ramifies into narrower veins, each with a radius of approximately 50 km.

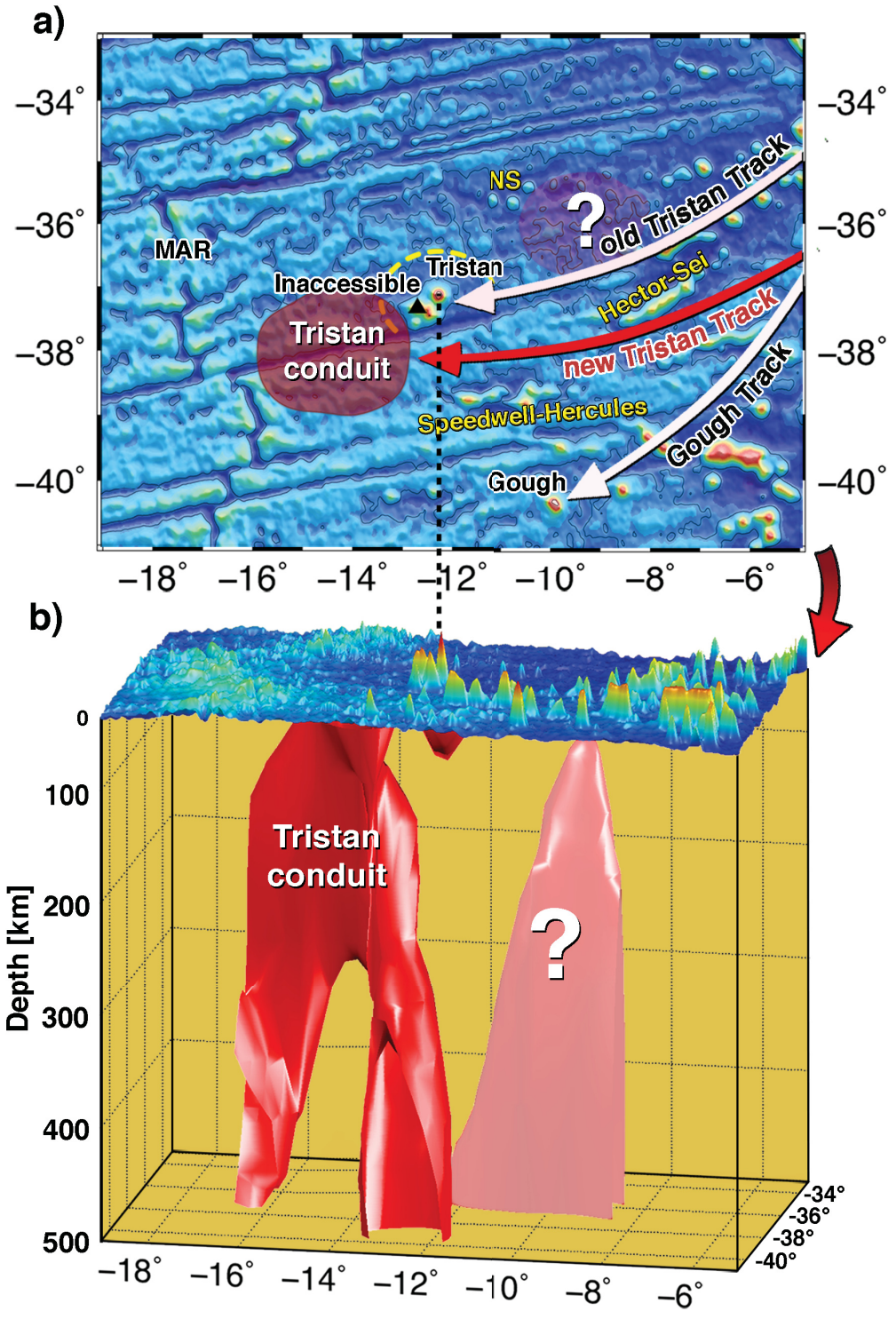

Figure 42: a) Map view of the investigated area with main interpreted features. Previously assumed hotspot tracks (white) are marked for comparison with the newlyproposed Tristan track (red), based on our results. The shapes of distinct lower velocity anomalies imaged at 200 km depth (Fig. 41) are marked. The black triangle marks Inacessible Island, the location of the theoretical calculated hotspot position. The dashed yellow line marks the bathymetric low surrounding the island. b) 3D imaging of low velocity zones contained with the -0.6 $(\frac{dVp}{Vp})\%$ envelope.

6.7 Discussion

6.7.1 Origin of Tristan da Cunha

We found a structure of relatively lower seismic velocities southwest of the archipelago of TdC, which extends from lithospheric depths to the bottom of our model (Fig. 41 and Fig. 42b). From 75 km to a depth of 250 km the structure has a radius of $\sim$ 100 km and we measure a velocity reduction of up to 2% compared to its surroundings.
These variations in seismic velocities may indicate differences in temperature and pressure (Karato, 1993), partial melt (Spetzler and Anderson, 1968), composition (Lee, 2003), water content (Karato and Jung, 1998), grain size (Faul and Jackson, 2005) or a combination of these physical properties. If we assume that compositional variations only play a minor role, the velocity perturbation of 1.5%-2% can be translated into a maximum temperature contrast of 300-400 K (e.g Nataf and VanDecar, 1993; Granet et al., 1995). In our opinion, the observed prominent lower velocity structure therefore reflects a combination of hotter temperature and the presence of partial melt.
From 75 km to a depth of 250 km, the $\sim$ 100 km radius of the cylindrical low velocity structure falls within the range determined for other prominent plumes or conduits (Hawaii 300 km; Afar and Reunion 200 km; Eifel 60 km (Montelli et al., 2004; Ritter et al., 2001)). By analogy, therefore, we refer to it as Tristan conduit. We interpret the lower velocity conduit as a narrow plume tail causing the magmatism at Tristan da Cunha and the nearby seamounts.

6.7.2 Interaction between the Tristan conduit and the lithosphere

The island of TdC was formed 1.3 ± 0.2 Ma ago (O'Connor and le Roex, 1992) and migrated northeast away from the MAR with the African Plate with at a velocity of $3.2\frac{cm}{yr}$ (Argus et al., 2011). If we assume that TdC was located directly above the Tristan conduit at its initial formation time, we would expect to find this source today 45 km southwest of TdC (Inaccessible Island, marked in Fig. 42a). We imaged the edge of the Tristan conduit below Inaccessible Island at a depth of 75 km to 150 km. At greater depth the Tristan conduit tilts towards the southwest away from the islands. We assume that plume material and heat was captured by the moving lithospheric plate beneath TdC and is causing the ongoing volcanic activity there. Future plume-related volcanism should be expected towards the west/southwest of the archipelago. A lower velocity zone at depths of 50 km to 100 km, which extends from the Tristan conduit to the young Speedwell-Hercules seamount chain located southeast of TdC may indicate a channelling of plume material from the conduit towards the seamounts (Fig. 41 and Fig. 42). Furthermore, we also observe a linkage at 50 km to 150 km depth between the low velocity structure at the northeast edge of our network and the northern seamounts (NS) (Fig. 41). These links can be interpreted as indications for recently existing feeder channels, which branched off from the Tristan conduit or the northeast structure and directed towards nearby seamounts chains. These chains, as well as TdC itself, are located along or close to fracture zones (Fig. 42a), which supports the idea that melt is transported from the Tristan conduit through weaker zones to the surface (O'Connor et al., 2012). However, it could also be the case that existing topography at the base of the lithosphere across the fracture zones control the melting within the uprising plume material.
We observe a circular higher velocity anomaly (+1.5%-+2%.) at 50 km depth directly beneath the TdC archipelago (Fig. 41). Seismic velocities in upper mantle rocks are significantly

influenced by the presence of water (Karato and Jung, 1998; Gaherty et al., 1999). We speculate that extensive remelting of the young lower lithosphere caused by the hot mantle plume resulted in further local depletion and dehydration (e.g. Villagómez et al., 2007; Phipps Morgan et al., 1995)). Alternatively, plume material of highly depleted composition might have accreted to the lower lithosphere by intrusion and underplating.

6.7.3 Depth extent

Below 250 km, the Tristan conduit ramifies into narrower veins (Fig. 42b). Subject to the resolution of our tomography, the apparent narrowing could be an effect of a reduced partial melt volume with greater depths. An alternative interpretation could be that the Tristan conduit is currently detaching from its deep source, as it has been proposed for the Azores plume (Silveira et al., 2006). In this interpretation, the Tristan conduit, decoupled from its source, is dying, which can be seen as consistent with the diminishing volcanism in the investigated area. Courtillot et al. (2003) already proposed a failing Tristan plume.
It is likely that, at present, the western side of the Tristan conduit interacts with the MAR because of their proximity. On the basis of trace-element and isotopic anomalies found in MORB at the MAR in this region (Humphris et al., 1985), Gibson et al. (2005) proposed that lateral flow of Tristan plume material towards the MAR is probable.
Masalu's (2015) S-wave velocity tomography showed that regional ridge-axis melt at the investigated latitudes could have a particularly deep source extent (down to 250 km) compared to other ridges. One reason might be that the Tristan conduit constitutes an additional deep source of melt. Zhang and Tanimoto (1993) identified an extended S-wave low velocity zone beneath the MAR, which is shifted off-axis towards Tristan and to a depth of 150 km. The Tristan conduit in our tomographic model (Fig. 41) coincides with this anomaly at these depths.
LLSVPs are generally considered to be the generation zones for mantle plumes (Burke et al.,2008;Torsvik et al., 2010). Some authors (e.g. Torsvik et al., 2006) propose that the African LLSVP in the lower mantle, the edge of which borders the investigated area, is related in some way to the Tristan conduit.

6.7.4 Splitting of subtracks

Enriched and less-enriched source components were determined in rock samples from Gough and TdC (Rohde et al., 2013a; Hoernle et al., 2015), on which basis the hotspot track has been subdivided into Tristan and Gough subtracks, each directed towards its respectively islands (Fig. 42a) (e.g. Rohde et al., 2013b). Based on the results of our tomography, we place the Tristan track now 100 km further south (Fig. 42a). The newly-proposed Tristan track-position coincides with the location of the Sei-Hector seamount chain at 37.3° S and the Hercules-Speedwell seamount chain at 38.7° S (Fig. 42a). Since the Tristan and Gough tracks are consequently located in close proximity, it becomes debatable whether we should maintain the spatial splitting of the Tristan and Gough subtracks or accept only one with various links from the Tristan conduit to the surface. Gassmöller et al. (2016) provides an indication for the latter by reconstructing crustal thickness along the Walvis Ridge - Tristan/Gough hotspot track for an assumed plume location between TdC and Gough Island. The authors suggested that the apparent separation into the Tristan and Gough subtracks can be explained by one single plume and interacting with the MAR. Results of $^{40}Ar/^{39}Ar$ step-heating experiments on

rock samples collected from other islands within the archipelago show that magma was being supplied simultaneously to Tristan and Gough over recent geological time (Schnur in prep.).
To explain the different compositions of rock samples found in this area, we assume that sharp and narrow morphological boundaries within the upper mantle are the only explanation for the differential compositions of Tristan da Cunha and Gough rocks. The upwelling material is highly influenced by and mixed with the heterogeneous ambient upper mantle material.
However, the potential existence of a second narrow conduit located northeast of TdC points to a more complex and heterogeneous mantle than expected so far. It may be possible that the upper mantle at the southwest end of the Walvis Ridge - Tristan/Gough hotspot track is penetrated by multiple narrow conduits, perhaps originating at the LLSVP as suggested by O'Connor et al. (2012). Those authors also suggested a mechanism of periodic suppression of plume melt transport to the surface. This would explain the absent or rather weak magmatism at the surface above the northeast conduit. Our results show that these conduits have radiuses of approximately 100 km.

6.8 Conclusion

We performed a finite-frequency tomography with relative travel time residuals from teleseismic earthquakes to resolve the upper mantle structure beneath the island of Tristan da Cunha (TdC). The results offer evidence for the existence of the Tristan conduit, which is located southwest of the TdC archipelago. With a radius of 100 km down to a depth of 250 km its shape is comparable to other prominent mantle plumes or conduits. Below 250 km depth, we observe a splitting into narrow veins, which may indicate a dying conduit or decreased melt fraction at those depths. Therefore our findings support the mantle plume hypothesis for the origin of Tristan da Cunha and the Walvis Ridge. Recent connections from the conduit to a seamount chain show, that melt is channelled towards seamounts and islands within the investigated area.
Strong heterogeneities and the existence of vein-like structures in the upper mantle could be the reason for the differences in rock composition found in this area. The close proximity to the mid-ocean ridge implies an interaction of the MAR and the Tristan conduit as was previously suggested by geochemical studies.

6.9 Acknowledgements

We thank the DFG (Deutsche Forschungsgemeinschaft) and "Senatskomission für Ozeanographie" for funding SAMPLE (South Atlantic Margin Processes and Links with onshore Evolution) Priority Program 1375 (JE296/9-1, GE 1783/4-2). Also we thank the master Ralf Schmidt and the crew of Maria S. Merian. We thank the DEPAS (Deutsche Geräte-Pool für amphibische Seismologie) instrument pool and the BGR (Bundesanstalt für Geowissenschaften und Rohstoffe) to provide us data from the IMS's 11 of the CTBTO. The authors thank M. Youssof for his support.

6.10 Supplementary

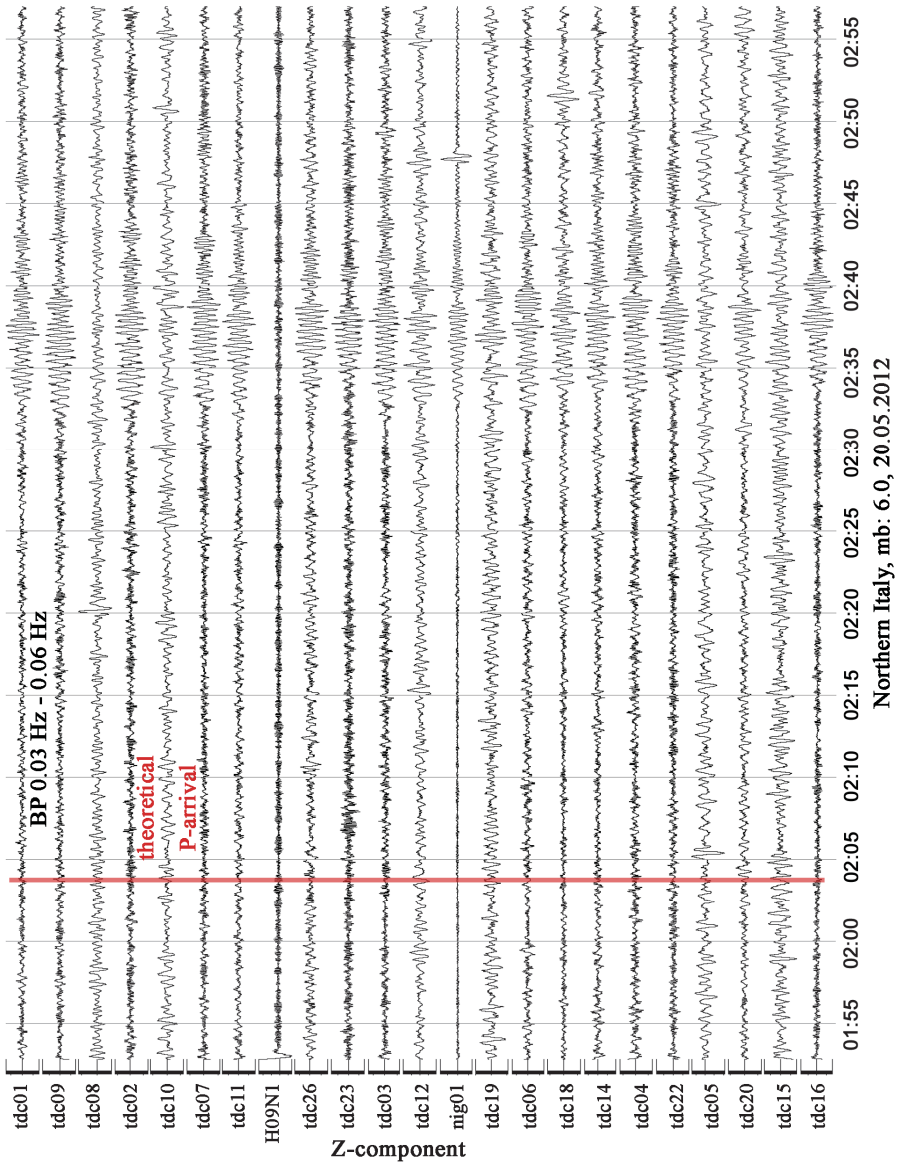

Figure 43: Seismograms of a northern Italy earthquake (20.05.2012) with magnitude (mb) 6.0 (lat: 44.89, lon: 11.23). The theoretical P arrivals are aligned to the event time (02:03:52). The traces are filtered with a bandpass filter from 0.03 Hz to 0.06 Hz. Only the surface waves can be observed.

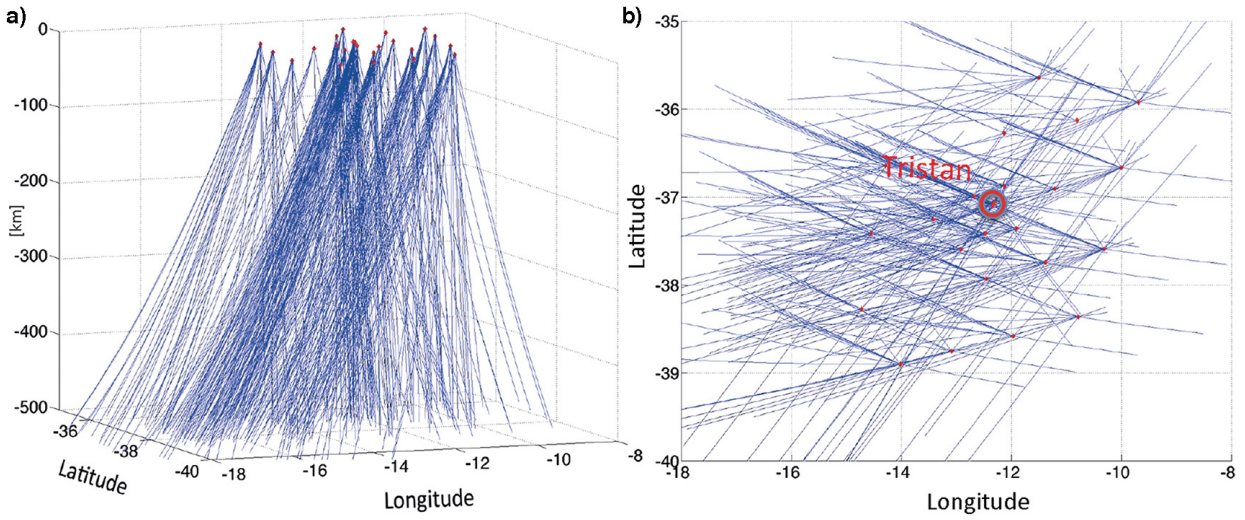

Figure 44: All used source-receiver ray paths within the model space. a) 3D ray density, b) Plan view ray density. The location of TdC is marked with a red circle.

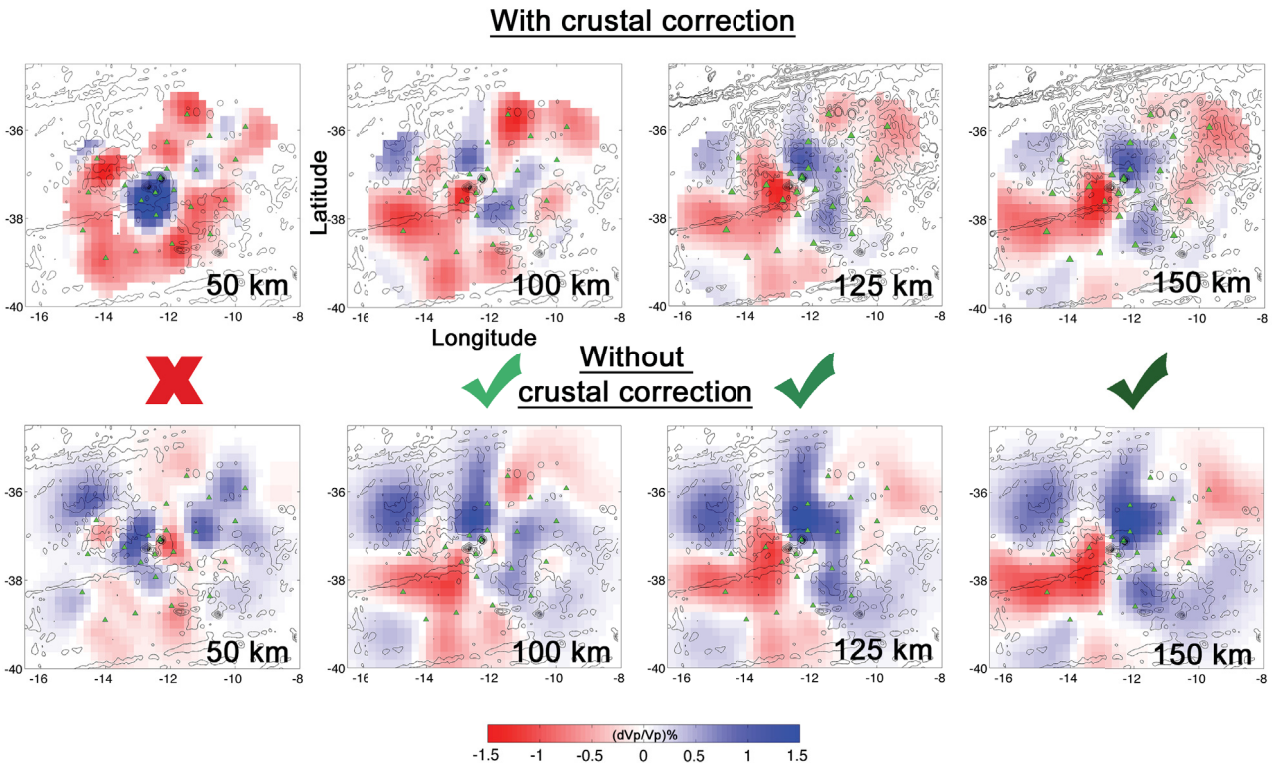

Figure 45: Comparison between the tomographic results with and without a crustal correction for depth slices from 50 km to 150 km.

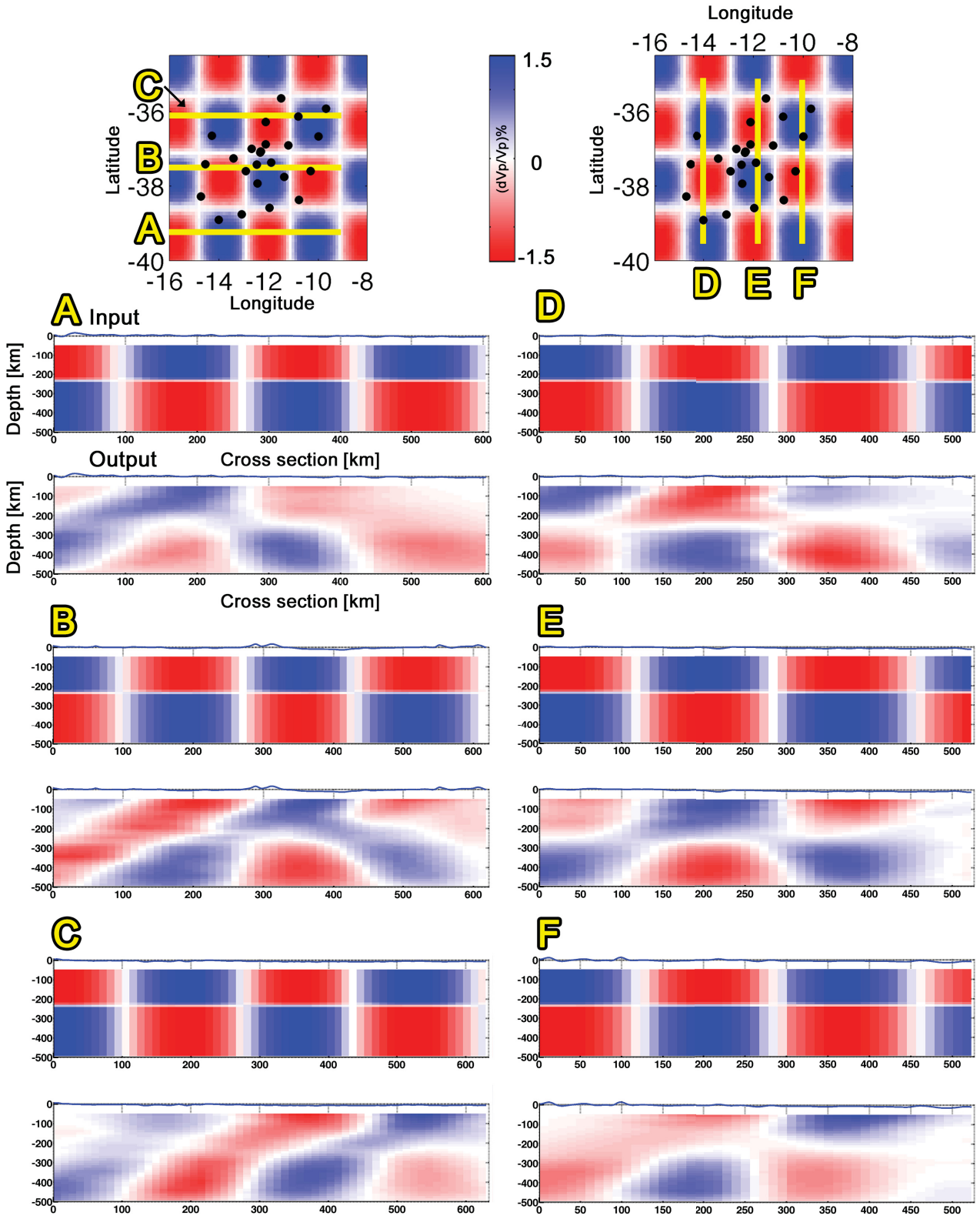

Figure 46: Vertical cross sections through the checkerboard pattern. Yellow lines mark the locations of the cross sections. The first cross section below a capital letter shows the input model while the second cross section shows the corresponding output model.

7 Seismicity in the vicinity of the Tristan da Cunha hotspot - Interaction of plate tectonics and mantle plume presence

7.1 Abstract

Seismicity along the southern Mid-Atlantic Ridge can be mostly confined by earthquakes with magnitudes larger than 4 listed in the global network earthquake catalogue. These localisations have large uncertainties due to the sparse distribution of permanent seismological stations in and around the South Atlantic Ocean. Normally, most of the earthquakes are located close to the ridge axis or in immediate vicinity of transform faults and therefore indicate plate tectonic processes related to the formation of new oceanic lithosphere. Local or regional networks to investigate these processes in detail are sparse or missing in the South Atlantic. The reason for that are the great distances to the next continent and therefore high expeditions costs as well as unfavourable weather conditions prevailing in the South Atlantic Ocean.
Here, we present a unique dataset acquired by ocean-bottom seismometers and land stations located around and at the archipelago of Tristan da Cunha. These island are situated in the vicinity of the Tristan mantle plume and the Mid-Atlantic Ridge.
One year of monitoring allows the detection of otherwise unobserved intra-plate seismicity in the African oceanic plate segment north of the island, which we relate partly to stresses induced by the bordering transform fault. An apparently aseismic zone coincide with the proposed location of the Tristan mantle plume southwest of the islands. This indicates elevated temperatures within the lithosphere above the mantle plume and potentially weakening by uprising fluids. Intra-plate seismicity might also be related to stresses induced by the presence of the plume and hint for an incipient ridge jump in the near future. Furthermore, we locate seismicity close to the islands of Tristan da Cunha and nearby seamounts, which we relate to ongoing tectono-magmatic activities in this area.

7.2 Introduction

Tristan da Cunha (TdC) is a small volcanic island in the South Atlantic Ocean and belongs to the eponymous archipelago (Fig. 47). Besides the inhabited main island TdC itself, the archipelago comprises the uninhabited Nightingale Islands, the Wildlife reserve Inaccessible Island and a number of smaller islands.
TdC is situated at the southwestern end of the Walvis Ridge - Tristan/Gough hotspot track, 450 km east of the present day spreading axis of the Mid-Atlantic Ridge (MAR). Currently, different hypothesis exists to explain the geodynamic of the island: The origin of TdC is either attributed to shallow plate tectonics (e.g. Anderson and Schramm, 2005) or to the existence of a mantle plume (e.g. Morgan, 1971; Courtillot et al., 2003). It has long been accepted that a plume directly beneath the island formed the archipelago (O'Connor and Duncan, 1990; Rohde et al., 2013b). Schlömer et al. (in rev.) located as one of the first a low-velocity structure southwest of TdC and attributed it to a weak Tristan mantle plume. This study also proposed guiding of hot material at the base of the lithosphere from the plume towards the islands and nearby seamounts. Moreover, the authors assumed an interaction with the nearby MAR.

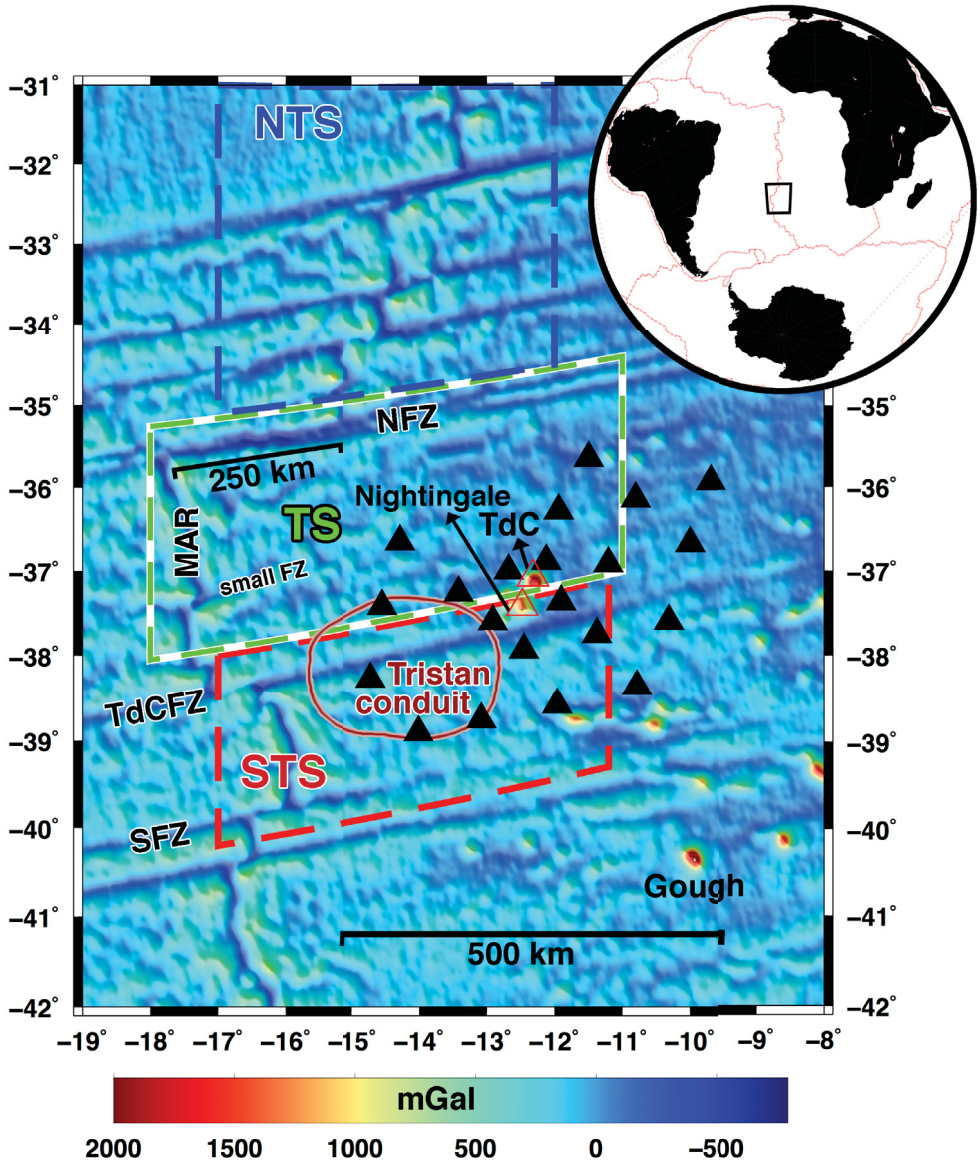

Figure 47: Satellite gravity map (Sandwell et al., 2014) of the study area, including locations of OBS (black triangles) and land stations (Nightingale and TdC: red framed triangles). Abbreviations: NTS - Northern Tristan Segment; TS - Tristan Segment; STS - Southern Tristan Segment; NFZ - Northern Fracture Zone; MAR - Mid-Atlantic Ridge; TdCFZ - Tristan da Cunha Fracture Zone; SFZ - Southern Fracture Zone; small FZ - small Fracture Zone. Red circular frame: location of the Tristan conduit found by P-wave tomography (after Schlömer et al. in rev.), green frame: NTS including part of MAR, green frame: TS with NFZ and part of MAR, red frame: STS including TdCFZ and part of MAR. Overview map with the main plate borders and the black marked study area is shown in the top right corner.)

The slow-spreading MAR in this region is strongly segmented along its axis by transform faults and associated fracture zones. Directly south of the archipelago the Tristan da Cunha Fracture Zone (TdCFZ) is situated. An offset of 250 km between the along-axis ridge can be observed at a large transform fault north of the island (Fig. 47). This offset is among the largest in the South Atlantic Ocean. Briais and Rabinowicz (2002) proposed that the eastern flank of the MAR in the study area spreads $\sim 20\%$ more slowly than the western flank.
Because of the remote location of the study area, very little is known about the local and regional seismicity. Additionally, the seismological station density is very low in and around the South Atlantic. Therefore, the existing knowledge based on global network observations of events with magnitudes larger than 4 (NEIC - National Earthquake Information Centre). These localisations suffer from large error ellipses due to the large distances to the recording stations.
Nevertheless, a few studies examined the seismicity at the archipelago or in its vicinity: Baker et al. (1962) reported on the most recent onshore eruption, which occurred in 1961 close to the capital settlement of TdC. This eruption was accompanied by seismic activity.
Earthquakes were felt again by the Tristaniens in 2004. Though fresh pumice was found on the beaches, the vent of the eruption remains unknown(Hards, 2004). Earthquakes of the 2004 seismic sequence were located close to Nightingale Island with two hydroacoustic stations O'Mongain et al. (2007). The authors associated them to submarine activity. Haxel and Dziak (2005) detected seismicity along the older part of the Walvis Ridge northeast of our study area and explained the occurrence of earthquakes by the recurrence of magmatic activity there. But these detections also suffer from larger location uncertainties.
Here, we present a study of local earthquakes using a temporary network of ocean-bottom seismometers (OBS) and island stations. Our results give new insights into oceanic intra-plate seismicity, the role of mid-ocean ridges and transform faults, mantle plumes and their potential interaction, as well as tectono-magmatic processes.

7.3 Data

We deployed a network consisting of 24 OBS and two seismological land stations around the island of TdC and on Nightingale Island during the R/V Maria S. Merian cruise MSM 20/2 in January 2012. The network covered an area of 400 km times 500 km with the archipelago of TdC in its centre (Fig. 47). The average station spacing was approximately 85 km and the western boundary of the array was located 120 km away from the MAR. All land stations and OBS were equipped with a three-component seismometer, the OBS systems included also a hydrophone. The instruments recorded continuously seismological data for one year with 50 Hz or 100 Hz sampling frequency and were recovered during the cruise MSM 24 in January 2013.
We extended our dataset by data of the IRIS (Incorporated Research Institutions for Seismology) seismometer station TRIS and by two hydroacoustic stations H09N1 and H09W1, operated by the CTBTO (Comprehensive Nuclear-Test-Ban Treaty). All three stations are located on the island of TdC. Unfortunately, the permanent seismometer TRIS was flooded in early 2012 and we could only use a small amount of data at the beginning of our experiment.
TdC is located in the middle of the South Atlantic, in a region of strong year-round westerly winds. This results in a high noise level at frequencies around 1 Hz measured in the OBS data and in a high noise level at frequencies larger than 3 Hz registered with land stations. The high noise level observed at land station data at frequencies, in which local earthquakes

normally occur, is caused due to high wind speeds and surf arriving at the coasts of the islands. Therefore, less than 1% of the picked arrival times were obtained from land stations. Figure 48 shows an example of a local earthquake detected on the vertical components in close proximity to Nightingale Island within the network. The waveforms are sorted with increasing distances from receivers to the earthquake. The signal-to noise ratio (SNR) is much higher in seismograms of the land stations (H09N1, H09W1 and nig01) compared to seismograms of OBS due to the above-mentioned reasons.

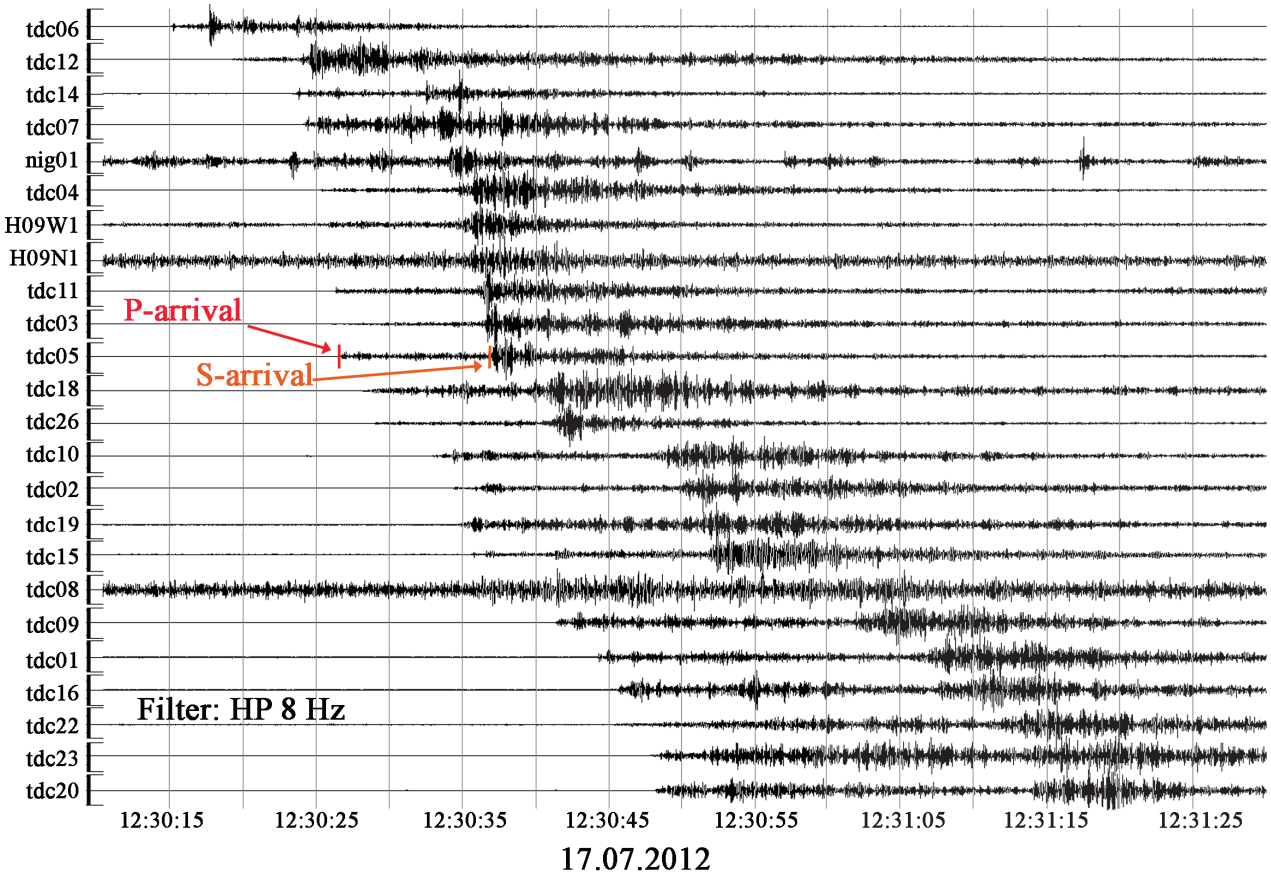

Figure 48: Example of a local earthquake occurred within the network close to the archipelago of TdC (37.69°S, 11.50°W). The vertical components filtered with a high-pass 8 Hz are shown. Event time: 17.07.2012 12:30:11.

7.3.1 Method

In a first step, we considered clock drifts (skews) of the OBS recorders and applied linear time corrections. We also corrected the timing of the seismograms for a leap second, which occurred in 2012. Afterwards, we applied a short time average/long time average (STA/LTA) detection algorithm to the continuous dataset. Because the algorithm was optimized to detect local earthquakes, the data were high-pass filtered (HP: 8 Hz) prior to the application. We observed acoustic waves in the filtered seismograms, emitted by marine mammals. The algorithm also detected these signals. Therefore, the detections served only to find potential local earthquakes in the continuous dataset, because afterwards the P- and sometimes additionally S-wave arrivals

were subsequently hand-picked. We used the hydrophone and vertical components to identify the P-arrivals and the horizontal components to identify the S-arrivals. 30% of the identified earthquakes were not used for this work, because the seismograms were too noisy to identify a first arrival, nor were these events locatable.

7.3.2 Localisation

We used the algorithm *dbgenloc* (Pavlis et al, 2004) implemented in the BRTT (Boulder Real Time Technologies) Antelope software and arrivals of at least 5 stations to localise earthquakes. The software uses an one-dimensional velocity-depth model to calculate travel times. In absence of information concerning the velocity structure within the crust beneath TdC, we assumed a velocity model with Moho depth of 11 km, a two-layered oceanic crust for the land stations and a homogeneous crust with an overlaying 800 m thick sediment layer for the OBS stations. The crustal P- and S-wave velocities were derived from a seismic refraction velocity model of the Discovery seamount (42°S, 0°10.02' E) (Keßling, 2008). Although the seamount is located 1500 km away from TdC, it provides the only direct information on crustal velocities in this region. The used velocity-depth model is listed in table 2. The model contains no water column but the localisation routine considers negative depths for the OBS, which are located in depths between 3.1 km and 4.1 km (Tab. S1).

Only a small number of events occurred within the network and showed clear P- and S-arrivals

Depth [km]	P velocity [km/s]	S velocity [km/s]	Layer
0	4.8	2.7	1. Layer
4.2	2	1	Sediment
5	5.4	3.7	2. Layer
11	7.9	4.5	Mantle

Table 2: P- and S-wave velocity model for the Tristan region.

and were hence suitable to determine also the hypocentre depths. We were not able to identify any first motion polarities.

The localisation routine weighted individual observations by the inverse of the picking errors. We assume a uniform error of 0.5 s. At the end of the localisation process, earthquakes with a root mean squared (RMS) travel time residual larger than one second were eliminated. A maximum measure of the epicentral error is determined by the length of the major and minor axis of the horizontal components of the confidence ellipse. The depth error for the hypocentre locations is estimated with the maximum value for the four principal axes of the confidence ellipsoid projected in vertical direction. 67% of the localized earthquakes have major axis lengths $\leq$10 km and the remaining events have major axis lengths $\leq$30 km. Finally, we obtained 473 events from 4574 P-arrivals and 598 S-arrivals within one year of monitoring.

7.3.3 Magnitude

We calculated the local magnitudes (ML) for all localised events. Firstly, the data were filtered with a Wood-Anderson Velocity (WAV) filter whereby the gain of the instrument response was considered to ensure the reliable conversion from velocity to displacement measurements.

Afterwards we measured the maximum amplitude of the earthquake on the vertical component. The local magnitude for an event measured at one station was calculated by

$$M_L = \log_{10}(A_{max}) + B(d), \tag{28}$$

in which A_{max} is the maximum amplitude and B(d) is a Richter correction value as function of the distance between source and receiver. If the signal-to-noise ratio fell below a given threshold the measurement was eliminated. Abnormal magnitudes and outliers were also recognized and excluded. In a further step, we calculated the median value of all station magnitudes for each event. This value is not strongly affected by large outliers. The minimum local magnitude measured with the network was 2.0 and the maximum magnitude was 5.3 with a distance of 64 km and 367 km to TdC, respectively.

7.4 Results

7.4.1 Spatial distribution of earthquakes

The spatial distribution of local events in the TdC region and their calculated magnitudes (ML) are shown in Fig. 49. As shown in Figure 47, we divide our study area according the plate segments into the Southern Tristan Segment (STS), the Tristan Segment (TS) and the Northern Tristan Segment (NTS). The latter consists actually of several smaller plate segments separated by fracture zones. The discussed fracture zones are a fracture zone in the south (SFZ), the Tristan da Cunha Fracture Zone (TdCFZ), and a Northern Fracture Zone (NFZ) (Fig. 47).

Southern Tristan Segment: In the south, we detected a few single earthquakes along the MAR and several at the SFZ and TdCFZ. Earthquakes occurred at the TdCFZ west of 14°W with local magnitudes ranging between 3 and 4 and from 12.5°W to 11.5°W (Fig. 49) with magnitudes 2 to 3. Interestingly there is significant seismicity (events with local magnitudes of 2.5 to 3.5) in a band spanning from the TdCFZ towards the SFZ from 15°W to 13 W. In an area slightly southwest of the archipelago we do not locate any event (marked in Fig. 49)

Tristan Segment: Within the central Tristan Segment (TS), again only single events were located along the MAR. Surprisingly, significant intra-plate seismicity dominates here. Earthquakes occurred between 16°W and 13°W approximately 120 km to 380 km east of the active spreading MAR and plate boundary. The local magnitudes are in the range of 3 to 4. The magnitudes increase to 4.8 starting from Tristan in north/northwest direction towards the northern fracture zone (NFZ), which borders this segment. The NFZ is characterized by many earthquakes with relatively large magnitudes (>4).

Northern Tristan Segment: The region north of the NFZ (from 36°S to 34°S) shows a high level of seismicity, mainly close to the MAR axis and along the transform faults and fracture zones. Further north, we locate most of the earthquakes along transform faults and only a few earthquakes were located intra-plate east of the MAR. Earthquakes far in the north were detected only with magnitudes larger than 4, since smaller events could not be detected by our network.

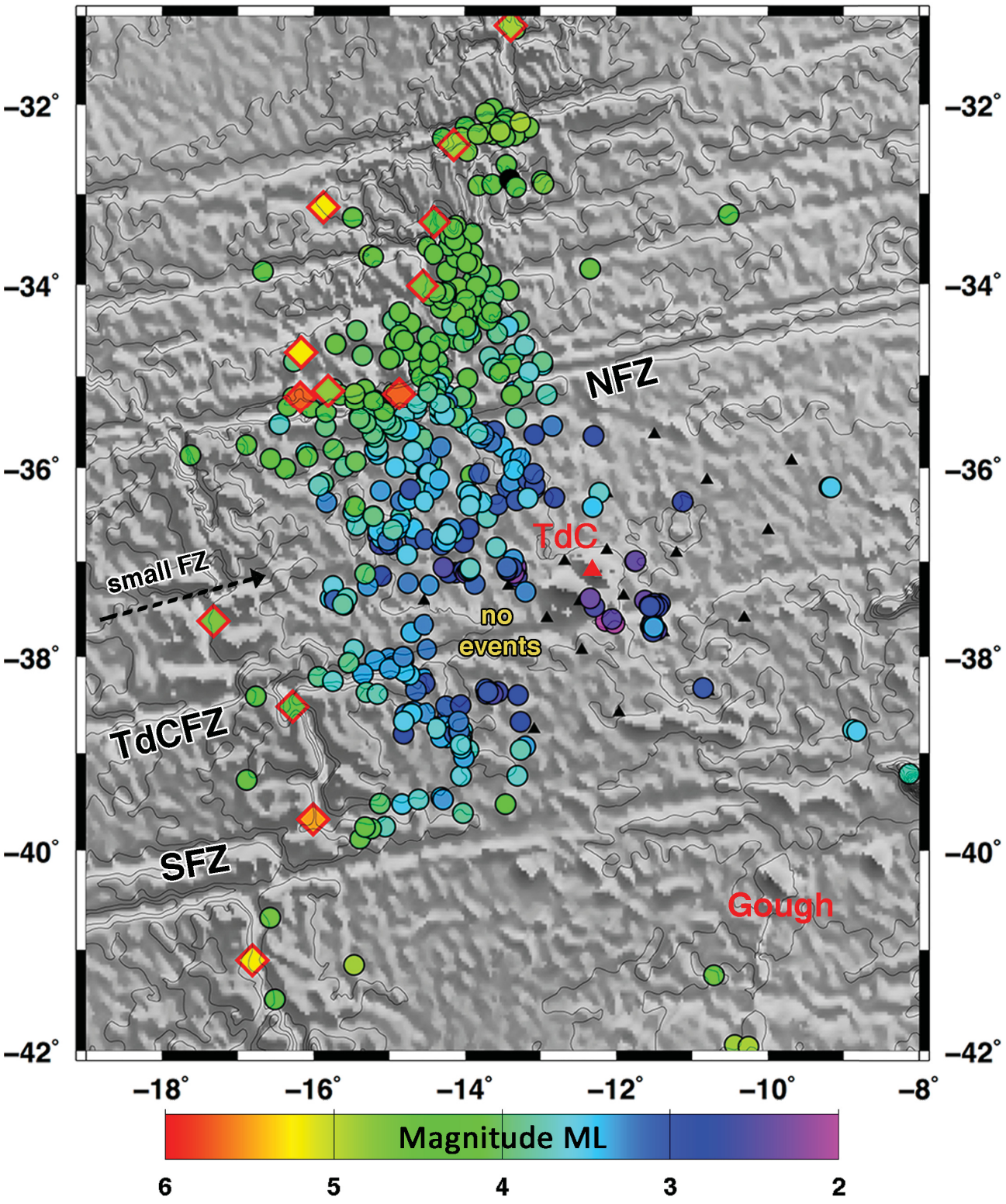

Figure 49: Local earthquakes in 2012. The circles mark the localisations obtained by the network detections, while the diamonds mark the events, which are also listed in the NEIC catalogue. The colour indicates the local magnitudes or rather the body-wave magnitudes for the NEIC events.

Earthquakes close to the archipelago of TdC: Beside the earthquakes along the MAR axis, transform faults and fracture zones, we also observed a few earthquakes in close proximity to the islands and seamounts. Some of these events occur close to the TdCFZ but further east of the main active zone of this fracture zone. For a detailed view, we plotted these events in a separate figure (Fig. 50a). The error ellipses of these earthquakes are smaller than the plotted location dots in the map. It is particular apparent, that the events in this area are restricted in distinct clusters: One of these clusters is positioned northwest of Inaccessible Island. More than 10 earthquakes were detected in immediate vicinity to 37°S and 13.4°W (Fig. 50a, labelled with c1). The magnitudes range between 2.2 and 3.3.
Two other earthquake clusters (c2 and c3) can be observed between 13°W and 11°W close to the TdCFZ (Fig. 50). One (c2) is located directly southeast of Nightingale Island (12.8°W to 12°W, ML: 2-3). Another cluster (c3) is positioned further to the east at the TdCFZ (11.5°W). In these cluster the earthquakes are concentrated at 37.7°S and 11.5°W. Because of the location of these earthquakes within the network and clearly P- and S-wave arrivals, we were able to determine hypocenters depths (Fig. 50b). The depths range mostly between 20 km and 30 km (depth errors $\leq$3 km). For a comparison with long-term observations, we also added the NEIC position of an earthquake occurred in 2013 to the map. Additionally, we plotted the earthquake (NEIC), which occurred on the 29.07.2014 northeast of Nightingale Island with magnitude 4.8. Probably as a consequence of this large earthquake O'Mongain et al. (2007) localised a swarm of earthquakes at the same day, which are also shown in the figure.

Comparison with teleseismic events: For a comparison of our observations with long-term seismicity in the study area, we plotted the available NEIC earthquake locations and their related body-wave magnitudes (mb) for a time period from May 1969 to August 2016 in figure 51a. The locations within the catalogue have large error ellipses due to the sparse amount of permanent installed stations in that area (IRIS operates the STS-2 on TdC only since 2004).
Because of missing first motion polarities, we used the Harvard CMT (Centroid Moment Tensor) catalogue to get an insight into the focal mechanism of the earthquakes. These solutions are plotted in figure 51b.
The catalogue event localisations primary dominate the along-axis ridge segments. However, a few deviations from the axis become visible and coincides with our earthquake localisations of 2012: Five earthquakes occurred along a band parallel to the ridge within the STS starting at the TdCFZ at 14.8°W and running southwards to the SFZ (Fig. 51a, red dashed line). These earthquake locations coincide with the region of high seismicity within the STS in our local observations (See 7.4.1 and Fig. 49). One earthquake occurred at the TdCFZ at 11°W and can be assigned to cluster c3 (See 7.4.1 and Fig. 50a). Only one event (2004), which occurred in immediate vicinity to the islands is listed in the NEIC catalogue throughout the time and marked in figure 51a.
Though the NEIC catalogue earthquakes mostly occurred at the NFZ a few events are shifted northwards and southwards (Fig. 51a, yellow dashed line) of this fracture zone and become intra-plate earthquakes, comparable to our observations. Less than eight events occurred at the MAR at latitudes between 37°S and 36°S (Fig. 51a, purple dashed line). Our results show also lack of seismicity within this MAR segment. Coincidence is also reached at the ridge segment between 34°S to 33°, where no seismicity is observed (Fig. 51a, orange dashed line).

West of this MAR ridge segment the NEIC localisation show some intra-plate earthquakes placed on a line from northwest (17°W) to southeast (15°W). Two focal mechanism solutions are available for these events and we localised 2 earthquakes in the same region in 2012.
While intra-plate earthquakes appeared east of this ridge segment at 33°S to 32°S, the NEIC catalogue included only a few earthquakes within this segment. Earthquakes located at the MAR in the STS have magnitudes smaller than 5.5.

7.4.2 Temporal distribution of earthquakes

To recognize temporal relationships between the earthquake occurrences in 2012, we plotted the number of local earthquakes for each day in 2012 (Fig. 52c). It is noticeable that only a few earthquakes could be evaluated between June and August. During that time we observed many acoustic signals emitted by whales, which masked the arrivals of the P-wave and hence these earthquakes were not suitable for a localisation.
It is conspicuous that an occurrence of more than 4 earthquakes can in most cases be assigned to one region and to one day. To demonstrate this, we selected days at which the number of events exceeds 6 or is noticeable concentrated to a specific region (Fig. 52). We also plotted the events per day for each region in figure 54 of the supplementary material. (For further observations of the temporal distribution, we added a gif-file to the enclosed storage system, which shows the occurrence of earthquakes in 2012 in a time-lapse.) Figure 52b shows not only active seismic days, but also a north-south shift within the earthquake occurrence with the passing of time (03.04.2012 and 18.05.2012).

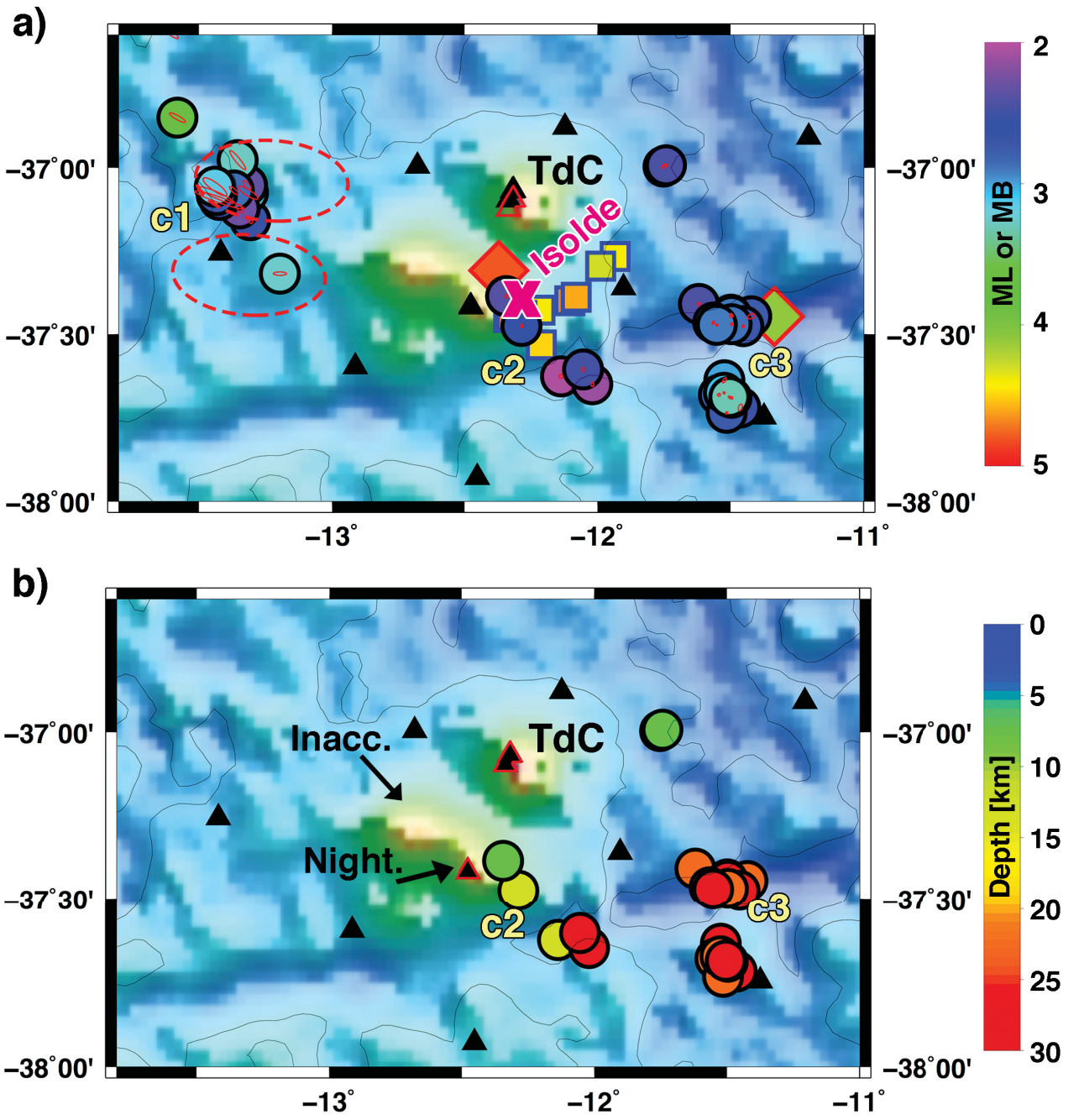

Figure 50: a) Magnitudes of earthquakes. Black framed circles: our observations in 2012; red framed diamond at TdCFZ: NEIC earthquakes (Event time: 2013), red framed diamond between Nightingale and TdC: NEIC earthquake (Event time 29.07.2004), blue framed squares: Swarm locations after (O'Mongain et al., 2007) (Event times: 29.-30.07.2004), red dashed frames: volcanic fields (after Geissler et al., in prep.), magenta cross: location of new found seamount Isolde (Geissler et al., in prep.). The colour indicates the moment magnitude for NEIC events and the local magnitude for others. The NEIC, swarm and c1 earthquakes have fixed depth. b) Our hypocentre locations in 2012 with red error ellipses in 2 different clusters (c2 and c3). The colour indicates the hypocentre depth. Abbreviations: TdC - Tristan da Cunha; Night. - Nightingale Islands; Inacc. - Inaccessible Island.

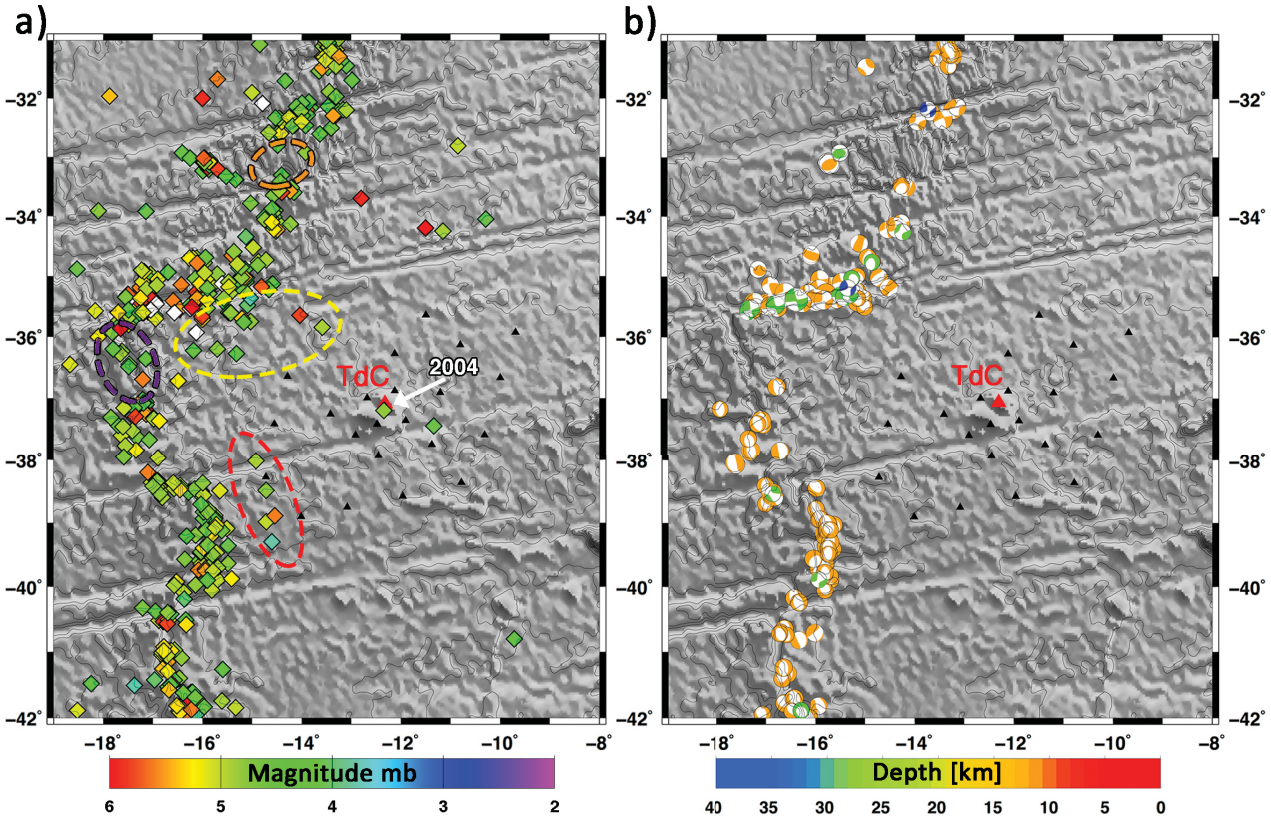

Figure 51: a) Locations of NEIC earthquakes from 1968 - 08.2016. The color indicates the body-wave magnitude mb. b) Focal mechanism solutions from the CMT Harvard. The color indicates the hypocenter depths.

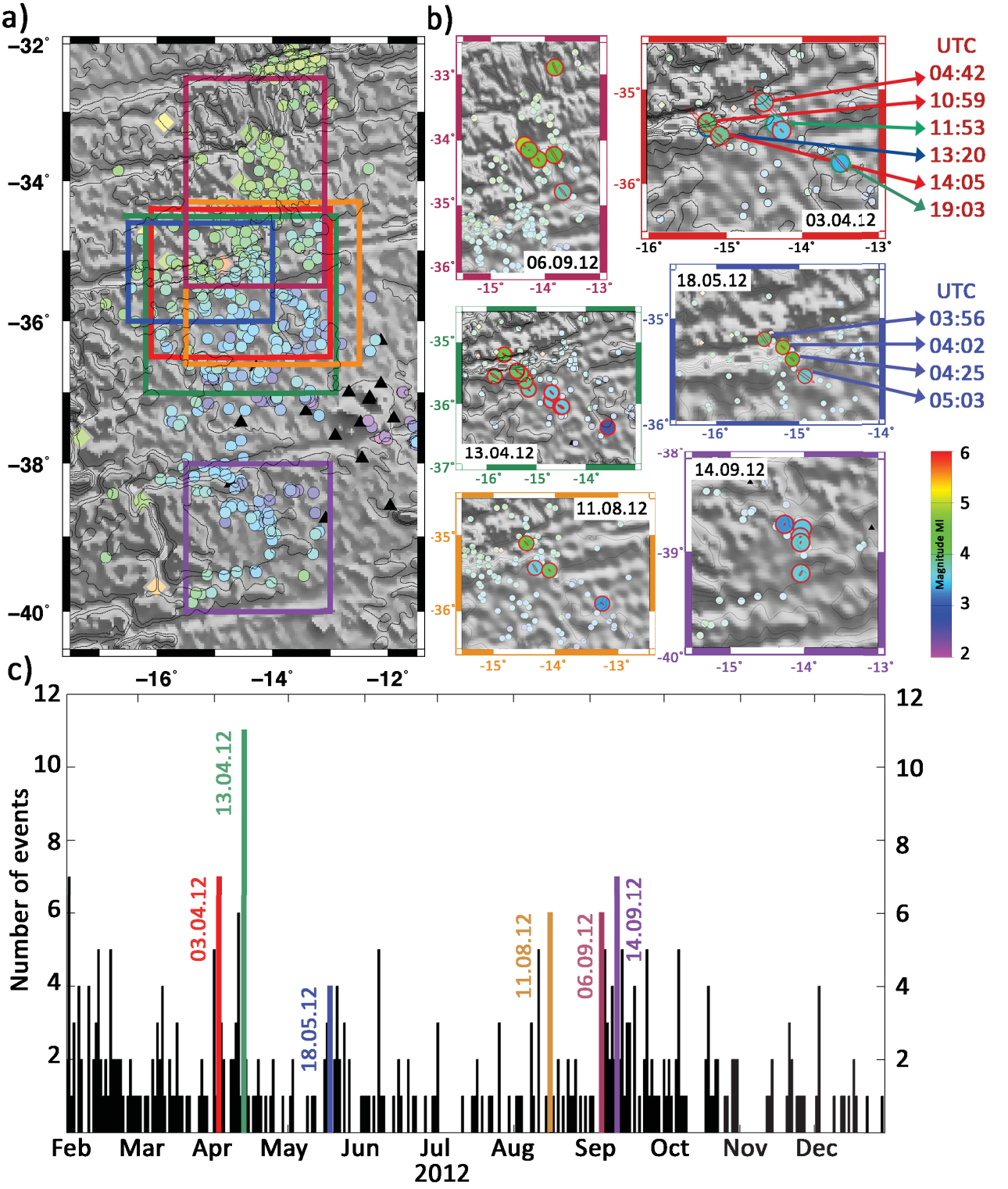

Figure 52: a) Map view with marked sections focused in b) b) Earthquakes at specific days with its error ellipses. At two days the earthquakes are labelled with their event time. c) Number of earthquakes per day. The specific days focused in b) are colour indicated.

7.5 Discussion

We observe different locations of seismicity in the Tristan region and attribute the occurrence of earthquakes in these specific regions to different physical processes.

7.5.1 Intra-plate seismicity due to plate tectonics

A high occurrence of intra-plate earthquakes is apparent in the TS, which we attribute to stresses within the segment. Along the NFZ, a distance of 250 km (Fig. 47) between the southern part and the northern part of the MAR crest is measured (Fig. 47). The relative movement of the plate segments on either side of the ridge crest is sinistral (Fig. 53a). The directions of motion along the NFZ can also be derived from the strike-slip type of events of the Harvard CMT catalogue (Fig. 51b), where one nodal plane coincides with the sinistral transform motion.
The segments are hooked together at their borders and the movement in opposite directions causes tensions or rather stretching forces within the TS (Fig. 53b). The continuing of the northern MAR crest to the south (red dashed line in (Fig. 53b)) can be used as an imaginary distinction within the TS, where the forces change their direction (Fig. 53b). The stretching forces are larger west of this imaginary distinction due to opposite acting forces at the northern border of this particular segment. East of this line both bordering plate segments are moving into the same direction and thus the tensions decrease. The strength of these forces are indicated by vectors in figure 53b. The described stress field is reflected by the occurrence of earthquakes within the TS: A large number of events occurred west of the imaginary distinction, while a smaller number of events is located east of this line (Fig. 49).
Furthermore, we can also identify the propagation of the stress field by the temporal observations of events at two specific days. The first earthquake on a specific day occurred at the fracture zone (Fig. 52b, red and blue maps): Accumulated stress was released by a strike slip movement (Fig. 51b) and pulls at the northwestern boundary of the TS. This drag causes tension forces, which propagates southwards through the TS (Fig. 52b). Later in that day, we observe intra-plate earthquakes. The direction of propagation starts at the NFZ and follows a line into the plate (green dashed envelope of the vectors in figure 51b). This line implicates the decrease of horizontal stretching forces with increasing distances from the NFZ.
The local magnitudes of these intra-plate earthquakes range between 2.5 and 4, while earthquakes at the fracture zone have magnitudes larger than 3.8. This is shown in figure 49 and in figure 52c in short sections including the NFZ (red-03.04.12; green-13.04.12, blue-18.05.12 and green-13.04.12). Consequently, it is possible to differentiate between fracture zone earthquakes, where strike slip movement occurs and intra-plate events caused by tension forces. To summarize, the temporal and spatial distribution of earthquakes at the NFZ and within the TS reflects the prevailing stress field within the TS (Fig. 53b).
Intra-plate seismicity is also apparent in a small segment between 33°S and 32°S (Fig. 49). The above-mentioned forces act at all similar plate geometries, but most of the ridge crest offsets (transform faults) have either smaller distances or can only be observed by local networks due to small magnitudes.

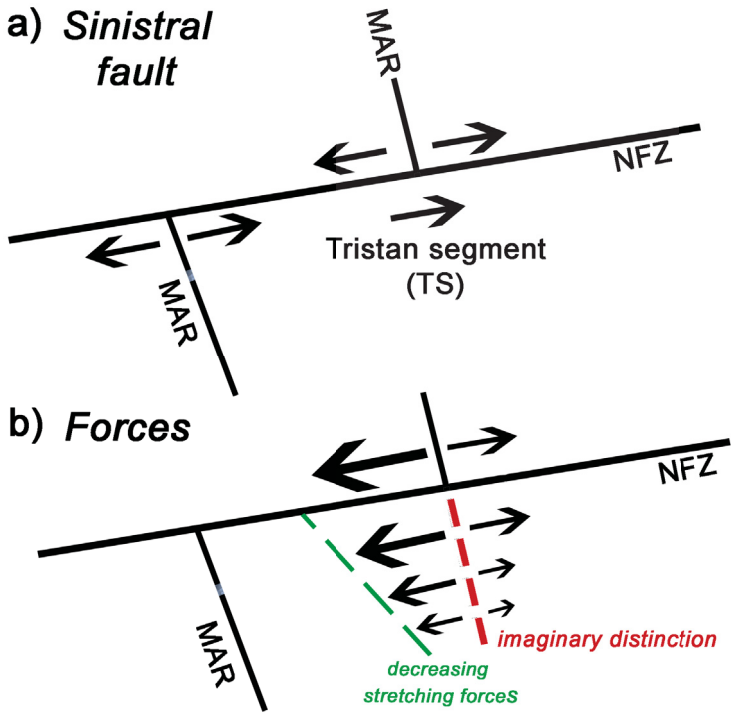

Figure 53: a) Directions of motion of the Tristan Segment (TS) and its bordering segments. b) The arrows indicate the strength of forces within the TS. The red dashed line is the imaginary continuing of the northern MAR ridge crest to the south. The green line indicates the decreasing stretching forces with increasing distance from the NFZ.

7.5.2 Regions of no seismicity along the MAR axis

We observe a lack of seismicity along-axis at the MAR crest at latitudes from 38°S to 36°S and from 33°S to 32.5°S in long-term observations (Fig. 51) as well as in 2012 (Fig. 49). The conformity of the dataset in these regions indicates a persistent lack of seismicity at time-scales of at least a few decades and excludes that the aseismic regions can be assigned to a variable temporal characteristic.
Different approaches to explain seismic lacks in other regions: Smith et al. (2003) proposed a correlation between the thermal structure and seismicity: high seismicity is assigned to thinner and hotter lithosphere, while low seismicity or lacks of seismicity are assigned to thicker and therefore colder Lithosphere. Wolfe et al. (1994) proposed that the different styles of seismicity in the MAR segments indicates that the thermal structure is not in a steady state, while Arnott et al., (1994) proposed that in this quiescent areas stress is accumulated but not being released. We additionally assume that the forces acting at the northern margin of the TS slow down or even stop this plate segment to move away from the ridge crests. Hence, the stretching forces at the ridge are minimized and as a result the number of earthquakes decreases. This assumption is supported by ∼20% slower spreading rates at the eastern flank of the MAR in the TdC region compared with the western flank (Briais and Rabinowicz, 2002). Furthermore, it seems that the TS adopts a passive role in these plate tectonic processes, while the bordering NS is in continual motion and adopts an active role.

7.5.3 Coincidence of plume location and seismicity lack

Southwest of TdC we observe a circular lack of seismicity with an east-west extension of ∼200 km and an north-south extension of ∼100 km (marked in fig. 49). Since earthquakes are generated by brittle failure of rocks, melt, its high viscosity and the related absence of frictional forces could cause lacks of seismicity. This distinctive zone with absent earthquakes coincides spatially perfectly to the location of the Tristan conduit imaged by a P-wave tomography based on teleseismic earthquakes (Schlömer et al. in rev.) (Fig. 47).
The lack is virtually surrounded by earthquakes (Fig. 49). Besides the presence of melt, a tomography images also hot temperatures, while earthquakes indicate failures of rocks. Therefore, the aseismic/seismic border may indicate the transition zone between ductile (reheated lithosphere) and brittle regime in the surrounding.

7.5.4 Ridge jump caused by Tristan conduit and plate tectonics

The high seismicity within the TS continues southwards away from the NFZ along the abovementioned band parallel to the MAR crest (see 7.4.1 and Fig. 53b). It is interrupted (Fig. 49) by the aseismic zone (plume location) and continuous southwards within the TS until it reaches the SFZ. The seismicity indicates the tensions, which prevails in the segments. These tensions weaken the lithosphere of the segment along the imaginary line. Additionally, the lithosphere is reheated by magma penetration, originated from the Tristan conduit and potentially thermally thinned by the underlying plume. These processes in addition with a passive role of the TS, meaning a slow motion and local stability of the segment may indicate successive ridge jumps of the involved sections towards the east. The proposed incipient ridge axis would run along this imaginary distinction within the TS and cross the Tristan conduit in its center. A few authors already predicted jumps of the MAR segment towards the Tristan da Cunha hotspot (e.g. Briais and Rabinowicz, 2002; Mittelstaedt et al., 2008).

7.5.5 Earthquakes close to the archipelago of TdC

Since 2 localisations of 2012 events coincide spatially with the swarm location of earthquakes in 2004 and 3 earthquakes occurred a little bit south at the TdCFZ (far east of the active TdCFZ) (Fig. 50a), we conclude a long-term activity in this region. This answers the question asked by O'Mongain et al. (2007), whether the swarm in July 2004, including the large NEIC earthquake with an abrupt onset can be considered as an isolated event or as regularly activity.
So far, there have only been speculations about the causes for this earthquake occurrence. Geissler et al. (in prep.) recently discovered a new submarine volcano named Isolde at the flanks of Nightingale Island during the cruise MSM 20/2. Its peak is situated only 200 m below the sea surface in a region, where seismic activity is observed (Fig. 50a, magenta cross). The authors proposed that the Isolde seamount might be the vent of the 2004 eruption. The occurrence of earthquakes 8 years later could indicate ongoing magmatic unrest in that area.
An additional earthquake cluster (c1) can be observed west/northwest of Inaccessible Island (Fig. 50b). This cluster coincides with proposed monogenetic volcanic fields found in bathymetry and sediment echosounder data (Geissler et al., in prep.) (Fig. 50a, marked with red dashed lines). The occurrence of earthquakes concentrated at a specific location points to further formations of seamounts and magmatic activity.

It can be summarized that the immediate vicinity to TdC is seismic active over a long time period.

7.6 Conclusions

High seismicity within a plate segment north of Tristan da Cunha is assigned to stresses due to different directed forces acting at the northern boundary of this plate. The spatial distribution and the magnitudes of these earthquakes give evidence for the prevailing stress field within the plate. The temporal occurrence of the events in addition to their magnitudes points to the occurrence of earthquakes at the transform fault caused by plate motions. The bordering plate segments are stretched and causes intra-plate earthquakes even in greater distances to the transform fault.
An area with no seismicity coincides spatially with the location of the Tristan conduit. This supports the existence of a heat source in the upper mantle beneath that area and reheating and weakening of the overlying lithosphere, which causes a ductile regime.
Furthermore, we find indications for an incipient ridge-jump 250 km towards the east to a parallel line, which crosses the centre of the Tristan conduit and spans along the band of high intra-plate seismicity.
Moreover, we locate earthquakes in close vicinity to the archipelago and nearby seamounts, which we interpret as ongoing tectono-magmatic activity.

7.7 Acknowledgements

We thank the DFG (Deutsche Forschungsgemeinschaft) and "Senatskomission für Ozeanographie" for funding SAMPLE (South Atlantic Margin Processes and Links with onshore Evolution) Priority Program 1375 (JE296/9-1, GE 1783/4-2). Also we thank the master Ralf Schmidt and the crew of Maria S. Merian. We thank the DEPAS (Deutsche Geräte-Pool für amphibische Seismologie) instrument pool and the BGR (Bundesanstalt für Geowissenschaften und Rohstoffe) to provide us data from the IMS's 11 of the CTBTO.

7.8 Supplementary

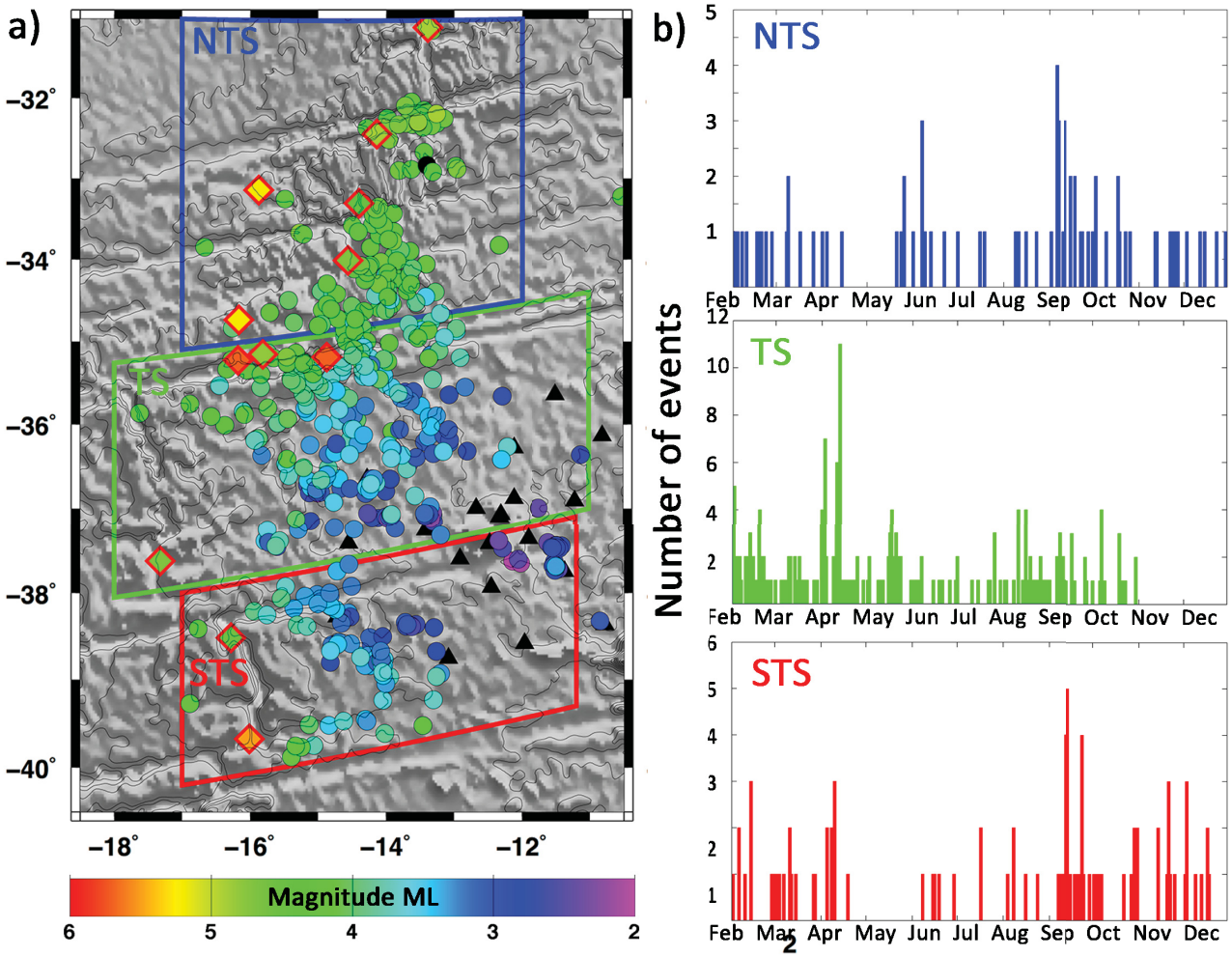

Figure 54: a) Map view with regions. b) Number of earthquakes per day for each region.

8 Merging electromagnetic & seismological data to reveal the upper mantle beneath the Tristan da Cunha hotspot

8.1 Abstract

Tristan da Cunha is a volcanic island in the South Atlantic close to the Mid-Atlantic Ridge. It is located at the western and youngest end of the Walvis Ridge - Tristan/Gough hotspot track. Tristan da Cunha together with the Walvis Ridge represent the classical example of a mantle plume track due to a link to the Cretaceous Etendeka flood basalt province in northwest Namibia. But the genesis of the island has so far remained enigmatic. It is hotly debated if Tristan da Cunha sits actually above a deep mantle plume or if it is only originated by upwelling material from weak (leaky) fracture zones.
A recent P-wave tomography imaged the Tristan conduit southwest of the island. Its shape is comparable to other prominent plumes. However, peculiarities compared to a classical hotspot track are present: The youngest end of the hotspot track is characterized by widely scattered seamounts and small islands and a diminishing volcanism can be observed in the region. These facts, however, tend to contradict a plume tail with a diameter of 100-200 km.
Here, we combine the recent results of marine magnetotelluric data with the tomographic results to reveal the upper mantle beneath Tristan da Cunha. We compare the results of the different methodologies and construct a model to explain the linkage between the island of Tristan da Cunha and the plume.

8.2 Introduction

Tristan da Cunha (TdC) is a small volcanic island in the South Atlantic Ocean. Besides the main island TdC, the eponymous archipelago comprises the Nightingale islands and a Wildlife Reserve Inaccessible Island. TdC is situated at the youngest end of the Walvis Ridge - Tristan/Gough hotspot track (Fig. 55). The present day spreading axis of the Mid-Atlantic Ridge (MAR) is 450 km west of TdC.
The origin of TdC has been controversy discussed. The reason for the complex debate is missing geophysical data in this region due to the remote location of the archipelago. While several authors proposed a deep-seated mantle plume beneath the TdC hotspot (Morgan, 1972; White and McKenzie, 1989; Courtillot et al., 2003), a few authors suggested an origin caused by shallow plate tectonics (Anderson, 2005; Foulger and Natland, 2003; Fairhead and Wilson, 2005).
Schlömer et al. (in rev.) recently imaged a Tristan conduit southwest of the island by performing a P-wave finite-frequency tomography. The shape of the plume is cylindrical with a diameter of 200 km down to a depth 250 km. Below that depth the conduit ramifies in narrow veins.
Thermal boundary layers like the mantle transition zone, the Large-Low-Shear Velocity Provinces (LLSVP) or the core mantle boundaries are zones to generate mantle plumes. Geissler et al. (in rev.) proposed a thinning of the mantle transition zone (410-660 km depth) south of the island. This may indicate also the presence of a mantle plume.
(Gassmöller et al., 2016) reconstructed crustal thickness along the Walvis Ridge - Tristan/-Gough hotspot track. The authors explained the volcanism in the study area by a plume interacting with the MAR. Based on geochemical data several authors proposed also an inter-

action with the MAR (e.g. Schilling et al., 1985; Gibson et al., 2005).
However, inconsistencies compared to a classical hotspot with an underlying mantle plume are noticed: The youngest end of the hotspot track including TdC consists of widely scattered islands and seamounts. A decline of volcanism is observed in the region. Only small volcanic cones have been mapped at the surface directly above the conduit (Geissler et al. in prep.). These inconsistencies tend to contradict a plume tail with a horizontal extend of 200 km. It has also to be clarified how plume melt reaches the island of TdC.
Here we combine the recent tomographic results of seismological data (Schlömer et al. in rev.) with recent results of electromagnetic conductivity (Baba et al. in rev.). The aim is to reveal the upper mantle beneath the Tristan da Cunha hotspot to understand upwelling processes, to explain how melt reaches the surface (TdC) and to explain the above-mentioned inconsistencies.

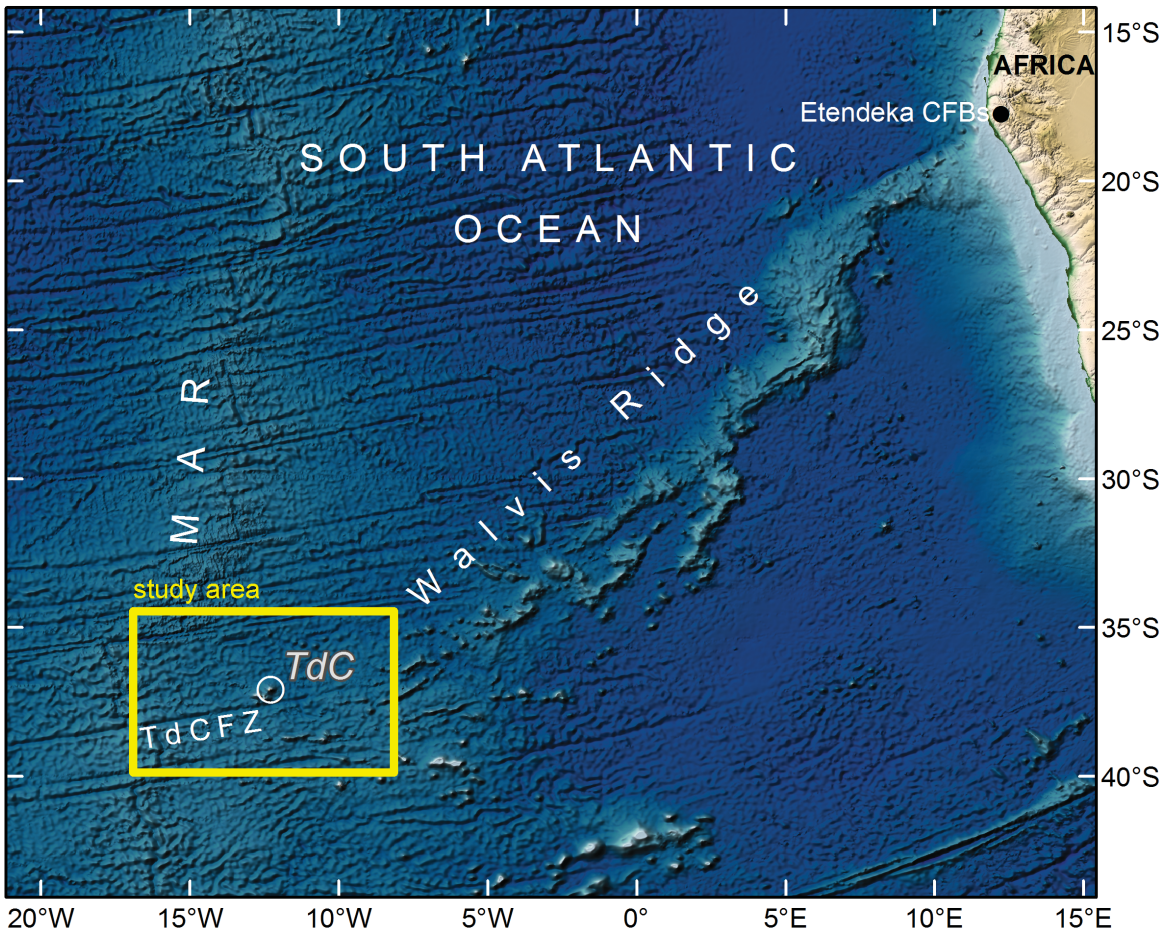

Figure 55: Bathymetric map of the study region including the Walvis Ridge - Tristan/Gough hotspot track. The study area is yellow framed and TdC is white circled. Abbreviations: MAR - Mid-Atlantic Ridge; TdC - Tristan da Cunha; CFBs - Continental Flood Basalts, TdCFZ - Tristan da Cunha Fracture Zone.

8.3 Syntheses of electromagnetic and tomographic results

The results of the conductivity and seismic tomography overlap at depths between 50 and 400 km. The highest resolution of the tomographic results is reached in a depth range of 100-300 km, while the EM has its best resolution above 150 km. The EM suffers also of low vertical resolution with increasing depth and would provide at best weak constraints on deeper structure (Kelbert et al., 2012). Therefore, we focus our interpretation of the combined results to depth above 250 km.

In a first step, we compare the conductivity of the magnetotelluric (MT) data (Baba et al. in rev.) with the tomographic results (Schlömer et al. in rev). Figure 56 shows the respectively depth slices from 150 km to 250 km in 50 km steps. While the tomographic results show a low velocity structure W/SW of the island throughout all depth slices, a conductive layer is observed north of the Tristan da Cunha Fracture Zone (TdCFZ) at 100 km and 150 km depth. A significantly resistive zone can be observed southwest of the archipelago in these depths. The TdC region, the west and southwest part of the study area are also resistive below 150 km depth.

Neither the conductivity nor velocity observations revealed indications for a plume-like structure directly beneath the archipelago of TdC. But the low velocity zone W/SW of the archipelago is attributed to the Tristan conduit (Schlömer et al. in rev.). The conductivity contrast across the TdCFZ indicates a higher potential temperature of the segment south of the TdC (Baba et al. in rev.). We assign the elevated temperature to the plume presence.

In Fig. 57, we merged a cross section of the conductivity along -38°W, an 1D electrical conductivity structure model and the 3D low velocity perturbations, which are measured to be lower than -0.6% dVp. The massive upper part of the cylindrical low velocity structure coincides with a broad conductive layer at depth of 100 km to 150 km imaged by the cross section of the conductivity and by the 1D conductivity structure model, which had a peak at this depth.

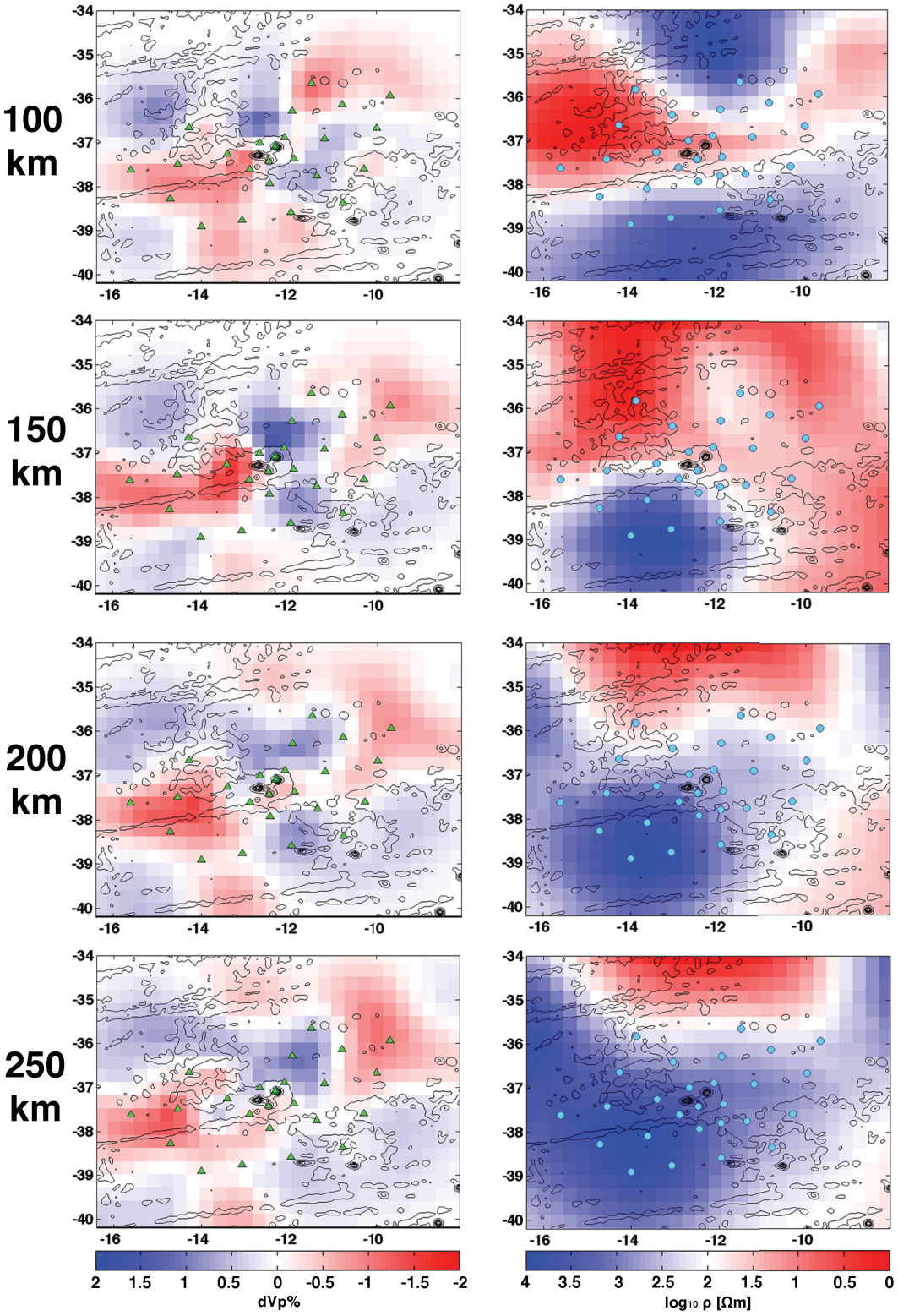

Figure 56: Comparison of seismic tomography (left) and electromagnetic conductivity (right) for different depth slices (100-250 km).

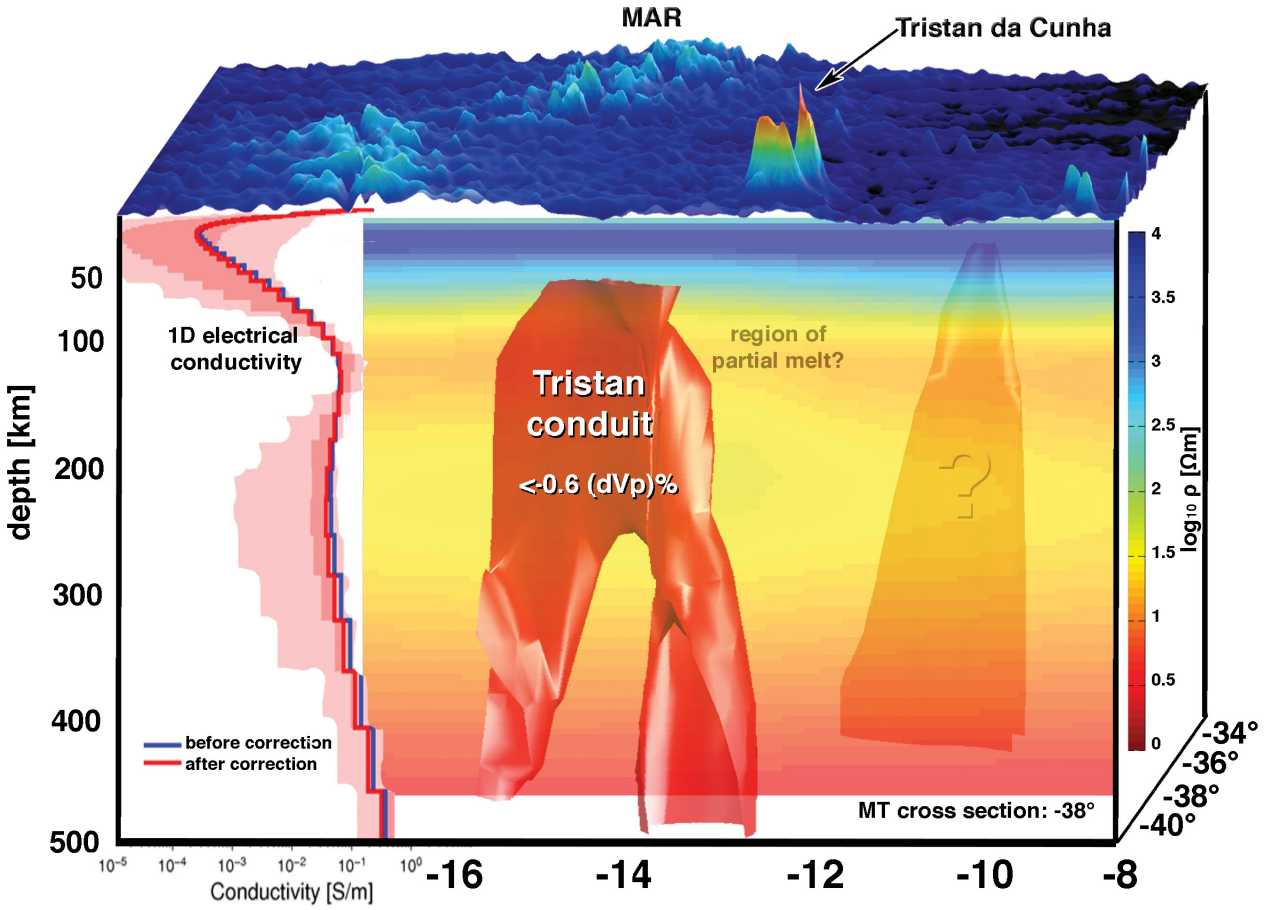

Figure 57: 3D tomographic results imaged by the envelope of the low velocities smaller than -0.6 dVp% (Schlömer et al. in rev.) combined with electromagnetic conductivity along a cross section at -38°and and 1D electrical conductivity model (left) (Baba et al. in rev.). t=The upper part of the low velocity structure coincides with the conductivity layer in 100-150 km depth.

8.4 Discussion

While low electrical resistivity anomalies are indicators for the presence of partial melt, low velocities indicate elevation of temperature and potentially also the presence of partial melt. Therefore, we assume that below a depth of 150 km the material of the Tristan plume is hotter than the surrounding mantle. The EM data show a broad, horizontally extended conductive layer above 150 km depth, which coincides with the upper part of the imaged conduit. As a consequence we assume the presence of partial melt in that layer.
It is surprising that although the size of the conduit is comparable to other prominent plumes (Schlömer et al. in rev.), a bathymetric feature like a volcanic island or a seamount directly above the Tristan plume is missing. Geissler et al. (in prep.) mapped only a few small volcanic cones at the surface close to the TdCFZ above the conduit. Therefore, we assume that the strength of the plume is not sufficient to penetrate the lithosphere vertically. A few authors already proposed a weak plume (e.g. Courtillot et al., 2003). This characteristic can be the reason for a missing plume-like structure in the electromagnetic results (Baba et al. in rev.).
The MT results show a broad layer of high conductivity beneath the lithosphere at 120 km depth. This indicates that the rising plume material spreads out in all directions over a broad area when it reached the lithosphere (Fig. 58).
The lithosphere thickness is determined by Sp receiver functions. Its base is proposed to be at 60-75 km depth (Geissler et al. in rev.). The temperature of the lower part of the lithosphere is close to its melting point and therefore fragile at its bottom. The plume material could be impinged the lower part of the lithosphere and is carried eastwards away from the plume due to plate motion. This process may be facilitated along zones of weakness, such as the TdCFZ. Some of these dragged portions are able to reach the surface. Newly discovered bathymetric features close to the archipelago support this : Geissler et al. (in prep.) discovered a new submarine seamount Isolde south of TdC at the flanks of Nightingale Island and mapped small volcanic cones west of the archipelago.
Weit et al. (2016) published constraints on the depth and the degree of melting of TdC basanites and proposed a consistent top depth of about 60 km and a base depth of of 80-100 km for the melting column. These depths coincide roughly with the assumed melt layer below the lithosphere. Stagnation and crystallization of magma is estimated to be in about 30 km depth beneath TdC (Weit et al., 2016) (Fig. 58).
We assume that similar processes form further seamounts and volcanic cones in the whole study area. While most of the bathymetric features are located close to fracture zones, the existing zones of weakness guided the spread material from a layer beneath the bottom of the lithosphere towards the surface (Fig. 58).
Because of the close vicinity of the MAR to the Tristan plume an interaction of both is proposed (Humphris et al., 1985; Schilling et al., 1985; Gibson et al., 2005, Schlömer et al.). In this case the plume material is flowing at the bottom of the thinning lithosphere to the ridge (Fig. 58). This model is already proposed for close ridge-plume configurations (e.g. Humphreys and Niu, 2009; Schilling, 1991). But, the striking difference between these and the Tristan plume is the apparent volcanism at the surface above the plume or above the melt flow. While seamounts and islands indicate generally underlying hot sources no (or only tiny) volcanic features can be observed above the Tristan plume. Therefore, we suggest that plume material flows to the ridge, which prevent a strong vertically penetration of the lithosphere. Schlömer et al. in rev. observed a region of no seismicity west of TdC, which spatially coincides with the location of the

Tristan plume and indicates a ductile region in the lithosphere. This leads to the assumption that there should be recent volcanism. Either, the volcanism has not been detected or it fails to appear and the strength of Tristan plume continues to decline. Perhaps a incipient suppression is in progress as it is proposed by O'Connor et al. (2012).

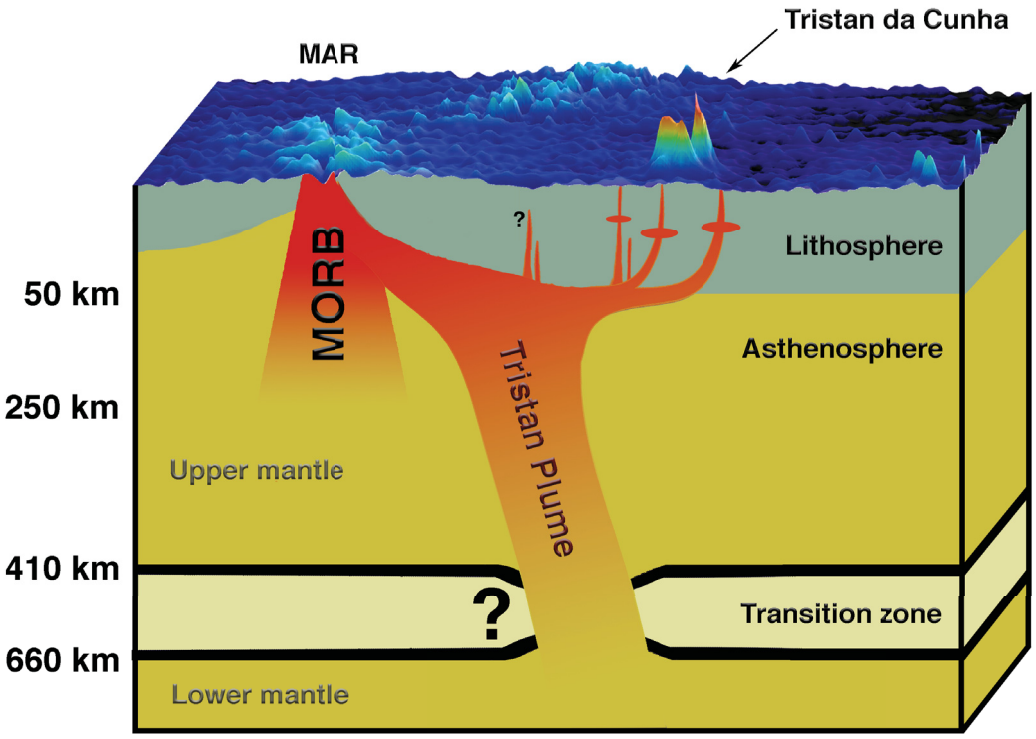

Figure 58: Schematic model of the upper mantle structure beneath TdC. The Tristan plume is shown southwest of the island. Plume material spreads out at the bottom of the lithosphere towards the MAR and towards the east. Beneath TdC plume material reaches the surface.

8.5 Conclusion

By merging electromagnetic and seismological data we were able to reveal the upper mantle structure beneath the Tristan da Cunha hotpot. A high conductivity layer coincides with the upper part of the Tristan plume. We propose on the one hand transport of plume material away from the plume along weak zones in east direction (towards Tristan) and one the other hand flow towards the Mid-Atlantic Ridge. Existing zones of weakness guided the material from a layer beneath the bottom of the lithosphere towards the surface. We assume a weak plume due to missing bathymetric features directly above the plume.

9 Conclusions

This study provides detailed new insights into the upper mantle structure beneath the island of Tristan da Cunha. Here, I summarized the major results of the thesis. All research questions listed in chapter 1.4 will be answered.

Upper mantle: A seismological dataset, consisting of OBS and land stations was used to calculate a finite-frequency tomography, which based on relative travel time residuals, obtained by teleseismic earthquakes.
The results show a low-velocity structure southwest of Tristan da Cunha, which is consistent throughout all depth slices of the model space. I assign this structure to the Tristan conduit and relate it to the origin of Tristan da Cunha. The shape is cylindrical with a diameter of ∼200 km down to a depth of 250 km. In depth greater than 250 km, the structure ramifies into narrow veins, each with a diameter of ∼100 km.
While the distance between the Tristan conduit and the island increases due to plate motion, former feeder channels have been preserved and are still used by plume material to reach the surface close to the archipelago. The presence of partial melt in a broad layer within the study area indicates that raising plume material spreads out laterally along the bottom of the lithosphere. It impinges the base of the lithosphere and is transported away from the plume. This process is facilitated at weak zones such as the Tristan da Cunha fracture zone.
Because of the close proximity to the Mid-Atlantic Ridge, it is likely that plume material flows also along the bottom of the thinning lithosphere towards the ridge. Almost no volcanic activity has been observed directly above the plume, which indicates a weak plume. The potential existence of a second narrow conduit located northeast of TdC points to a complex and heterogeneous mantle. It may be possible that the upper mantle at the southwest end of the Walvis Ridge - Tristan/Gough hotspot track is penetrated by multiple narrow conduits.

Local Seismicity: The seismological dataset was also used to detect local earthquakes. I localised approximately 470 earthquakes in the Tristan region. High seismicity is observed in an African Plate segment north of Tristan da Cunha. The earthquakes reflect the prevailing stress field within the plate, which is caused by different acting forces at the northern boundary of this plate. Several earthquakes were localised close the archipelago of Tristan da Cunha, which can be related to ongoing magmatic activity, such as the forming of new seamounts.
An area without seismic activity coincides spatially with the location of the proposed Tristan conduit. The aseismic/seismic zone may indicate the transition zone between ductile and brittle regime. This is a further indication for a heat source at this location.
Weakening of the lithosphere due to tensions as well as reheating and thinning of the lithosphere by the mantle plume presence are indicators for an incipient ridge jump towards the location of the plume.

In summary, the existence of a Tristan mantle plume has been proven and possible interactions between the upper mantle and the surface have been discussed. Two different independent seismological methodologies give evidences for the location of the Tristan plume southwest of the island.

10 Outlook

This study provides the first geophysical results of the Tristan da Cunha region. Therefore many further questions arise. I will mention some of these and how they could be addressed in the future.

Since the Walvis-Ridge Tristan/Gough hotspot track seems to have bifurcated into a northern subtrack directed towards TdC and a southern subtrack directed towards Gough, it has to be proven, if an additional Gough plume exits or if the island can also be related to the Tristan conduit. To prove this assumptions I would suggest an OBS network designed similar to the network used in this study but with Gough in its centre.
Furthermore, the tomographic results show a second narrow conduit located northeast of TdC, which suggests that the southwest end of the hotspot track is penetrated by multiple conduits. A suitable network should be cover the youngest end of the hotspot track, including both subtracks, the archipelago of Tristan da Cunha and Gough Island. Here, it is important to deploy also OBS stations west of the Mid-Atlantic Ridge to estimate the influence of the Mid-Atlantic Ridge on the travel times.
The tomographic results of this study are limited downwards to a depth of 500 km. While Tristan da Cunha is located above the edge of the LLSVP it has to be proven if this is the origin of the Tristan plume.

New petrological investigations of rock samples of the Mid-Atlantic Ridge segment west of TdC could clarify if and how the plume interacts with the ridge. High resolution bathymetry data as well as sediment echosounder data of the whole Tristan area, including the proposed location of the plume, would show if other volcanic cones or seamounts recently erupted.

It has been shown that the noise in the OBS seismograms is linked to the wind speed. Maximum amplitudes of wind speeds can be directly correlated to the noise maximums or with a small phase shift. It would be interesting to observe this linkages on a smaller scale and to investigate in which way the noise at the surface is linked to the ocean bottom. In the same context it could be investigated if array methods can be applied to determine the direction of propagation and strength of a passing storm.

Whales send acoustic signals, which can be treated in a similar way like seismic waves. This could be used to localised the whales, count their occurrence or differentiate between species. An interesting topic would be the seasonal occurrence of whales in the South Atlantic Ocean.

11 Supplementary

Station	Longitude	Latitude	Elevation [km]
tdc01	-9.6875	-35.9246	-3.9420
tdc02	-9.9938	-36.6687	-3.6360
tdc03	-10.3090	-37.5922	-3.3580
tdc04	-10.7821	-38.3635	-3.5340
tdc05	-11.9621	-38.5811	-3.1640
tdc06	-11.3744	-37.7472	-3.5620
tdc07	-11.2062	-36.9082	-3.7910
tdc08	-10.8025	-36.1323	-3.9510
tdc09	-11.4946	-35.6429	-4.1690
tdc10	-11.9398	-36.2762	-3.7130
tdc11	-12.1223	-36.8780	-3.5700
tdc12	-11.9020	-37.3607	-3.6740
tdc14	-12.4518	-37.9298	-3.3080
tdc15	-13.0818	-38.7528	-3.1840
tdc16	-14.0116	-38.9018	-3.0990
tdc18	-12.9129	-37.5974	-3.1600
tdc19	-13.4182	-37.2571	-3.5800
tdc20	-14.7217	-38.2744	-3.2240
tdc22	-14.5486	-37.4812	-3.3420
tdc23	-14.2836	-36.6469	-3.6720
tdc26	-12.6794	-36.9952	-3.5030
nig01	-12.4755	-37.4177	0.0400
nig02	-12.4777	-37.4183	0.0650
TRIS	-12.3200	-37.0700	0.0600
H09W1	-12.3350	-37.0972	0.0000
H09N1	-12.3152	-37.0681	0.0000

Table S1: Locations and elevations of OBS and land stations

Station	Recorder SN	Start Recording GPS time	Stop Recording GPS time	data recorded kb	Synchronized GPS time	synchtime sec	skew time GPS time	skew time sec	skew µs	comments
TDC01	060738	22.01.2012 20:06:20	02.01.2013 06:21:29	11050725	22.01.2012 20:03:35	375480220	02.01.2013 06:22:08	405325327	1199093	skew from log file
TDC02	060743	22.01.2012 20:54:44	30.11.2012 17:56:44	9026167	22.01.2012 20:53:28	375483213	-	-	-	recorder idle, no END mark
TDC03	060742	22.01.2012 21:26:27	02.01.2013 22:30:50	11302005	22.01.2012 21:25:26	375485131	02.01.2013 22:31:14	405383474	1348781	
TDC04	091107	23.01.2012 09:32:13	03.01.2013 10:15:19	21012032	23.01.2012 09:31:12	375528677	03.01.2013 10:15:45	405425745	1640156	Problems with mcscopy
TDC05	060720	23.01.2012 13:39:54	06.01.2013 16:00:56	11134354	23.01.2012 13:38:26	375543511	06.01.2013 16:01:57	405705717	2429281	
TDC06	060725	23.01.2012 20:31:59	03.01.2013 20:05:17	11253231	23.01.2012 20:30:01	375568206	03.01.2013 20:05:47	405461147	1773843	
TDC07	060729	23.01.2012 22:09:46	04.01.2013 06:05:35	10767531	23.01.2012 22:08:25	375574110	04.01.2013 06:06:05	405497165	2122250	
TDC08	060740	24.01.2012 14:06:11	04.01.2013 17:43:24	7812446	24.01.2012 14:04:28	375631473	04.01.2013 17:43:40	405539020	-847969	
TDC09	060735	24.01.2012 17:28:27	05.01.2013 01:50:00	9971781	24.01.2012 17:26:41	375643606	05.01.2013 01:50:59	405568259	1442281	
TDC10	050921	24.01.2012 20:49:31	05.01.2013 10:59:32	10230696	24.01.2012 20:48:12	375655694	05.01.2013 11:00:29	405601229	1793000	
TDC11	091104	24.01.2012 13:21:17	05.01.2013 18:48:43	19419436	24.01.2012 13:19:57	375628802	05.01.2013 18:50:06	405629406	765593	End sequence 0 03.01.2013 17:53:14
TDC12	060739	25.01.2012 17:21:18	06.01.2013 00:50:46	10766137	25.01.2012 17:20:26	375729628	06.01.2013 00:52:07	405651127	1501937	
TDC14	050907	25.01.2012 21:23:59	06.01.2013 21:22:24	11375747	25.01.2012 21:22:53	375744177	06.01.2013 21:23:20	405725000	1836625	
TDC15	060715	25.01.2012 22:15:07	13.01.2013 02:20:43	11756244	25.01.2012 22:13:59	375747239	13.01.2013 02:21:37	406261297	2932406	
TDC16	060728	26.01.2012 14:11:20	12.01.2013 15:34:16	10478244	26.01.2012 14:10:11	375804616	12.01.2013 15:35:14	406222514	1664625	
TDC17	060713	26.01.2012 14:29:51	-	-	26.01.2012 14:28:57	-	-	-	-	not recovered
TDC18	050930	26.01.2012 21:40:31	28.11.2012 22:14:06	7675321	26.01.2012 21:36:36	375831396	-	-	-	recorder stopped, battery low
TDC19	060708	26.01.2012 20:30:59	*07.01.2013 16:48:28*	9307246	26.01.2012 20:29:49	375827391	08.01.2013 ca. 03:00	405831515	2131752101	15.10.2012 10:10:47 ADC stuck
TDC20	050906	27.01.2012 10:52:05	12.01.2013 07:31:45	10468669	27.01.2012 10:50:56	375879058	12.01.2013 07:32:06	406193526	1738750	
TDC21	060704	27.01.2012 10:22:28	27.01.2012 15:12:49	4093	27.01.2012 10:20:25	-	-	-	-	stopped before deployment
TDC22	060723	27.01.2012 14:47:59	11.01.2013 04:44:17	11394756	27.01.2012 14:47:03	375893227	11.01.2013 04:45:20	406097120	1128406	
TDC23	060724	27.01.2012 15:39:44	10.01.2013 22:35:40	11488175	27.01.2012 15:38:21	375896306	10.01.2013 ca. 22:36	406074999	1643406	2 recording sequences!
TDC25	060703	28.01.2012 19:15:12	-	-	28.01.2012 19:14:30	-	-	-	-	not recovered
TDC26	050902	28.01.2012 13:51:25	09.01.2013 04:57:57	9693667	28.01.2012 13:49:57	375976201	09.01.2013 04:58:27	405925107	1748906	

Figure S1: Skewlist from cruise report

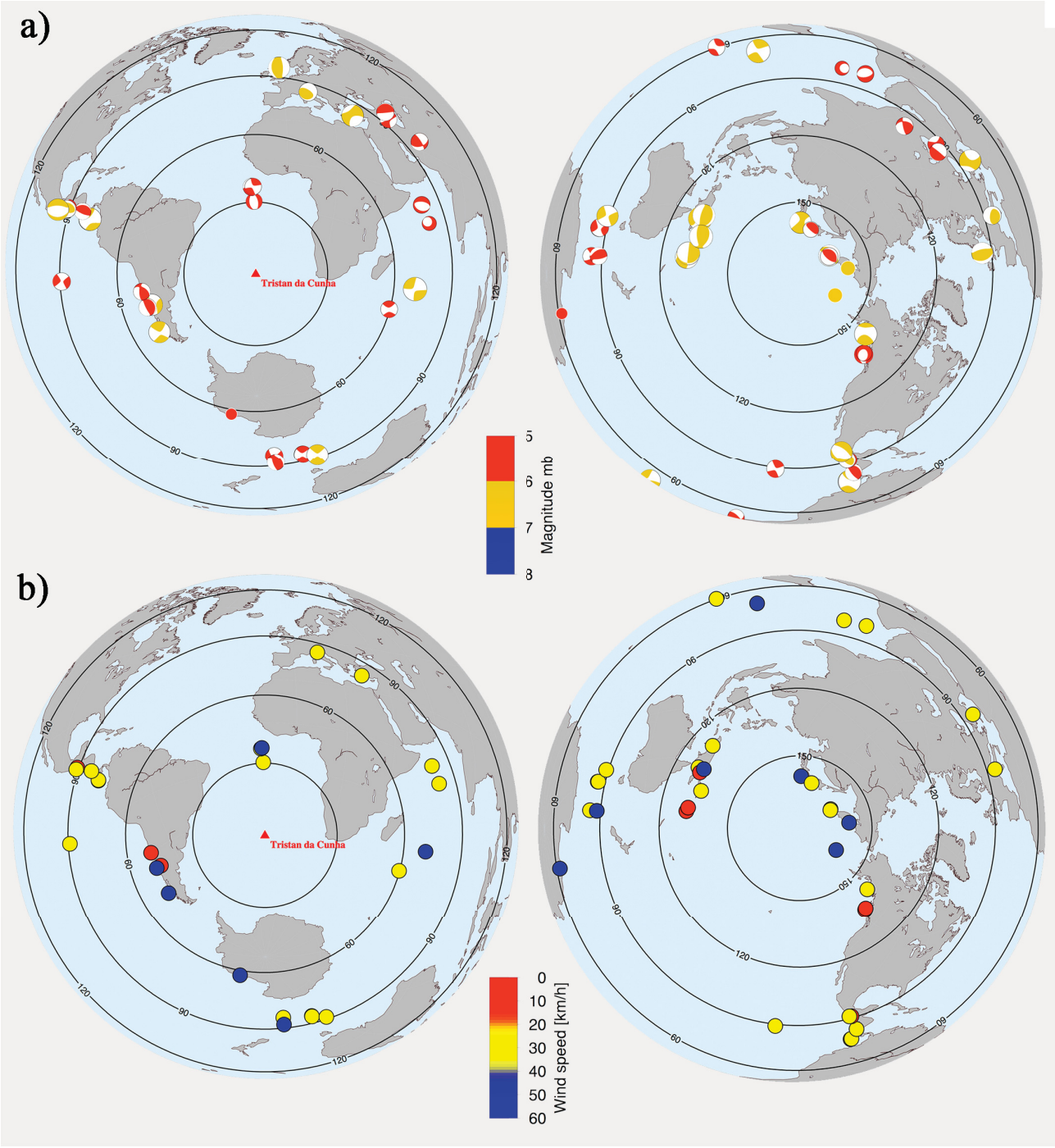

Figure S2: a) Fault mechanism of the earthquakes where only the surface waves are observable. b) Wind speed on TdC at the event time of the earthquakes, which locations are shown.

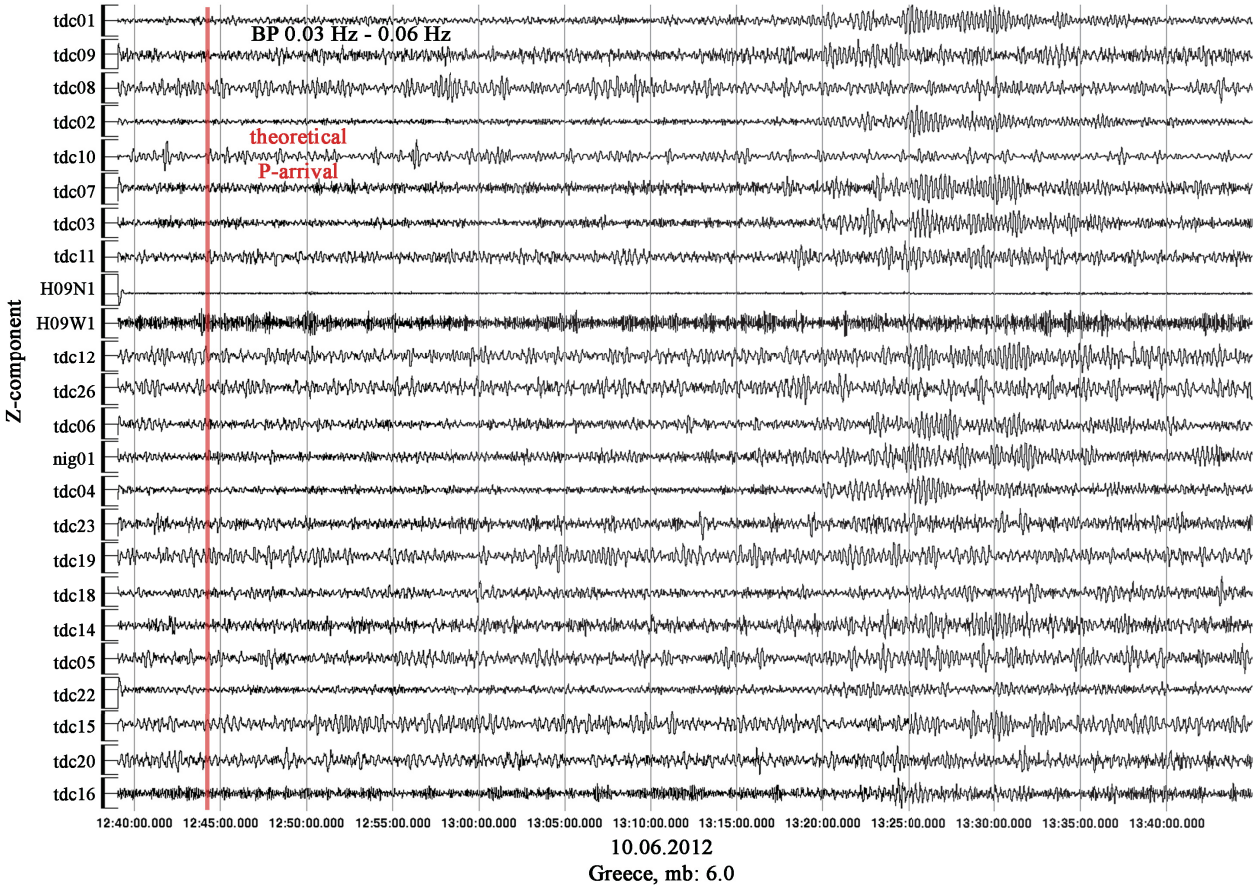

Figure S3: Seismograms of a Greece earthquake (10.06.2012) with magnitude 6.0 (lat: 36.42, lon: 28.80). The theoretical P-arrivals are aligned to the event time (12:44:16). The traces are filtered with a bandpass filter from 0.03 Hz to 0.06 Hz. Only the surface waves can be observed.

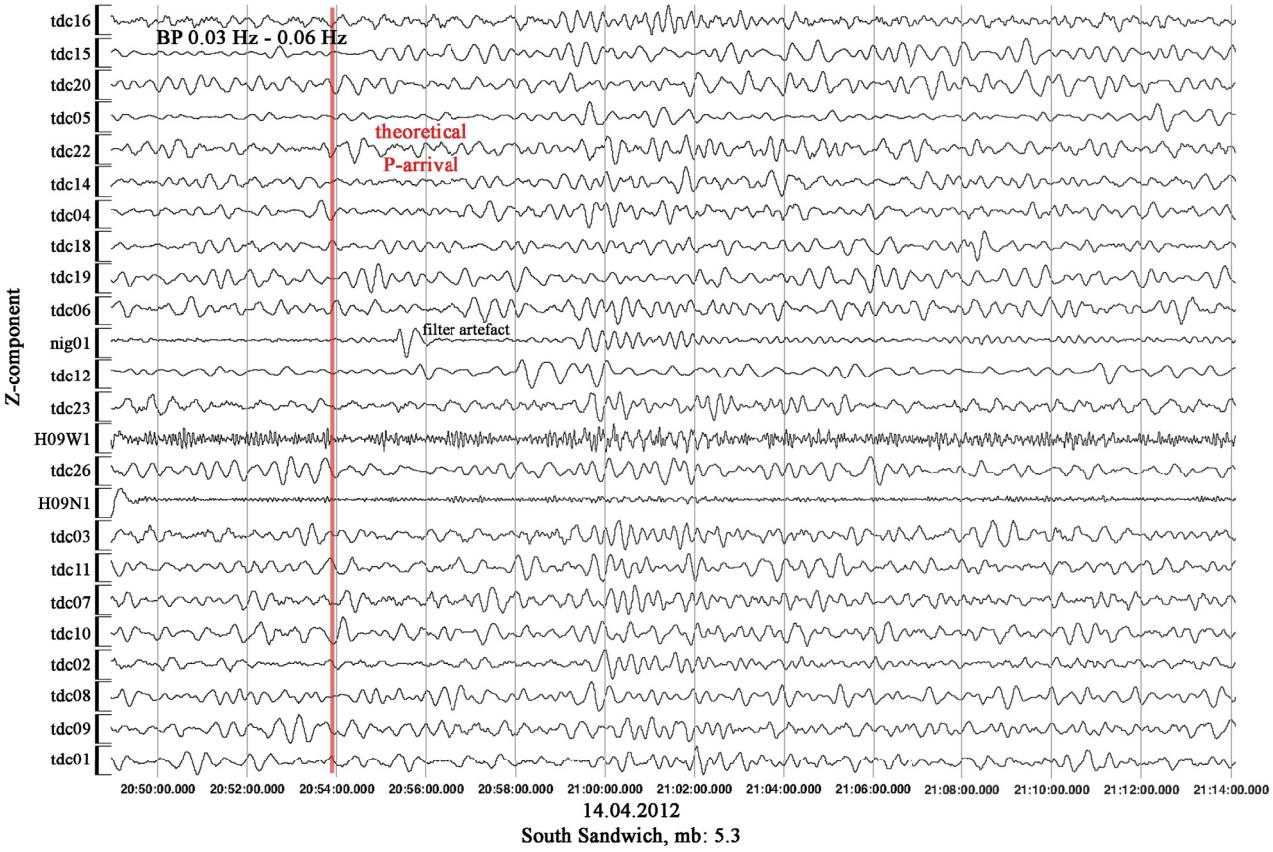

Figure S4: Seismograms of a South Sandwich earthquake (14.04.2012) with magnitude 5.3 (lat: -56.845, lon: -25.209). The theoretical P-arrival is aligned to the event time (14.04.2012). The traces are filtered with a bandpass filter from 0.03 Hz to 0.06 Hz.

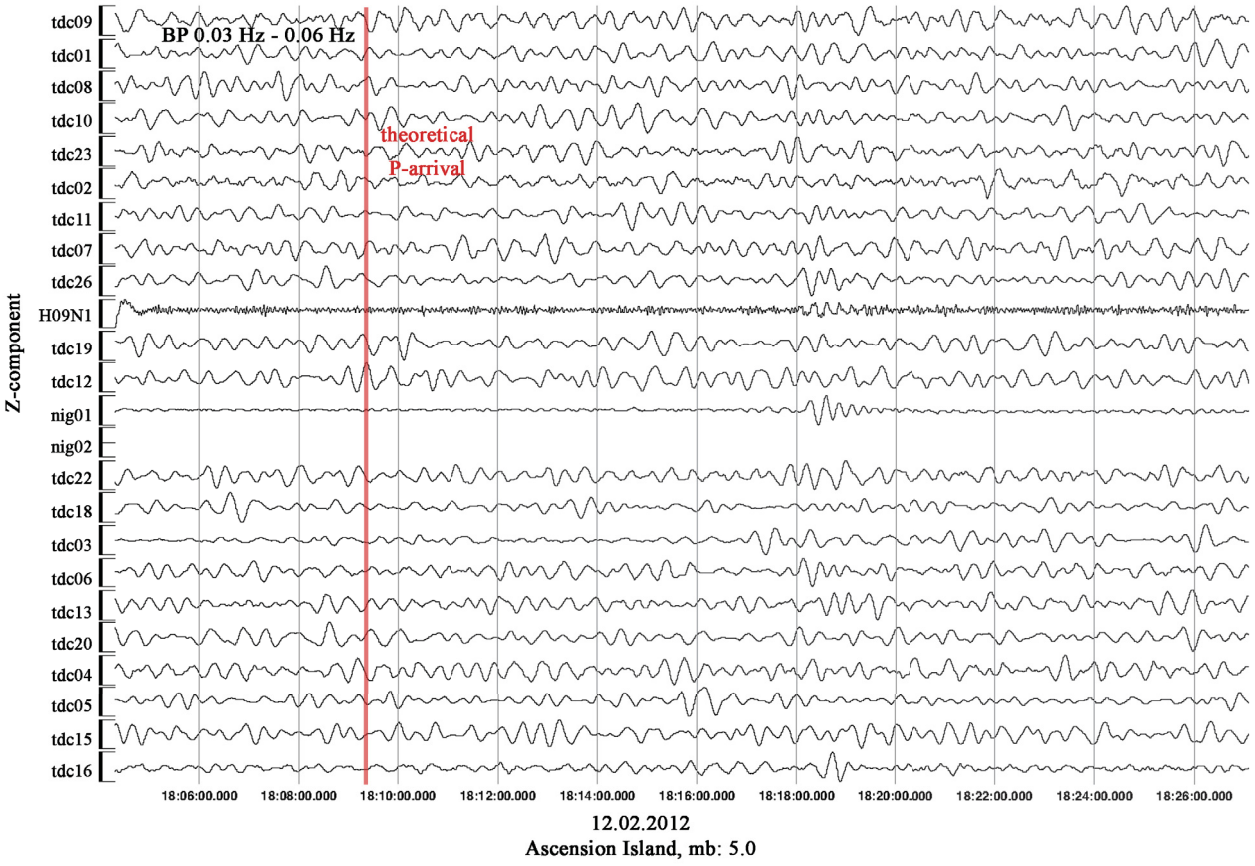

Figure S5: Seismograms of an Ascension Island earthquake (12.02.2012) with magnitude 5.0 (lat: -56.845, lon: -25.209). The theoretical P-arrival is aligned to the event time (14.04.2012). The traces are filtered with a bandpass filter from 0.03 Hz to 0.06 Hz.

References

Anderson, D. L. (2005). Scoring hotspots: The plume and plate paradigms. *Geological Society of America Special Papers*, 388:31–54.

Anderson, D. L. and Schramm, K. A. (2005). Global hotspot maps. *Special Papers-Geological Society Of America*, 388:19.

Argus, D. F., Gordon, R. G., and DeMets, C. (2011). Geologically current motion of 56 plates relative to the no-net-rotation reference frame. *Geochemistry, Geophysics, Geosystems*, 12(11).

Baker, P. E., Gass, I., Harris, P., and le Maitre, R. (1962). The volcanological report of the Royal Society Expedition to Tristan da Cunha. *Philosophical Transactions of the Royal Society of London*, 256.

Bezada, M. J., Levander, A., and Schmandt, B. (2010). Subduction in the southern Caribbean: Images from finite-frequency P wave tomography. *Journal of Geophysical Research: Solid Earth*, 115(B12).

Bormann, P. and Wielandt, E. (2002). Seismic signals and noise. *New manual of seismological observatory practice*, 1.

Briais, A. and Rabinowicz, M. (2002). Temporal variations of the segmentation of slow to intermediate spreading mid-ocean ridges 1. Synoptic observations based on satellite altimetry data. *Journal of Geophysical Research: Solid Earth*, 107(B5).

Bungum, H. and Husebye, E. (1971). Errors in time delay measurements. *pure and applied geophysics*, 91(1):56–70.

Burke, K., , Steinberger, B., Torsvik, T. H., and Smethurst, M. A. (2008). Plume Generation Zones at the margins of Large Low Shear Velocity Provinces on the core–mantle boundary. *Earth and Planetary Science Letters*, 265(1):49–60.

Condie, K. C. (2001). *Mantle plumes and their record in Earth history*. Cambridge University Press.

Courtillot, V., Davaille, A., Besse, J., and Stock, J. (2003). "Three distinct types of hotspots in the Earth's mantle". *Earth and Planetary Science Letters*, 205(3):295–308.

Dahlen, F., Hung, S.-H., and Nolet, G. (2000). Fréchet kernels for finite-frequency traveltimes I. Theory. *Geophysical Journal International*, 141(1):157–174.

Duncan, R. A. and Richards, M. (1991). Hotspots, mantle plumes, flood basalts, and true polar wander. *Reviews of Geophysics*, 29(1):31–50.

Eberhart-Phillips, D. (1986). Three-dimensional velocity structure in northern California Coast Ranges from inversion of local earthquake arrival times. *Bulletin of the Seismological Society of America*, 76(4):1025–1052.

Fairhead, J. D. and Wilson, M. (2005). Plate tectonic processes in the South Atlantic Ocean: Do we need deep mantle plumes? *Geological Society of America Special Papers*, 388:537–553.

Faul, U. H. and Jackson, I. (2005). The seismological signature of temperature and grain size variations in the upper mantle. *Earth and Planetary Science Letters*, 234(1):119–134.

Foulger, G. and Natland, J. H. (2003). Is "hotspot" volcanism a consequence of plate tectonics? *Science*, 300(5621):921–922.

French, S. W. and Romanowicz, B. (2015). Broad plumes rooted at the base of the Earth's mantle beneath major hotspots. *Nature*, 525(7567):95–99.

Fromm, T., Planert, L., Jokat, W., Ryberg, T., Behrmann, J., Weber, M., and Haberland, C. (2015). South Atlantic opening: A plume-induced breakup? *Geology*, 43(10):931–934.

Gaherty, J. B., Kato, M., and Jordan, T. H. (1999). Seismological structure of the upper mantle: a regional comparison of seismic layering. *Physics of the Earth and Planetary Interiors*, 110(1):21–41.

Gassmöller, R., Dannberg, J., Bredow, E., Steinberger, B., and Torsvik, T. H. (2016). Major influence of plume-ridge interaction, lithosphere thickness variations, and global mantle flow on hotspot volcanism—The example of Tristan. *Geochemistry, Geophysics, Geosystems*, 17(4):1454–1479.

Gibson, S., Thompson, R., Day, J., Humphris, S., and Dickin, A. (2005). Melt-generation processes associated with the Tristan mantle plume: Constraints on the origin of EM-1. *Earth and Planetary Science Letters*, 237(3):744–767.

Granet, M., Wilson, M., and Achauer, U. (1995). Imaging a mantle plume beneath the French Massif Central. *Earth and Planetary Science Letters*, 136(3):281–296.

Hanan, B., Kingsley, R., and Schilling, J.-G. (1986). Pb isotope evidence in the South Atlantic for migrating ridge-hotspot interactions. *Nature*, 322:137–144.

Hards, V. (2004). Assessment of volcanic activity in the wake of the seismic episode of 29/30 July 2004 on Tristan da Cunha, South Atlantic Ocean. *British Geological Survey Commissioned Report CR/04/235*.

Haxel, J. and Dziak, R. (2005). Evidence of explosive seafloor volcanic activity from the Walvis Ridge, South Atlantic Ocean. *Geophysical research letters*, 32(13).

Heit, B., Yuan, X., Weber, M., Geissler, W., Jokat, W., Lushetile, B., and Hoffmann, K.-H. (2015). Crustal thickness and Vp/Vs ratio in NW Namibia from receiver functions: Evidence for magmatic underplating due to mantle plume-crust interaction. *Geophysical Research Letters*.

Hicks, A., Barclay, J., Mark, D. F., and Loughlin, S. (2012). Tristan da Cunha: Constraining eruptive behavior using the 40Ar/39Ar dating technique. *Geology*, 40(8):723–726.

Hoernle, K., Rohde, J., Hauff, F., Garbe-Schönberg, D., Homrighausen, S., Werner, R., and Morgan, J. P. (2015). How and when plume zonation appeared during the 132 Myr evolution of the Tristan Hotspot. *Nature communications*, 6.

Humphreys, E. R. and Niu, Y. (2009). On the composition of ocean island basalts (OIB): The effects of lithospheric thickness variation and mantle metasomatism. *Lithos*, 112(1):118–136.

Humphris, S. E., Thompson, G., Schilling, J.-G., and Kingsley, R. H. (1985). Petrological and geochemical variations along the Mid-Atlantic Ridge between 46 S and 32 S: influence of the Tristan da Cunha mantle plume. *Geochimica et Cosmochimica Acta*, 49(6):1445–1464.

Hung, S.-H., Dahlen, F., and Nolet, G. (2000). Fréchet kernels for finite-frequency traveltimes II. Examples. *Geophysical Journal International*, 141(1):175–203.

Jokat, W., Boebel, T., König, M., and Meyer, U. (2003). Timing and geometry of early Gondwana breakup. *Journal of Geophysical Research: Solid Earth (1978–2012)*, 108(B9).

Karato, S.-i. (1993). Importance of anelasticity in the interpretation of seismic tomography. *Geophysical Research Letters*, 20(15):1623–1626.

Karato, S.-i. and Jung, H. (1998). Water, partial melting and the origin of the seismic low velocity and high attenuation zone in the upper mantle. *Earth and Planetary Science Letters*, 157(3):193–207.

Kennett, B., Engdahl, E., and Buland, R. (1995). Constraints on seismic velocities in the Earth from traveltimes. *Geophysical Journal International*, 122(1):108–124.

Keßling, S. (2008). Die Tiefenstruktur der Kruste des Discovery Seamounts und des südlichen Walfischrückens im Südatlantik. Master's thesis, University Jena.

Le Roex, A., Cliff, R., and Adair, B. (1990). Tristan da Cunha, South Atlantic: geochemistry and petrogenesis of a basanite-phonolite lava series. *Journal of Petrology*, 31(4):779–812.

Lee, C.-T. A. (2003). Compositional variation of density and seismic velocities in natural peridotites at STP conditions: Implications for seismic imaging of compositional heterogeneities in the upper mantle. *Journal of Geophysical Research: Solid Earth*, 108(B9).

Maercklin, N. (2002). SUPOLAR and SUPOFILT: SU programs for polarization analysis and filtering of three-component data.

Marquering, H., Dahlen, F., and Nolet, G. (1999). Three-dimensional sensitivity kernels for finite-frequency traveltimes: the banana-doughnut paradox. *Geophysical Journal International*, 137(3):805–815.

Masalu, D. C. P. (2015). Global Mid-Ocean Ridges Mantle Tomography Profiles. *Earth Sciences*, 4(2):80–88.

Mittelstaedt, E., Ito, G., and Behn, M. D. (2008). Mid-ocean ridge jumps associated with hotspot magmatism. *Earth and Planetary Science Letters*, 266(3):256–270.

Montelli, R., Nolet, G., Dahlen, F. A., Masters, G., Engdahl, E. R., and Hung, S.-H. (2004). Finite-Frequency Tomography Reveals a Variety of Plumes in the Mantle. *Science*, 303(5656):338–343.

Morgan, W. J. (1971). Convection plumes in the lower mantle. *Nature*, 230.

Morgan, W. J. (1972). Deep mantle convection plumes and plate motions. *Am. Assoc. Pet. Geol. Bull*, 56(2):203–213.

Nataf, H.-C. and VanDecar, J. (1993). Seismological detection of a mantle plume? *Nature*, 364(6433):115–120.

O'Connor, J. and Duncan, R. (1990). Evolution of the Walvis Ridge-Rio Grande Rise hot spot system: Implications for African and South American plate motions over plumes. *Journal of Geophysical Research*, 95(B11):17475–17502.

O'Connor, J., Jokat, W., le Roex, A., Class, C., Wijbrans, J., Keßling, S., Kuiper, K., and Nebel, O. (2012). Hotspot trails in the South Atlantic controlled by plume and plate tectonic processes. *Nature Geoscience*, 5(10):735–738.

O'Connor, J. M. and Jokat, W. (2015). Age distribution of Ocean Drill sites across the Central Walvis Ridge indicates plate boundary control of plume volcanism in the South Atlantic. *Earth and Planetary Science Letters*, 424:179–190.

O'Connor, J. M. and le Roex, A. P. (1992). South Atlantic hot spot-plume systems: 1. Distribution of volcanism in time and space. *Earth and Planetary Science Letters*, 113(3):343–364.

O'Mongain, A., Ottemoller, L., Baptie, B., Galloway, D., and Booth, D. (2007). Seismic activity associated with a probable submarine eruption near Tristan da Cunha, July 2004–July 2006. *Seismological Research Letters*, 78(3):375–382.

Paige, C. C. and Saunders, M. A. (1982). LSQR: An algorithm for sparse linear equations and sparse least squares. *ACM Transactions on Mathematical Software (TOMS)*, 8(1):43–71.

Phipps Morgan, J., Morgan, W. J., and Price, E. (1995). Hotspot melting generates both hotspot volcanism and a hotspot swell? *Journal of Geophysical Research: Solid Earth*, 100(B5):8045–8062.

Reagan, M. K., Turner, S., Legg, M., Sims, K. W., and Hards, V. L. (2008). 238 U-and 232 Th-decay series constraints on the timescales of crystal fractionation to produce the phonolite erupted in 2004 near Tristan da Cunha, South Atlantic Ocean. *Geochimica et cosmochimica acta*, 72(17):4367–4378.

Renne, P. R., Glen, J. M., Milner, S. C., and Duncan, A. R. (1996). Age of Etendeka flood volcanism and associated intrusions in southwestern Africa. *Geology*, 24(7):659–662.

Richards, M. A., Duncan, R. A., and Courtillot, V. E. (1989). Flood basalts and hot-spot tracks: plume heads and tails. *Science*, 246(4926):103–107.

Ritsema, J. and Allen, R. M. (2003). The elusive mantle plume. *Earth and Planetary Science Letters*, 207(1):1–12.

Ritsema, J., Deuss, A., Van Heijst, H., and Woodhouse, J. (2011). S40RTS: a degree-40 shear-velocity model for the mantle from new Rayleigh wave dispersion, teleseismic traveltime and normal-mode splitting function measurements. *Geophysical Journal International*, 184(3):1223–1236.

Ritsema, J., van Heijst, H. J., and Woodhouse, J. H. (1999). Complex shear wave velocity structure imaged beneath Africa and Iceland. *Science*, 286(5446):1925–1928.

Ritter, J. R., Jordan, M., Christensen, U. R., and Achauer, U. (2001). A mantle plume below the Eifel volcanic fields, Germany. *Earth and Planetary Science Letters*, 186(1):7–14.

Rohde, J., Hoernle, K., Hauff, F., Werner, R., O'Connor, J., Class, C., Garbe-Schönberg, D., and Jokat, W. (2013a). 70 Ma chemical zonation of the Tristan-Gough hotspot track. *Geology*, 41(3):335–338.

Rohde, J. K., van den Bogaard, P., Hoernle, K., Hauff, F., and Werner, R. (2013b). Evidence for an age progression along the Tristan-Gough volcanic track from new $^{40}Ar/^{39}Ar$ ages on phenocryst phases. *Tectonophysics*, 604:60–71.

Sandwell, D. T., Müller, R. D., Smith, W. H., Garcia, E., and Francis, R. (2014). New global marine gravity model from CryoSat-2 and Jason-1 reveals buried tectonic structure. *Science*, 346(6205):65–67.

Scherbaum, F. (2013). *Of poles and zeros: Fundamentals of digital seismology*, volume 15. Springer Science & Business Media.

Schilling, J., Thompson, G., Kingsley, R., and Humphris, S. (1985). Hotspot-migrating ridge interaction in the South Atlantic. *Nature*, 313:187–191.

Schilling, J.-G. (1991). Fluxes and excess temperatures of mantle plumes inferred from their interaction with migrating mid-ocean ridges. *Nature*, 352:397–403.

Schmandt, B. and Humphreys, E. (2010). Seismic heterogeneity and small-scale convection in the southern California upper mantle. *Geochemistry, Geophysics, Geosystems*, 11(5).

Silveira, G., Stutzmann, E., Davaille, A., Montagner, J.-P., Mendes-Victor, L., and Sebai, A. (2006). Azores hotspot signature in the upper mantle. *Journal of Volcanology and Geothermal Research*, 156(1):23–34.

Sleep, N. H. (1990). Hotspots and mantle plumes: Some phenomenology. *Journal of Geophysical Research: Solid Earth (1978–2012)*, 95(B5):6715–6736.

Sleep, N. H. (2002). Ridge-crossing mantle plumes and gaps in tracks. *Geochemistry Geophysics Geosystems*, 3(12):8505.

Smith, D. K., Escartin, J., Cannat, M., Tolstoy, M., Fox, C. G., Bohnenstiehl, D. R., and Bazin, S. (2003). Spatial and temporal distribution of seismicity along the northern Mid-Atlantic Ridge (15 °–35 ° N). *Journal of Geophysical Research: Solid Earth*, 108(B3).

Spetzler, H. and Anderson, D. L. (1968). The effect of temperature and partial melting on velocity and attenuation in a simple binary system. *Journal of Geophysical Research*, 73(18):6051–6060.

Torsvik, T. H., Smethurst, M. A., Burke, K., and Steinberger, B. (2006). Large igneous provinces generated from the margins of the large low-velocity provinces in the deep mantle. *Geophysical Journal International*, 167(3):1447–1460.

VanDecar, J. and Crosson, R. (1990). Determination of teleseismic relative phase arrival times using multi-channel cross-correlation and least squares. *Bulletin of the Seismological Society of America*, 80(1):150–169.

Villagómez, D. R., Toomey, D. R., Hooft, E. E. E., and Solomon, S. C. (2007). Upper mantle structure beneath the Galápagos Archipelago from surface wave tomography. *Journal of Geophysical Research: Solid Earth*, 112(B7).

White, R. and McKenzie, D. (1989). Magmatism at rift zones: The generation of volcanic continental margins and flood basalts. *Journal of Geophysical Research: Solid Earth*, 94(B6):7685–7729.

Wilson, J. T. (1963). A possible origin of the Hawaiian Islands. *Canadian Journal of Physics*, 41(6):863–870.

Wilson, M. and Guiraud, R. (1992). Magmatism and rifting in Western and Central Africa, from Late Jurassic to Recent times. *Tectonophysics*, 213(1):203–225.

Wolfe, C. J., Bjarnason, I. T., VanDecar, J. C., and Solomon, S. C. (1997). Seismic structure of the Iceland mantle plume. *Nature*, 385(6613):245–247.

Wolfe, C. J., McNutt, M. K., and Detrick, R. S. (1994). The Marquesas archipelagic apron: Seismic stratigraphy and implications for volcano growth, mass wasting, and crustal underplating. *Journal of Geophysical Research: Solid Earth (1978–2012)*, 99(B7):13591–13608.

Youssof, M., Thybo, H., Artemieva, I., and Levander, A. (2015). Upper mantle structure beneath southern African cratons from seismic finite-frequency P- and S-body wave tomography. *Earth and Planetary Science Letters*, 420:174 – 186.

Zhang, Y.-S. and Tanimoto, T. (1993). High-resolution global upper mantle structure and plate tectonics. *Journal of Geophysical Research: Solid Earth (1978–2012)*, 98(B6):9793–9823.

12 Danksagung

Ein herzliches Dankeschön geht an

- Wolfram Geissler für die Betreuung meiner Arbeit, die vielen Diskussionen und die Geduld meine Manuskripte zu lesen.
- Wilfried Jokat für den freitags nachmittag Schnack. Ich werde immer das Bild im Kopf haben, wie er in unserem Türrahmen steht, die Hände hochwirft und sein legendäres "Und?" in den Raum wirft.
- die Geophysiker-Truppe, auf deren Flur meist immer was los ist.
- den Hexenzirkel für die anregenden Themen bei der Mittagsrunde.
- die Kaffeetanten, die nachmittags für eine abwechslungsreiche Pause sorgen und den NP-Schoko-Vorrat immer auf einem konstanten Level halten.
- mein Bürogegenüber, wo mittlerweile nur eine hochgezogene Augenbraue über den Rand des Bildschirmes hinweg mehr als tausend Worte sagt. Auch wenn sie mir ständig irgendwo kitschige Dinge versteckt.
- meine Familie im Sauerland - Schön, dass es Euch gibt.

Desweiteren möchte ich Wilfried Jokat und Wolfgang Bach für die Begutachtung dieser Arbeit danken.